6-2022

Probing the Processes of Planet Formation via Studies of the ϵ Chameleonitis Association

D. Annie Dickson-Vandervelde
dad1197@rit.edu

Recommended Citation

Dickson-Vandervelde, D. Annie, "Probing the Processes of Planet Formation via Studies of the ϵ Chameleonitis Association" (2022). Thesis. Rochester Institute of Technology. Accessed from

Probing the Processes of Planet Formation via Studies of the ϵ Chameleonitis Association

---

Ph.D. *Doctor of Philosophy*

in Astrophysical Sciences and Technology

D. Annie Dickson-Vandervelde

School of Physics and Astronomy

Rochester Institute of Technology

Rochester, New York

June 2022

ASTROPHYSICAL SCIENCES AND TECHNOLOGY
COLLEGE OF SCIENCE
ROCHESTER INSTITUTE OF TECHNOLOGY
ROCHESTER, NEW YORK

Ph.D. DISSERTATION DEFENSE

Candidate: . . . .

Dissertation Title: . . . .

Adviser: . . . .

Date of defense: . . . .

The candidate's Ph.D. Dissertation has been reviewed by the undersigned. The Dissertation

(a) is acceptable, as presented.
(b) is acceptable, subject to minor amendments.
(c) is not acceptable in its current form.

Written details of required amendments or improvements have been provided to the candidate.

Committee:

____
Dr. Gabriel Diaz, Committee Chair

____
Dr. Josh Faber, Committee Member

____
Dr. Jacqueline Faherty, Committee Member

____
Dr. Joel Kastner, Thesis Advisor

Please submit form to AST Graduate Program Coordinator

ASTROPHYSICAL SCIENCES AND TECHNOLOGY
COLLEGE OF SCIENCE
ROCHESTER INSTITUTE OF TECHNOLOGY
ROCHESTER, NEW YORK

CERTIFICATE OF APPROVAL

Ph.D. DEGREE DISSERTATION

The Ph.D. Degree Dissertation of *D. Annie Dickson-Vandervelde* has been examined and approved by the dissertation committee as satisfactory for the dissertation requirement for the Ph.D. degree in Astrophysical Sciences and Technology.

Dr. Gabriel Diaz, Committee Chair

Dr. Josh Faber, Committee Member

Dr. Jacqueline Faherty, Committee Member

Dr. Joel Kastner, Thesis Advisor

Date ______________________________

Probing the Processes of Planet Formation via Studies of the ϵ Chameleonitis Association

By

D. Annie Dickson-Vandervelde

A dissertation submitted in partial fulfillment of the
requirements for the degree of Ph.D. in Astrophysical
Sciences and Technology, in the College of Science,
Rochester Institute of Technology.

June 17, 2022

Approved by

Dr. Andrew Robinson Date
Director, Astrophysical Sciences and Technology

Abstract

Nearby Young Moving Groups (NYMGs), i.e., loose groups of stars of age $\lesssim 100$ Myr in the solar vicinity, present ideal, accessible observational laboratories for studies on star and planet formation. Studying individual members of NYMGs, especially those hosting protoplanetary disks, in the infrared and millimeter regimes gives astronomers key information on disk evolution and the planet formation process. In this dissertation, I present an analysis of newly available data for members of one of the youngest known NYMGs, the ϵ Chameleonitis Association (ϵCA), including detailed studies of two ϵCA members that host protoplanetary disks viewed at high inclinations (i.e. within ~30 degrees of edge-on). Through analysis of Gaia Space Astrometry Mission data for the ϵCA, I present updated constraints on the Galactic positions and kinematics and color-magnitude diagram positions of ϵCA members and candidates. I reassess their membership status and refine estimates of the multiplicity and disk fraction of the group. I determine a mean distance to ϵCA of 101.0 ± 4.6 pc and confirm that, at an age of 5^{+3}_{-2} Myr, it represents the youngest stellar group within ~100 pc of Earth. The two nearly edge-on star-disk systems studied here are representative of the diversity of planet-forming environments around young stars. The first, 2M1155−79B, was discovered during the aforementioned Gaia study of the ϵCA. Near-infrared spectra of 2M1155−79B, along with analysis of photometry from Gaia EDR3, 2MASS, VHS, and WISE, reveal that 2M1155−79B is most likely a young, late-M, star near the hydrogen-burning limit that is partially obscured by, and actively accreting from, a nearly edge-on circumstellar disk. The second planet-forming disk studied here orbits T Cha, a near solar-mass ϵCA member. I present archival Atacama Large Millimeter Array images of the millimeter continuum and ^{12}CO (3-2) and ^{13}CO (3-2) emission from the highly inclined (i~73°) T Cha disk. Radial brightness profiles show a limb-brightened ring of CO gas orbiting inside of the large dust grains generating the millimeter continuum, surrounded by a radially and vertically extended region of CO gas out to radii of ~200 AU that modelling reveals is likely probing the vertical freeze-out. These analyses illustrate the future potential of the ϵCA for providing new insights into star and planet formation processes.

Contents

List of Figures

List of Tables

Chapter 1

Introduction

While human kind has always been interested in worlds beyond, accompanied by a fascination with the alien other, the first exoplanet was not discovered until 1992 orbiting twin pulsars [15]. A few years later in 1995, the next planet would be found around a main sequence star and the amount of known exoplanets would proceed to expand exponentially [16]. The leftover gas and dust from star formation orbiting around young stars would become the key to discovering both the formation mechanisms of the Solar System and exoplanetary systems. Particularly, systems around solar-mass stars can give scientists key insights into the properties of the Solar Nebula.

In pre-Main Sequence (MS) stars, the remnants of stellar formation orbit the young star in a disk made of dust and gas. These disks are presumed, and thus noted, as protoplanetary - their conditions thus being the conditions of planet formation. The properties of planets that form from these disks are directly linked to the physical conditions of the disk thus linking the study of protoplanetary disks to our knowledge of planet attributes. As low-mass stars ($M < 4M_{\odot}$) constitute the vast majority of stars in the Galaxy, they are particularly relevant targets in the expanding knowledge of planet formation. Very low-mass stars ($M < 0.4M_{\odot}$) have emerged as the most promising targets for detections of potentially habitable planets (e.g., [17, 18, 19]) – the terrestrial planet occurrence rate around M dwarfs in their habitable zones ($\sim$0.1–0.4 au) is $\sim$50% [20, 21, 22].

1.1 Star and Disk Formation

All stars begin in giant molecular clouds, regions in the interstellar medium that are over-dense (e.g. the reviews, [23, 24]). Typical densities of these regions vary between 10^2 – 10^4 particles per cm^3 and temperatures between 10 and 100 K. Giant molecular clouds are composed of molecular gas and dust, which will eventually become the direct building blocks for planets. The gas components of these clouds are mainly H_2, He, CO, and N_2. High-mass star formation happens on very fast timescales, see Zinnecker and Yorke (2007) for a great overview of massive star formation [25], but for the purpose of this thesis we will overview the lower-mass star formation process.

Low-mass protostars form due to dense core substructures within over-dense filamentary regions within giant molecular clouds (Fig. 1.1a). Eventually, the dense cores become dense enough to overcome the thermal and magnetic pressure of the cloud and they begin to collapse and form an initial prestellar core [26]. Because of this process, star formation within these massive ($\sim 10^5$-10^6 $M_\odot$) clouds often creates embedded clusters (see review by Lada & Lada (2003) [27]). After this initial collapse, the prestellar core continues to increase in mass due to material infalling from the surrounding cloud matter (the protostellar envelope) while it decreases in radius due to radiative energy loss. The secondary collapse is driven by the dissociation of the hydrogen molecules, after which the protostar is formed (Fig. 1.1b).

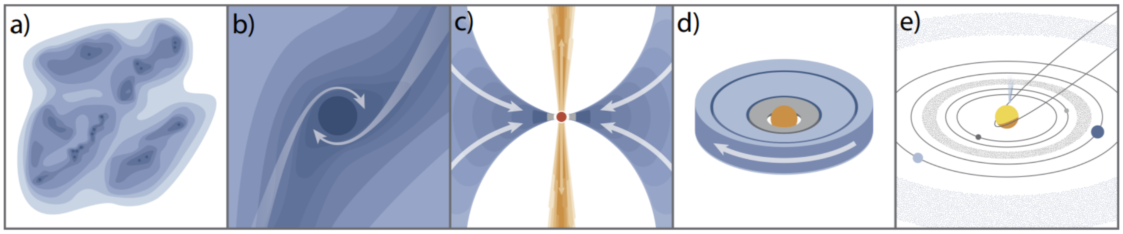

Figure 1.1: Cartoon of the different stages that characterize low-mass (Solar-like) star and planet formation. a) Dense cores form in interstellar molecular clouds. b) The dense core begins to collapse in on itself and form a star. c) The collapsed core becomes a protostar while remaining material from the molecular cloud accretes onto the protostar, funneled by a disk and creating jets. d) The cloud disperses and leaves behind a pre-MS star and a protoplanetary disk. e) The material from the disk that is not accreted onto the star or planets is dispersed via winds, leaving behind a planetary system and a young star. From Oberg & Bergin (2021) [1](credited to K. Peek)

Mass from the surrounding cloud continues to accrete onto the protostar and often results in protostellar outflows and jets, which helps remove angular momentum as well as mass from the system (Fig. 1.1c). This process also leads to this material spreading into a disk surrounding the protostar, which forms through conservation of angular momentum. Protostars are highly magnetized systems, which complicates the process of disk formation (see review of these processes in [28]).

Disks are observed to already be formed while the protostar is still embedded, commonly referred to as a Class 0/I young stellar objects (YSOs). These classes were initially developed based on the spectral slope of the spectral energy distribution (SED) in the 2.2–20 μm wavelengths and correspond to different stages of the the early star and disk formation. Class 0 YSOs are this “first” phase where the protostar is still heavily embedded in its envelope. The system continues to evolve and the protostellar envelope begins to dissipate, which allows emission from the protostar and its disk to be observed in the infrared. The YSO is then classified as a Class I.

The protostellar envelope continues to accrete more mass into the protostar system until the envelope becomes mostly depleted. The remaining mass is then locked into the star and disk, which results in a pre-MS star surrounded by a Keplerian disk (Fig. 1.1d). This is the Class II stage − where the envelope has completely dissipated and the protostar is now visible in the optical. Class II disks are both gas- and dust-rich and commonly referred to as protoplanetary.

1.2 Utilizing Nearby Young Moving Groups

Nearby Young Moving Groups (NYMGs) are loose stellar associations of young (<200 Myr) stars within ∼120 pc that formed together in both time and space. These associations, by nature, share age, chemical composition, distance and kinematics. The co-eval nature of NYMG provides good benchmarks for theoretical isochrones and are key to deepening our understanding of star and planet formation. They present ideal environments for studying nascent exoplanets and low-mass stars/brown dwarfs (e.g., [29, 30]) due to both their proximity,

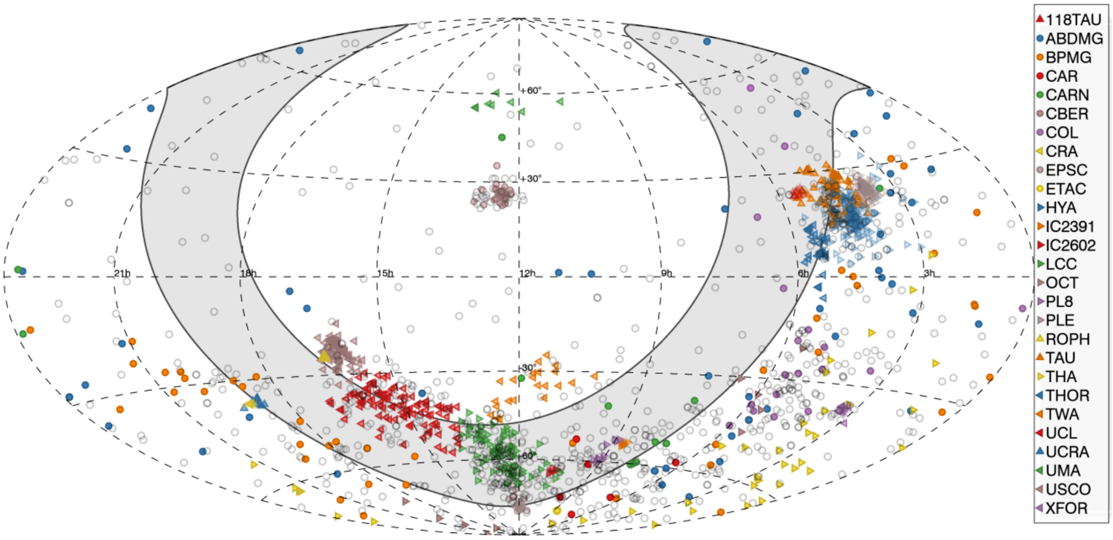

Figure 1.2: Gaia sky positions of known *bona fide* members in young associations as presented in Gagne & Faherty (2018) [2]

youth, and their well-constrained ages. The majority of these associations reside within the age range where protoplanetary disks are quickly evolving, through disk evolution processes, into debris disks and planetary systems. Because of this, constraining the known members of NYMG is paramount in the study of young stars and planet formation.

Age determinations of NYMG are often done through theoretical isochronal fitting to the association. Theoretical isochrones are derived from stellar evolutionary tracks (e.g., [5, 31]) that represent a function of temperature (color) and luminosity (brightness) at a single age, spanning all spectral types. This method produces a range of ages for groups, and is dependant on which models are used, especially in lower-mass stars since prescriptions for handling magnetic activity in stars vary between modelling groups.

There are roughly a couple dozen NYMG, although the exact number and memberships are constantly under evaluation (see reviews [29, 32]). A recent census of NYMG as projected on the sky is illustrated in Fig. 1.2.

1.2.1 Studying NYMG with Gaia

Gaia has been an important tool in bettering the census of known NYMG members because of the importance of precise distance and proper motions when determining galactic coordinates and space velocities. Before the Gaia space astrometry mission [33], constraining the distances and space motions of nearby young stars was reliant on previous parallax missions (like the Hipparcos mission), and individual study of stars that showed other symptoms of youth (i.e. Lithium absorption). Through the release of stellar parallaxes and proper motions for a billion stars [34, 9], the Gaia space mission provides an opportunity to test membership by analyzing individual stars' galactic space motions - although Gaia does not yield radial velocities (RVs) for all stars, which means that many stars still need follow up observations to determine their 3D galactic velocities.

The first three data releases of Gaia (DR1, DR2, and EDR3) have already been used to advance the list of known members of many NYMG using statistical searches through its database (e.g., [2, 35, 36]). It has also been a helpful tool in re-analyzing membership of previously accepted members of NYMG that no longer fall in the correct distance and motion regimes.

1.3 Protoplanetary Disk Evolution

Due to their constrained youth and proximity, the youngest NYMGs provide excellent subjects for studies of planet-forming disks. The evolution from protoplanetary disk (Fig. 1.1d) to stellar-planet system (Fig. 1.1e) takes place over the course of 1-30 Myr (see reviews in [37, 38, 39, 3]). The initial stages of the disk mass loss is powered by both the accretion of gas onto the star and the far-UV (FUV) photoevaporation of the outer disk. Photoevaporation is the process of high energy photons heating up individual atoms and molecules, which increases their velocities to greater than the escape velocity of the disk. During the phase of accretion dominated disk mass depletion, photoevaporation limits the expanse of the disk, limiting the disk to outer radii of a few hundred AU. While the disk is losing mass mainly via accretion, the dust grains within the disk begin growing larger and settling in the mid-plane. This decreases the scale height of the disk's dust component and flattens the flared edges of the disk.

As the disk evolves, and the gas mass decreases, the accretion rate decreases and the rate of photoevaporation increases due to energetic photons from the host star penetrating the optically thinner inner disk more easily. This process limits the refueling of the inner disk from the outer disk material [40]. With the formation of the inner hole, the disk mass begins to dissipate rapidly. The remaining gas within the disk is dispersed by photoevaporation (winds) or accreted onto planets.

1.3.1 Planet Formation

Formation of planets most likely begins while the star-disk system is still in its protostellar envelope phase, although the exact timescales of planet formation are still being narrowed down. We know from observations of solids around both young protostars and more evolved T-Tauri stars that disks contain a large amount of μm to cm sized dust particles [3]. These dust particles will eventually congeal into larger, rocks called planetestimals that will ultimately coalesce into planet-cores.

The first phases of planet formation begin with the smallest, μm-sized dust particles growing in size by colliding into other particles and then sticking together [3]. The stickiness of the dust grains is dependant on the grain composition, ice mantles, and the dust grain's shape. After enough colliding and sticking has happened, the dust grains are now mm-sized particles and begin decoupling from the gas. At this point, the smaller, μm-sized dust particles experience the same pressure gradients as the gas while these larger, mm-sized (and cm-sized) dust grains move at swifter velocities that cause them to drift towards the central star. This decoupling happens on timescales faster than potential planet growth (as short as 100 years).

One way to overcome the dust drifting are barriers/traps within the disk that stop the grain's inward radial motion [41, 42]. Within these dust traps, the mm-sized grains have time to grow into planetesimals. Observationally, these dust traps appear as rings in imaging of the dust-grains. Once the planetesimals have successfully formed, previous properties give way to gravitationally dominated ones as the planetesimals grow to either a terrestrial planet or the core of a gas giant.

1.4 Protoplanetary Disk Properties

1.4.1 Disk Structure

Within protoplanetary disks, solids usually represent a small portion of its total mass — the accepted standard gas-to-dust ratio is 100:1 — but play a fundamental role in planet formation ([3] and refs therein). Estimates for the solid masses within individual disks are subject to a range of uncertainties due to assumptions of the emitting particles and are most likely lower bounds. Gas mass estimates face similar problems for different reasons — not only is the most abundant gas, H_2, unable to be detected, but the standard gas tracer, CO and its isotopologues ^{13}CO and $C^{18}O$, generate "low" mass estimates with standard ISM abundance ratios and gas-to-dust ratios [43]. Comparatively, density measurements are equally assumption-ridden.

Temperature information about disks can be estimated through a few methods. The most common effect of temperature gradients within the disk is witnessed through freeze-out in gas molecules, gas depositing into ice onto dust particles. Each molecule has a different freeze-out temperature and so measuring the radii and height where a range of gas emission stops illustrates the temperature structure of the disks [1]. Often, this is easier to do when the disk is observed at higher inclinations (i.e. [44]) because CO emission becomes optically thick at the warm surface layers of the disk. The freeze-out of molecules derivative of other molecules can trace the freeze-out of its parent molecule; i.e. DCO^+ is a derivative of CO and therefore its freeze-out coincides with the freeze-out of CO.

Since planet formation and disk evolution are happening simultaneously within protoplanetary disks, the two heavily influence both each other and the observable disk structures. Improved spatial resolution has allowed for exploration of the physical substructures within protoplanetary disks. Rings, gaps, spirals and arcs have been observed in a variety disks, with substructure appearing into the inner most radii [45, 46, 47]. These observed morphologies are indicative of the properties of and the processes happening within each disk: mass-loss, giant planets, low-mass planets, dust evolution, etc. A range of substructures are expected to be caused by planets, although most are not unique to only embedded planets; spiral wakes, gaps, meridional flows, circumplanetary disks, etc. Circumplanetary disks have been claimed to be observed in the PDS 70 system [48, 49].

Vertical substructures in disks can be inferred by the detections of variability of infrared surface brightness, most likely caused by disk shadowing and stellar obscuration due to asymmetrical vertical substructure in the inner disk. A recent study of mid-inclination protoplanetary disks found vertical substructures in CO line emission that align with rings and gaps in millimeter dust observations [50].

1.4.2 Disk Chemistry

The chemistry within protoplanetary disks not only determines the individual abundances of molecular species, but also the distribution of the molecules throughout the disk and other physical conditions of the disk itself (e.g. the review Oberg & Bergin (2021) [1]). These chemical processes begin with the inception of the star and evolve throughout the different stages of star formation (e.g. reviews, [51, 52]). The chemical genesis of each molecular species depends on a variety of initial conditions, such as disk density structure, viscosity, stellar irradiation, and atomic/molecular abundances.

The initial conditions of stars are related to the material of the local interstellar medium (ISM) which consists primarily of hydrogen and helium followed by oxygen, carbon, and nitrogen dominating the heavier elements. The major volatile carriers of the heavier elements are H_2O, CO, and N_2, which remain important through the planet-forming phases and are central to understanding disk chemistry. These volatile reservoirs, along with the first generation of organics, form during the molecular cloud stage through a combination of gas-phase reactions and dust grain surface reactions [53]. During the protosellar stage, the major volatile reservoirs are mostly conserved while the organic molecules become more complex.

The strong vertical and radial temperature and density gradients that result from stellar high-energy photons lead to more diverse chemical processes within the protoplanetary disk

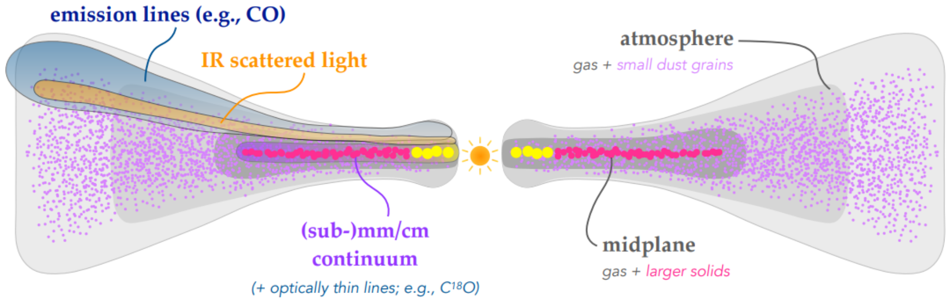

Figure 1

A cartoon schematic of a disk structure viewed in cross-section. The gas is denoted in grayscale, and solids are marked with exaggerated sizes and colors. The left side highlights the approximate locations of emission tracers; the right side defines some structure and contents terminology.

Figure 1.3: Cartoon from Andrews et al. (2020) [3] illustrating a cross-section protoplanetary disk structured.

phase, causing a layered chemical structure [1]. The vertical structure of the disk can be divided into three regions: the upper layer, the midplane, and the warm intermediate molecular layer (represented in Fig 1.3). The upper layer is similar to a dense photon-dominated region (PDR), which consists of simple ions, neutral species, and small dust grains due to UV and X-Ray radiation ionizing atoms and photodissociating most molecules. The midplane lacks most gas-phase molecules due to freeze out and lack of UV photons and is instead composed of ices, stuck to dust grain surfaces. When a molecule freezes it can no longer participate in gas-phase chemistry, although it may still remain chemically active as ice layers on dust grains. The intermediate layer is composed of simple and complex molecules in the gas phase and is dominated by rapid gas-dust interactions. The UV radiation has been attenuated enough to allow molecules to survive in this region, but not completely gone to stop ion-molecule chemistry. The chemistry in deeper disk layers is driven by X-Rays, which can penetrate the disk more deeply than UV.

The radial regions of the disk are more naturally separated into 'inner' ($<\sim 5$ AU) and 'outer' ($>\sim 5$ AU) regions. The inner region is characterized by high temperatures ($\sim 100 - 1000$ K) and densities ($> 10^{12} \text{cm}^{-3}$). This higher density causes an increase in three body reactions, such as the collision of 2 hydrogen atoms and a third particle to make molecular hydrogen. In the outer regions of the disk, the chemistry is instead driven by cosmic rays and high energy radiation. The high energy of the photons irradiating this region creates various ions which leads to ion-molecule driven chemistry. The outer regions are also heavily effected by the freeze-out of molecules due to low temperatures (< 100 K). The radial location where individual molecules freeze out is also referred to as the molecule's 'snow line', which is unique to the different stages of the disk to both the star and disk evolving.

Gas-phase, gas-grain, and grain surface processes within the disk control and regulate the growth of planetesimals ([1] and refs therein). A few examples of regulating processes include dust grain growth and migration, disk gas dispersal, and the buildup of grain ice mantles. These dynamical processes not only affect planet formation but also affect the structure of the protoplanetary disk, therefore the effects of the processes could be seen in the molecular emission line from the disk. Combining model predictions and suites of multi-wavelength, high-resolution observations, astrophysicists can test the dynamical processes leading to planet formation within nearby disks.

1.5 Studying Protoplanetary Disks

The structure of protoplanetary disks can be observed through probing different parts of the electromagnetic spectrum because of its large temperature gradient, hot near the star and cold at the disk's edges, and complex chemical structure. Imaging of the disk, and resolving disk structure and substructure, is best performed through infrared imaging of the scattered-light or radio imaging of the thermal emission (e.g. [54],[46],[55]). The gas can be detected in most regimes but can be observed in the radio regime through the detection of molecular rotational emission lines, emission from the abrupt change in angular momentum of the quantum particle. CO is the easiest molecule to detect from radio rotational transition lines because of its relatively large abundance and its large dipole moment, which translates to a low critical density for excitation.

While historically, disks around young stars have been observed for a long time, the first resolved images of disks began in the 1990s with optical high resolution imaging via HST (e.g.

[56]). Higher resolution imaging is needed to image the disk substructures that are crucial to quantify to understand planet formation. Over the past three decades, our observational technologies have evolved and now instruments like VLT/SPHERE can obtain IR scattered-light images of disks with <0.1" resolution (e.g., [57]).

Infrared spectroscopy has often been a useful tool in stellar astrophysics but it is also home to many accretion and accretion-driven process signatures (e.g. [58]). As discussed earlier, the process of accretion from disk to star is an important part of disk evolution and is important to quantify to understand the parameters of a protoplanetary disk.

The sub-mm regime is both ideal for imaging the thermal continuum emitted from the bulk of disk solids as well as host to a wealth of molecular line emissions. Interferometers are an invaluable tool for high resolution astronomy and spectroscopy. In radio astronomy, interferometers are the only feasible way to achieve angular resolution comparable to that routinely obtained with optical/IR telescopes. To get similar resolutions with individual telescopes, the telescopes have to have prohibitively large diameters which are in general not technologically attainable. Interferometers are multiple telescopes measuring the interference pattern of light in tandem. The distance between the telescopes – called the *baseline* – determines the angular resolution that can be achieved for a given telescope pair along the pair's position angle (as projected on the sky).

The Atacama Large Millimeter/submillimeter Array (ALMA) is a powerful radio interferometer facility able to observe over the frequency range 84 GHz to 950 GHz, corresponding to wavelengths of 3.6 mm down to 300 microns. It is located in the Atacama desert in Chile, at an altitude of 5000 m above sea level. ALMA has 66 total antennas at full capacity (54 12-m and 12 7-m antennas) and the arrangement of these antennas can vary from arrays with extended baselines (maximum baselines of 16 km) to compact arrays with shorter baselines (maximum baselines of 160 m). This allows for varying distributions of baselines, the minimum baseline being limited by the distance between the two telescopes closest to each other. Due to the wealth of molecular rotational emission lines within 84 GHz to 950 GHz, ALMA has been at the forefront of breakthroughs in the physical and chemical evolution of protoplanetary disks (e.g., [59, 60, 45, 8]).

1.5.1 Radiative Transfer Modelling

While there are a multitiude of ways to effectively model protoplanetary disks, each with their own pros and cons, this thesis takes advantage of models that concentrate on effectively modelling the radiative transfer happening in this disk. MCFOST is a continuum 3D radiative transfer code based on the Monte Carlo method, originally developed at the Institut de Planétologie et d'Astrophysique de Grenoble and then updated to include dust heating and continuum re-emission [61, 62]. It is very widely used for the interpretation the 2D thermal continuum, scattered light images, and molecular line images of the disks in terms of 3D disk density, temperature, and chemical structures.

1.6 The Epsilon Chameleon Association

This thesis utilizes the ϵ Cha Association (ϵCA), at only 100 pc, as the nearest opportunity to probe pre-MS stars in the crucial age for planet formation of $\sim$ 5 Myr [63, 64]. Chapter 2 of this thesis presents a Gaia DR2 study of ϵCA that reconsiders the membership of it along with presents updated statistics for the association. Constraining the properties and membership of this NYMG both provides potential new young stars to probe (as in the case of 2MASS J11550336-7919147) and gives the proper context to further understand how stellar and planet formation vary with mass within an age group. Two members provide unique, and under-examined, opportunities to better understand brown dwarf and planet formation and will be the topics of my thesis: 2MASS J11550336-7919147 (henceforth 2M1155B) is the topic of Chapter 3 and T Cha the focus of Chapter 4.

2MASS J11550336-7919147: is the unexplored companion to 2MASS J1155-7919A (henceforth 2M1155A) [65]. The co-moving pair have a projected separation of 5.75", corresponding to 582 AU at PA 227.9°. 2M1155A is a mid-M star [66] and displays modest reddening, E(B-V) $\sim$ 0.3 [63]. The nature of 2M1155B has yet to be narrowed down, presenting the motivation for this thesis work.

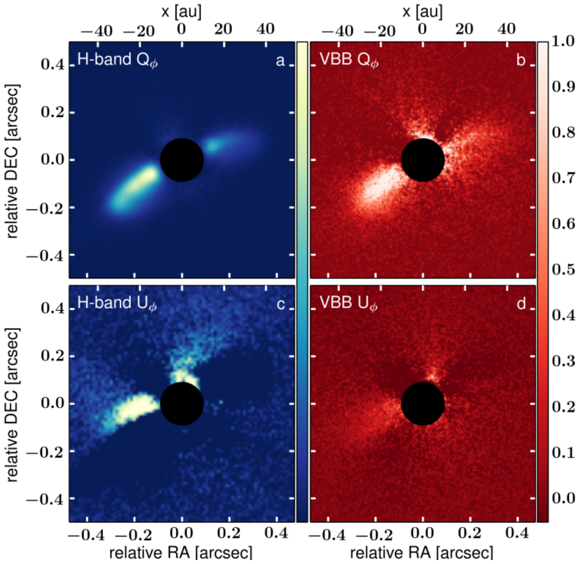

Figure 1.4: IRDIS-DPI H-band and ZIMPOL P2 VBB-filter $Q\phi$ (top row) and $U\phi$ (bottom row) images from Pohl et al. (2017) [4]. The black circle in the center represents the location of the coronagraph.

T Cha: is an intermediate-mass (∼1.4 $M_\odot$ [66]) star that lies at D $=$ 109 pc [34] which hosts a transition disk with an mm-sized dust inner cavity of radii 13 AU (Olofsson et al. 2013). A transition disks are a subcategory of protoplanetary disks that have are more evolved with large inner cavities cleared by forming planets and/or disk photoevaporation processes. T Cha hosts the nearest-known example of a highly inclined disk ($i = 67 \pm 5°$, Huelamo et al. (2015) [12]). Sacco et al. (2014) [67] present an H_2 gas mass estimate for the disk of 2.4 $\times 10^{-4}$ $M_\odot$ and a corresponding dust mass of 2.0 $\times 10^{-5}$ $M_\odot$. T Cha has been observed in scattered light (Fig 4., Pohl et al. (2017) [4]), which reveals the brighter left-hand side of the highly inclined disk.

The analysis of these two objects will facilitate the furthering of our knowledge in planet and stellar formation by probing the conditions of disks at the crucial age of 5 Myr in disks that are close enough to study in detail. The disk around 2M1155B as seen in the NIR spectra presented in Chapter 3 is a rare examination of disks around very low-mass, pre-MS stars viewed at a high inclination. Also at a high inclination, the disk surrounding T Cha as imaged via the CO emissions lines from the disk will allow constraints to be put on the vertical temperature and density structure of gas and dust in disks during the intermediate phases of planet formation.

Chapter 2

Gaia-based Isochronal, Kinematic, and Spatial Analysis of the Epsilon Cha Association

The following Chapter was originally published as ["Gaia-based Isochronal, Kinematic, and Spatial Analysis of the ϵ Cha Association", D.A. Dickson-Vandervelde, E. Wilson, and J. Kastner, The Astronomical Journal, 161:87, February 2021

2.1 Introduction

Nearby Young Moving Groups (NYMGs) serve as laboratories for the study of stars and their planetary offspring during their first stages of development, i.e., over the first tens of Myr after these young stars and planets have emerged from their birth clouds [68]. The age range spanned by coeval NYMGs (a few Myr to several × 100 Myr) provides unique opportunities to study stellar properties over a range of masses and temperatures at specific snapshots of pre-main sequence (pre-MS) and young MS evolution. Thanks to the proximity (< 120 pc) of NYMGs, it is possible to observe and characterize an entire stellar population, down to the diminutive brown dwarfs (e.g., [69, 70]) and even massive planets (e.g., [71]). The younger

NYMGs (ages <25 Myr) feature Sun-like stars orbited by gas-rich circumstellar disks that are likely sites of ongoing planet formation (e.g., [67]), while dusty debris disks are found among groups at more advanced ages (e.g., [72]).

The precise astrometric and photometric data flowing from the Gaia Space Astrometry mission [33, 34] is particularly useful to the study of NYMGs. Gaia Data Release 1 and the subsequent Gaia Data Release 2 (hereafter DR2) has resulted in a leap in our understanding of the membership of previously known NYMGs and, hence, their fundamental properties, such as ages, mass distributions, internal kinematics, and stellar multiplicity statistics (e.g., [73, 2, 6]). Gaia DR2 data have also led to the identification of previously unknown NYMGs (e.g., [74]).

Here, we present an analysis of Gaia DR2 data for the ϵ Chamaeleontis Association (hereafter ϵCA). At an estimated age of 3-5 Myr ([63], henceforth M+13), ϵCA is the youngest NYMG within $\sim$100 pc of Earth ([68], and refs. therein). Its relative youth and consequent large disk frequency (29%, M+13) — combined with its position well in the foreground of the Cha star formation complex (see Fig. 2 of M+13) — make it a key NYMG for purposes of studying planet formation and pre-MS stellar evolution, without the complication of pervasive ambient or intervening molecular cloud material.

The identification and study of stars belonging to ϵCA began in association with the study of the neighboring η Cha cluster [75]. Chandra X-ray Observatory observations of the Herbig Ae/Be star HD 104237A ϵCA led to further characterization of the group and discovery of new members [76]. HD 104237A has a close, T Tauri-type companion (HD 104237B), both of which are orbited by a CO-rich circumbinary disk [77]. An additional three stars are thought to be part of the HD 104237 system, two of which form another close binary (HD 104237D+E); HD 104237D shows evidence of accreting plasma [78].

In addition to HD 104237A, the members of ϵCA include two stars with gas-rich circumstellar disks, MP Mus and T Cha; these stars represent two of only four known examples of solar-mass stars with protoplanetary disks that lie within $\sim$100 pc of Earth [79, 67]. Among these four, the disk orbiting MP Mus — a single, 1.2 $M_\odot$ star lying a mere 98 pc from Earth

— may be most closely analogous to the solar nebula. Meanwhile the T Cha disk is the only nearby transition disk that is viewed at a high inclination (73°), and furthermore displays evidence for an embedded planet [13].

The most recent comprehensive study of the membership of ϵCA (M+13) was reliant on pre-Gaia stellar kinematics and photometry. With the benefit of Gaia DR2 data, we have revisited and refined the membership, kinematics, and color-magnitude distribution of ϵCA, with the primary goal of firmly establishing its position along the NYMG age sequence. We have also reexamined the multiplicity and detailed spatial distribution of disk-bearing ϵCA members. In Section 2, we discuss the sample selection and flags and caveats of the available Gaia DR2 data. In Section 3, we describe our methods, including determination of an empirical isochrone and kinematics for the ϵCA. In Section 4, we present the results from this analysis. In Section 5, we discuss the implications of these results, including the age of ϵCA relative to other young NYMGs.

2.2 Sample Selection

Table 2.1 lists all (65) stars we considered for ϵCA membership for which Gaia DR2 data is available. The majority of these ϵCA candidates were drawn from M+13. Those authors gathered all proposed members of ϵCA from the previous literature (52 in total) and assessed membership via their (pre-Gaia) proper motions and their spectral properties (such as Li absorption line equivalent widths and infrared excesses). The set of 35 stars initially considered here as *bona fide* ϵCA members then consists of M+13's "confirmed members" (M+13 Table 7). Ultimately, we also considered the 6 "provisional members" and 11 "rejected stars" from the M+13 study (§2.4.1) as well as 15 stars from Gagné and Faherty (2018)[2] (henceforth GF18) that GF18 designated as potential ϵCA members (§2.4.1.4).

We searched the Gaia archive for DR2 counterparts to these 67 stars from the MF+13 and GF18 studies, using a 0.25" search radius centered at the position listed in M+13. Unique DR2 counterparts were identified for all stars listed in Table 2.1 comprising a total of 65 of the 67 stars searched, though not all of these counterparts had parallaxes and colors. All

Table 2.1: Gaia Data and RVs for Candidate ϵCA Members

Name[a]	RA deg	Dec deg	π mas	σ	G mag	σ	G−R_P mag	σ	PMRA mas/yr	σ	PMDec mas/yr	σ	RV km/s	σ	RUWE[b]	RV ref[c]
HD 8279*	142.0874	-78.2597	8.504	0.025	8.92760	0.00038	0.3737	0.0025	-28.211	0.043	20.350	0.046	12.76	0.2	1.05	2
CP-68 1388 †	164.4553	-69.2333	8.592	0.029	10.0229	0.0024	0.6763	0.0070	-34.842	0.051	3.552	0.044	15.9	1.0	0.93	12
VW Cha*	167.0058	-77.7079	–	–	12.187	0.020	1.425	0.018	–	–	–	–	–	–	–	
TYC 9414-191-1‡	169.1200	-78.4224	1.564	0.022	10.523674	0.00025	0.86718	0.00067	-38.372	0.040	2.460	0.033	–	–	0.91	–
2MJ11183572-7935548 †	169.6478	-79.5986	10.57	0.15	13.8687	0.0027	1.3726	0.0043	-41.76	0.26	4.98	0.24	19.3	1.6	3.35^+	8
RX J1123.2-7924*	170.7311	-79.4123	9.379	0.021	12.8674	0.0016	1.0036	0.0041	-31.670	0.040	-17.443	0.038	2.7	2.9	1.14	8
HIP 55746*	171.3217	-84.9545	11.077	0.138	7.53435	0.00044	0.3524	0.0021	-46.19	0.16	11.92	0.16	20.9	1.2	1.46	3
2MJ11334926-7618399*	173.4550	-76.3111	5.410	0.060	15.56704	0.00081	1.3373	0.0010	-22.41	0.11	-0.561	0.087	–	–	1.07	–
RX J1137.4-7648*	174.3794	-76.7997	11.988	0.021	13.52653	0.00079	1.0494	0.0022	-60.544	0.041	-8.935	0.032	14.0	5.0	1.16	8
2MJ11404967-7459394 †	175.2063	-74.9942	10.397	0.069	16.4291	0.0018	1.4466	0.0044	-42.74	0.13	-2.28	0.10	10.3	1.0	0.94	8
2MJ11411722-7315369#	175.3211	-73.2602	10.416	0.052	15.47804	0.00084	1.3229	0.0024	-42.047	0.093	5.672	0.082	–	–	1.07	–
TYC 9238-612-1*	175.3646	-73.7841	6.124	0.021	10.5976	0.0012	0.5663	0.0035	-35.747	0.041	10.938	0.036	–	–	1.33	–
2MJ11432669-7804454 †	175.8603	-78.0793	5.54	0.56	14.8931	0.0072	1.321	0.022	-43.98	0.92	-6.52	0.75	15.6	1	10.51^+	8
2MJ11432968-7418377#	175.8729	-74.3105	10.063	0.039	14.17633	0.00066	1.2213	0.0022	-40.621	0.073	-3.026	0.067	–	–	1.19	–
RX J1147.7-7842 †	176.9496	-78.698	9.894	0.039	12.3523	0.0012	1.1840	0.0028	-41.660	0.075	-4.265	0.065	16.1	0.9	1.28	8
RX J1149.8-7850 †	177.3818	-78.8503	9.918	0.025	11.9324	0.0043	1.028	0.015	-41.876	0.047	-4.265	0.040	13.4	1.3	1.19	8
RX J1150.4-7704 *	177.6171	-77.0773	6.551	0.031	11.5250	0.0016	0.7773	0.0042	-42.744	0.054	-11.047	0.040	–	–	1.26	–
RX J1150.9-7411 †	177.6868	-74.1871	10.63	0.18	13.4567	0.0050	1.324	0.012	-39.50	0.32	-8.08	0.29	15.0	1.2	6.01^+	8
2MJ11550485-7919108 †	178.7692	-79.3198	9.886	0.058	14.8180	0.0017	1.3502	0.0053	-41.18	0.13	-4.336	0.086	–	–	1.08	–
T Cha †	179.3054	-79.3588	9.122	0.083	12.97	0.11	1.61	0.35	-42.00	0.12	-9.245	0.080	6–30	–	0.91	2,5,10
RX J1158.5-7754B †	179.6109	-77.9126	9.662	0.035	13.2023	0.0027	1.1713	0.0081	-39.573	0.064	-5.686	0.060	13.0	2.0	1.22	11
RX J1158.5-7754A †	179.6165	-77.9083	9.518	0.035	9.9798	0.0011	0.7888	0.0033	-39.660	0.063	-12.844	0.070	14.02	1.82	1.66	2,8,12
HD 104036 †	179.646	-77.8254	9.566	0.038	6.69296	0.00053	0.1646	0.0041	-41.286	0.065	-7.762	0.073	12.6	0.5	1.23	3
CXOU J115908.2-781232‡	179.7824	-78.2089	9.425	0.062	15.2563	0.00063	1.3139	0.0022	-38.62	0.14	-5.181	0.091	15.1	0.2	1.24	8
ϵ Cha AB†	179.9056	-78.2219	–	–	4.7816	0.0080	-0.1505	0.0086	–	–	–	–	13	3.7	–	11
RX J1159.7-7601 †	179.9254	-76.024	10.025	0.023	10.8095	0.0023	0.7694	0.0058	-41.025	0.043	-6.190	0.038	13.0	3.7	0.96	2,8
2MJ12000269-7444068#	180.0105	-74.7352	10.067	0.049	14.3241	0.0011	1.2431	0.0028	-42.047	0.079	-5.699	0.071	–	–	1.24	–
HD 104237A †	180.0204	-78.193	9.226	0.058	6.5427	0.0018	0.2213	0.0074	-39.31	0.11	-6.212	0.083	13.52	0.39	1.55	4
HD 104237D †	180.0336	-78.1943	9.885	0.061	13.0206	0.0015	1.1981	0.0065	-38.87	0.13	-3.195	0.098	–	–	1.53	–
HD 104237E †	180.0379	-78.1951	9.796	0.034	11.838	0.028	1.16	0.11	-42.907	0.074	-4.418	0.051	–	–	1.54	–
2MJ12005517-7820296 †	180.2291	-78.3415	9.713	0.082	15.5826	0.0012	1.4005	0.0040	-40.59	0.14	-4.96	0.12	10.7	1.3	1.17	8
HD 104467 †	180.412	-78.9881	10.14	0.17	8.4285	0.0022	0.5145	0.0059	-41.11	0.26	-5.41	0.26	12.81	0.96	5.17	2
2MJ12014343-7835472 †	180.4302	-78.5965	9.53	0.11	17.115	0.021	1.166	0.069	-41.32	0.19	-6.33	0.14	20.0	0.6	1.28	8
USNO-B 120144.7-781926 †	180.4343	-78.3241	9.819	0.063	15.2758	0.0076	1.372	0.020	-41.43	0.11	-6.105	0.088	14.9	1.1	1.08	8
CXOU J120152.8-781840 †	180.4681	-78.3115	9.735	0.068	14.9821	0.0012	1.3319	0.0026	-40.59	0.12	-6.88	0.10	16.5	1.1	1.14	8
RX J1202.1-7853 †	180.5145	-78.8837	10.011	0.046	11.5100	0.0030	1.0059	0.0088	-45.122	0.081	-4.124	0.069	17.1	0.2	1.63	5
RX J1202.8-7718‡	180.7269	-77.3106	9.606	0.035	13.3749	0.0026	1.1762	0.0080	-39.625	0.072	-6.044	0.059	14.4	0.6	1.21	7
RX J1204.6-7731 †	181.1498	-77.5263	9.922	0.034	12.5714	0.0018	1.1513	0.0053	-41.364	0.056	-6.397	0.052	10.4	2.0	1.20	6
TYC 9420-676-1 *	181.2384	-79.5346	3.700	0.080	10.23947	0.00063	0.4443	0.0016	-38.16	0.16	-1.00	0.18	–	–	2.95	–
HD 105234‡	181.7721	-78.7412	9.566	0.035	7.41947	0.00041	0.2247	0.0028	-40.971	0.058	-9.41	0.057	–	–	1.15	–
2MJ12074597-7816064*	181.9407	-78.2685	9.454	0.058	14.55144	0.00073	1.2293	0.0021	-38.424	0.091	-6.319	0.077	15.2	1.9	1.33	8

Table 2.2: *(Continued)*

Name^a	RA deg	Dec deg	π mas	σ	G mag	σ	G−R$_P$ mag	σ	PMRA mas/yr	σ	PMDec mas/yr	σ	RV km/s	σ	RUWE^b	RV ref^c
RX J1207.7-7953 †	181.9501	-79.8785	10.016	0.030	13.3403	0.0022	1.1860	0.0057	-42.058	0.056	-7.113	0.052	15.0	0.7	1.12	8
HIP 59243‡	182.2811	-78.7813	10.019	0.033	6.79373	0.00043	0.1889	0.0034	-43.364	0.062	-7.619	0.06	–	–	1.10	–
HD 105923 †	182.9084	-71.1767	9.400	0.036	8.83653	0.00083	0.5367	0.0035	-38.721	0.062	-7.423	0.051	14.34	1.06	0.87	1,2,12
RX J1216.8-7753 †	184.1906	-77.8927	9.820	0.039	12.9206	0.0037	1.132	0.010	-39.825	0.072	-9.074	0.072	14.0	2.0	1.17	6
RX J1219.7-7403 †	184.9315	-74.0659	9.865	0.027	12.1400	0.0016	1.0187	0.0042	-40.323	0.043	-9.256	0.039	13.86	1.89	0.96	2
RX J1220.4-7407 †	185.0901	-74.1277	6.71	0.70	11.9406	0.0020	1.0706	0.0050	-40.9	1.2	-4.1	1.4	12.3	0.4	38.28$^+$	6
2MJ12203396-7135188#	185.1411	-71.5886	10.773	0.057	13.21947	0.00084	1.2486	0.0019	-42.573	0.096	-8.571	0.070	–	–	1.28	–
2MJ12203619-7353027#	185.1502	-73.8842	10.007	0.035	13.1409	0.0010	1.1424	0.0024	-40.621	0.069	-9.326	0.050	–	–	1.12	–
2MJ12210499-7116493 †	185.2703	-71.2804	10.055	0.024	11.2032	0.0028	0.8874	0.0079	-40.416	0.043	-9.647	0.034	11.44	2.53	1.02	9
2MJ12220068-7001041#	185.5022	-70.0178	10.008	0.047	14.0236	0.0011	1.2371	0.0045	-41.229	0.096	-10.474	0.063	–	–	1.23	–
2MJ12222238-7137040#	185.5926	-71.6178	10.516	0.027	12.5299	0.0081	1.105	0.023	-41.843	0.044	-9.962	0.043	–	–	1.06	–
2MJ12224862-7410203#	185.702	-74.1724	10.605	0.089	16.1751	0.0024	1.4774	0.0068	-42.57	0.15	-9.27	0.13	–	–	1.18	–
2MJ12255824-7551116#	186.4921	-75.8533	10.049	0.065	15.36554	0.00074	1.3318	0.0026	-41.23	0.11	-10.46	0.10	–	–	1.20	–
2MJ12324805-7654237#	188.1995	-76.9067	11.69	0.91	12.8346	0.0012	1.1960	0.0033	-41.84	1.67	-13.49	1.32	–	–	36.83$^+$	–
2MJ12332483-6848553#	188.3531	-68.8154	10.061	0.086	15.7118	0.0012	1.3676	0.0039	-41.43	0.13	-12.51	0.11	–	–	1.16	–
2MJ12351540-7043079#	188.8135	-70.7189	10.705	0.066	15.70148	0.00068	1.3844	0.0026	-43.72	0.11	-12.639	0.094	–	–	1.03	–
RX J1239.4-7502 †	189.838	-75.0443	9.646	0.027	9.9751	0.0017	0.6679	0.0048	-38.214	0.044	-12.368	0.042	13.62	2.8	0.97	9
2MJ12421315-6943484#	190.5543	-69.7302	10.062	0.083	15.1444	0.0011	1.3551	0.0039	-39.50	0.14	-12.77	0.10	–	–	1.24	–
RX J1243.1-7458∗	190.7219	-74.98	7.99	0.37	13.7652	0.0044	1.186	0.011	-17.25	0.66	-2.63	0.53	13.5	7.0	10.71$^+$	8
2MJ12425584-7034207#	190.7321	-70.5725	10.062	0.078	15.97496	0.00098	1.4049	0.0031	-40.47	0.12	-13.20	0.12	–	–	0.99	–
2MJ12473611-7031135#	191.9000	-70.5206	10.012	0.031	13.26920	0.00065	1.1498	0.0016	-40.249	0.048	-14.241	0.045	–	–	1.12	–
CD-69 1055 †	194.6061	-70.4804	10.549	0.029	9.6062	0.0027	0.6388	0.0076	-41.001	0.047	-16.459	0.045	11.18	1.67	1.01	1,2,8
CM Cha‡	195.5560	-76.6328	5.152	0.024	12.5599	0.0043	1.001	0.012	-20.990	0.040	-9.144	0.041	–	–	1.15	–
MP Mus †	200.531	-69.6368	10.115	0.031	9.9521	0.0030	0.7207	0.0087	-38.289	0.044	-20.204	0.045	11.6	0.2	0.98	12

NOTE: a) M+13 *bona fide* members are indicated by †, M+13 provisional members are indicated by ‡, M+13 rejected members are indicated by ∗, and GF18 members are indicated by #. Names that begin with 2M are 2MASS designations.

b) Values marked with + have high astrometric excess noise.

c) References for radial velocities: ^{1}[80] ^{2}[34] ^{3}[81], ^{4}[82], ^{5}[83], ^{6}[84], ^{7}[85], ^{8}[63], ^{9}[86], ^{10}[87],^{11}[88], ^{12}[89]

Gaia counterparts met or exceeded the minimum number of Gaia visibility periods ($n_{\mathrm{vis}} > 5$) recommended by Lindegren et al. (2018) [90].

To assess the quality of the Gaia data for individual stars, we applied three metrics: the Re-normalized Unit Weight Error (RUWE) [91], astrometric excess noise, and photometric excess [34]. The astrometric Unit Weight Error (UWE), in its renormalized form (RUWE), is useful to determine when data are potentially unreliable based on Gaia measurement uncertainties alone. Following Lindegren (2018) [91], we flag data with RUWE > 1.4. Note that this RUWE threshold is implicitly based on a star's $G_{B_P} - G_{R_P}$ color, whereas the color-magnitude diagram analysis carried out here (Sec 2.3.1) uses Gaia $G - G_{R_P}$ colors. We also utilitzed `astrometric_excess_noise` to assess the quality of the astrometric data, flagging those stars with `astrometric_excess_noise` $> 0.1 \times \pi$ as having potentially large parallax uncertainties. We used Gaia's `phot_bp_rp_excess_factor`, E, to flag stars that did not satisfy $1.0 + 0.015(G_{B_P} - G_{R_P})^2 < E < 1.3 + 0.06(G_{B_P} - G_{R_P})^2$. As discussed in Gaia Collaboration et. al (2018) [34], stars that fall outside of this range of $G_{B_P} - G_{R_P}$ have colors that may not be trustworthy.

The RUWE values for all 65 stars are listed in Table 2.1. The results of the astrometric excess noise and photometric excess tests are also noted in Table 2.1. Two stars, T Cha and HD 104237E, fail the `phot_bp_rp_excess_factor` test. In Figure 2.1, we display the Gaia DR2 color-magnitude diagram (CMD) positions of the 30 (of 35) *bona fide* M+13 ϵCA members that have viable DR2 parallaxes and photometry (see §3.1), with the results of the preceding data-flagging exercise indicated.

2.3 Analysis

2.3.1 Empirical Single-Star Isochrone

To ascertain the empirical isochrone defined by single-star members of NYMGs like ϵCA, we have developed the Single-star Locus Fitting Routine (SLFR, Dickson-Vandervelde et al. 2020, in prep.). The SLFR utilizes a recursive method to fit a polynomial to the color-magnitude

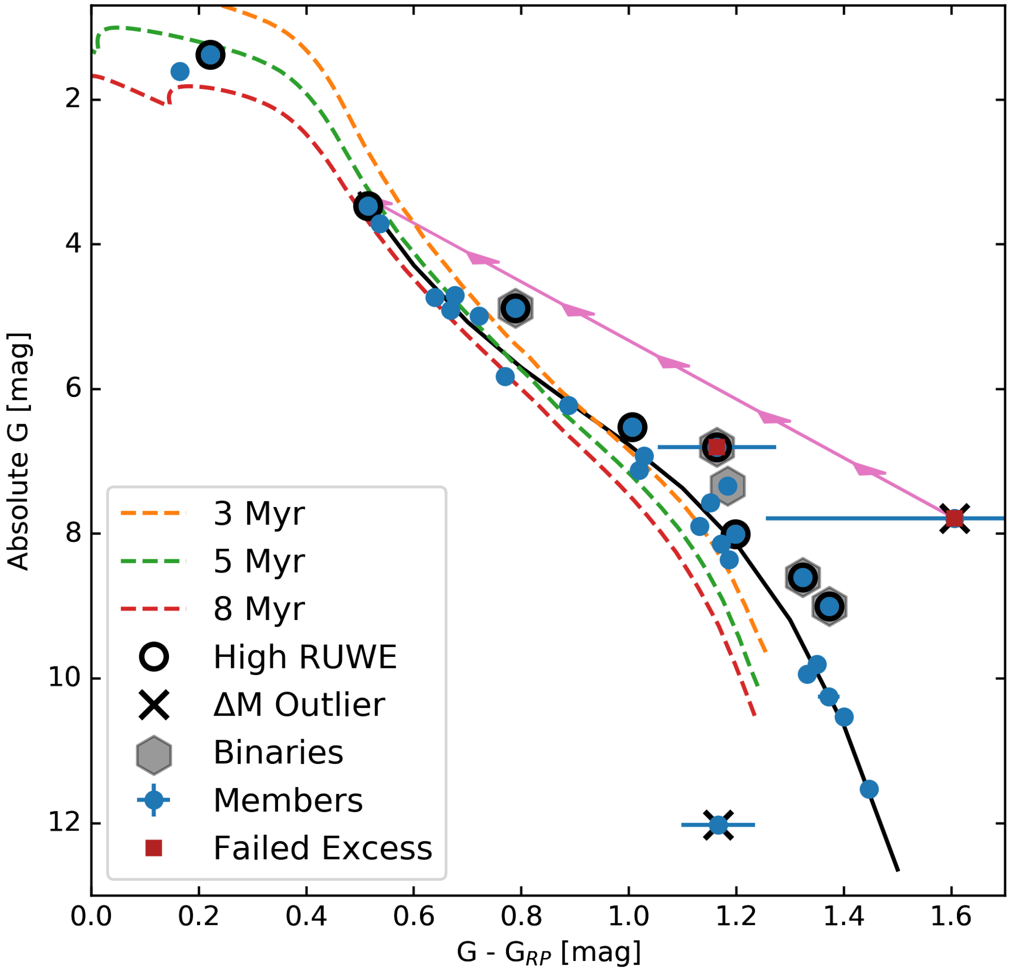

Figure 2.1: Gaia DR2 color-magnitude diagram (CMD) for the 30 M+13 *bona fide* members (blue circles) included in empirical single-star locus fitting (SLFR) analysis (Sec 2.3.1). The best-fit empirical isochrone obtained from the SLFR method is represented by the black curve. Three theoretical isochrones [5] for ages of 3, 5, and 8 Myr (orange, green, and red dashed lines, respectively) are also overlaid on the data. Stars with high RUWE values (low-accuracy astrometry) are marked with black, open circles; stars failing the color excess factor test (bad photometry) are marked with red squares; and stars that are outliers in the magnitude offset are marked with crosses. Five stars identified as candidate photometric binaries (via the empirical single-star isochrone fitting) are denoted by grey hexagons. Errors are displayed as horizontal and vertical bars in blue; where no error bar is seen, the errors are smaller than the symbols. The pink line (with arrows) represents the reddening vector inferred for T Cha (the red square and cross at $G - G_{RP} \sim 1.6$), i.e., $E(G - G_{RP}) = 1.1$ mag and $A_G = 4.5$ mag (see Sec 2.4.1.3).

diagram (CMD) of a set of NYMG members, identifying and rejecting outliers at each iteration. Between iterations, any star with with a magnitude greater than 2σ is rejected before refitting the polynomial. The final result is a polynomial that represents the best fit to the single-star locus of the group across well-sampled regions of color-magnitude space, as well as a list of candidate photometric binaries, i.e., stars that lie significantly above, but within $\sim$0.75 mag of, the single-star locus. The resulting best-fit polynomial then effectively represents the group's empirical single-star isochrone.

Only 32 of the 33 *bona fide* members of ϵCA listed in Table 2.1 have the DR2 parallaxes and photometry necessary for SLFR analysis; we further excluded two stars whose parallaxes appear incompatible with ϵCA membership (see § 2.4.1.2). Figure 2.1 illustrates the results of the SLFR method as applied to the remaining 30 stars. The SLFR-generated empirical isochrone (polynomial) is only well fit where there is a good sampling of stars in color-magnitude space and is particularly unreliable (and is therefore not plotted) in the bluest region of the CMD ($G - G_{RP} < 0.5$).We found a 4th-order polynomial to be sufficient to match the color-magnitude data without introducing artifacts in poorly sampled regions. The final polynomial is given by $G = 1.28c^4 + 8.44c^3 - 28.9c^2 + 33.17c + 7.18$, where G is absolute G magnitude and c is $G - G_{RP}$ color. This fit provided an RMS in G of 0.61 magnitudes. Hereafter we refer to this polynomial as the empirical (5 Myr) isochrone.

The empirical isochrone is evidently a better match to the ϵCA color-magnitude data than any of the theoretical isochrones (from [5]) plotted in Figure 2.1. While the 5 Myr and 8 Myr theoretical isochrones follow the SLFR-generated empirical isochrone in the blue CMD regions (i.e., $G - G_{RP}$ in the range 0.2–0.8), both of these isochrones fall below the NYMG distribution for redder colors ($G - G_{RP} > 0.8$). This general behavior, in which theoretical isochrones fall under the single-star loci of NYMGs in Gaia-based CMDs, has been well documented in the recent literature (e.g., [74]). Nonetheless, it is apparent that the 5 Myr isochrone appears to be the best overall match to the SLFR-generated empirical isochrone. We further discuss the implications of the comparison between empirical and theoretical isochrones for the age of the ϵCA in § 2.5.3.

The SLFR polynomial fitting exercise yields five photometric binary candidates among the 30 *bona fide* M+13 ϵCA members plotted in Figure 2.1. Of note, the majority of these binary star candidates have high RUWE. This is consistent with the results of Belokurov et al. (2020) [92], who found that stars along the binary-star locus within all Gaia data show higher RUWEs than stars along the single-star locus. This correlation is likely a result of marginally resolved, close binaries yielding low-precision astrometric solutions. The SLFR method also flagged two clear CMD outliers among the 32 *bona fide* members, T Cha and 2MASS J12014343-7835472, both of which are discussed in Sec 2.4.1.3.

2.3.2 Kinematic Analysis

We calculated the heliocentric space motions and positions of the (35) stars considered as ϵCA members by M+13 (Section 2.2) for which proper motions, parallaxes, and radial velocities (RVs) are available (see Table 2.1). Gaia DR2 provides RVs for 8 stars, and the remaining (majority) of the RVs come from M+13 and other RV surveys in the literature (see footnote b of Table 2.1). Heliocentric velocities (UVW) and positions (XYZ) were calculated using code from BANYAN Σ [93]. In cases where a star had multiple RV measurements, we adopt the mean RV to calculate UVW, except in the case of T Cha (see Section 2.4.1.3). The resulting UVW were used to reevaluate ϵCA membership (§ 2.4.1).

2.4 Results

2.4.1 Membership

2.4.1.1 Kinematic and photometric inclusion/rejection parameters and criteria

We employed two quantitative criteria, kinematic offset (K_{kin}) and magnitude offset (ΔM), to help assess ϵCA membership. These two metrics, listed in Table 2.3, correspond to those defined in M+13. Specifically, the kinematic offset is defined as

$$K_{kin} = \sqrt{(U-U_0)^2 + (V-V_0)^2 + (W-W_0)^2} \tag{2.4.1}$$

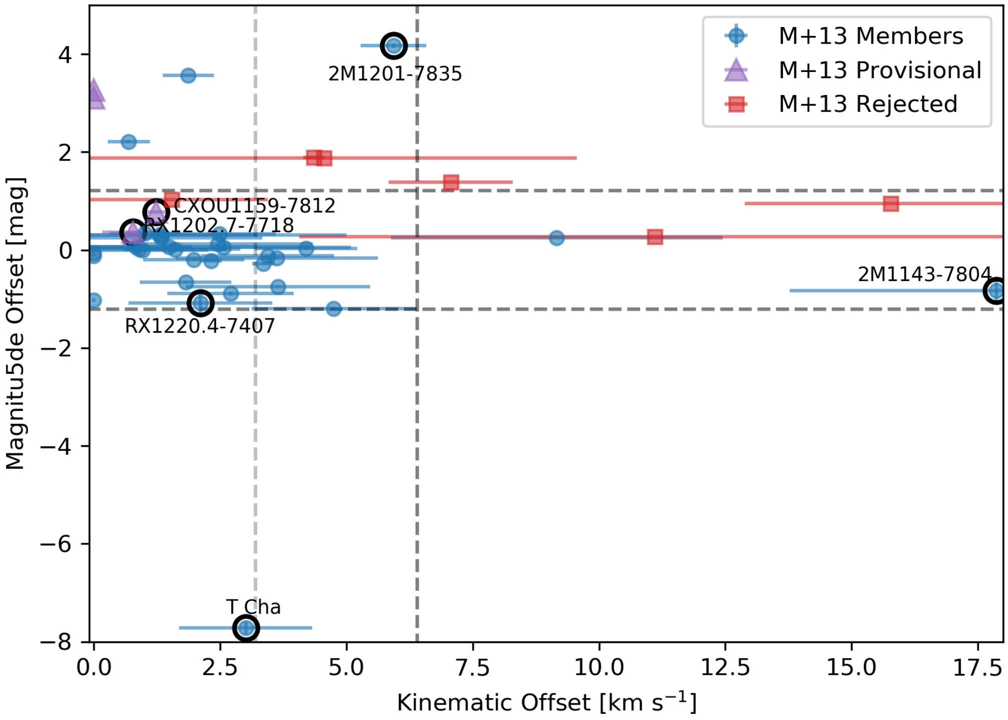

Figure 2.2: Comparison of the offsets in CMD (G vs. $G - R_p$) space and kinematic (UVW) space used to assess ϵCA membership (Section 2.4.1). Blue circles, purple triangles, and red squares represent the M+13 ϵCA study's *bona fide* members, provisional members, and rejected stars, respectively. The horizontal dashed lines correspond to $2\sigma_{\Delta M} = 1.25$ mag; the vertical dashed lines correspond to $\sigma_{K_{kin}}$ (3.2 km s^{-1}) and $2\sigma_{K_{kin}}$. Points appearing at 0.0 on the x-axis are stars lacking radial velocities measurements, for which kinematic offsets cannot be determined. Four outliers discussed in the text are labeled: RX J1220.4-7407 and 2MASS J11432669-7804454 in Section 2.4.1.2, T Cha and 2MASS J12014343-7835472 in Section 2.4.1.3, and RX J1202.8-7718 and CXOU J1159082-781232 in Section 2.4.1.4.

where (U_0,V_0,W_0) is the mean space motion for ϵCA as calculated from the 30 *bona fide* M+13 members used for the SLFR analysis (§2.3.1). We defined ΔM as:

$$\Delta M = M'(c) - M \tag{2.4.2}$$

where c is the color of the star, $M'(c)$ is the absolute magnitude of the empirical isochrone at the star's color, and M is the measured absolute G magnitude of the star. Outliers in ΔM are those with $|\Delta M| \geq 2\sigma_{\Delta M}$ and in K_{kin} are $K_{kin} \geq 2\sigma_{K_{kin}}$, where $\sigma_{\Delta M} = 0.629$ mag and $\sigma_{K_{kin}} = 3.2$ km s^{-1}. These standard deviations are calculated for the M+13 *bona fide* membership list with usable data (30 stars), i.e., omitting M+13's (17) provisional and rejected members.

Figure 2.2, like Figure 8 in M+13, illustrates the kinematic and magnitude offsets plotted against each other. The figure includes all stars from M+13 (i.e., M+13's *bona fide*, provisional, and rejected members) with Gaia parallaxes and $G-G_{RP}$ colors. Stars with K_{kin} or ΔM values that place them within both 2σ boundaries, within errors, are henceforth considered to be high-probability members of ϵCA. Stars outside these bounds were reconsidered for membership on a case by case basis. For instance, the two magnitude outliers within $1\sigma_K$, HD 104036 and HD 104237A, are both A-stars in the bluest region of the CMD. This region is not well fit by the empirical isochrone so the large ΔM is not enough to disqualify their membership. Additional cases, including stars whose DR2 parallaxes render their ϵCA membership doubtful, are discussed in §4.1.2, §4.1.3.

Figure 2.3 presents Gaia CMDs for the full sample of (M+13) stars initially considered ϵCA members, i.e. for the stars listed in Table 2.1 (left panel), and for the final membership list, which is presented and discussed in §2.4.1.5 (right panel). The empirical isochrone in both panels is that found for the original 30 star dataset (i.e., is the same as the SLFR curve in Figure 2.1). In the following, we describe the reasoning behind retaining or rejecting the $> 2\sigma$ outliers plotted in Fig. 2.2.

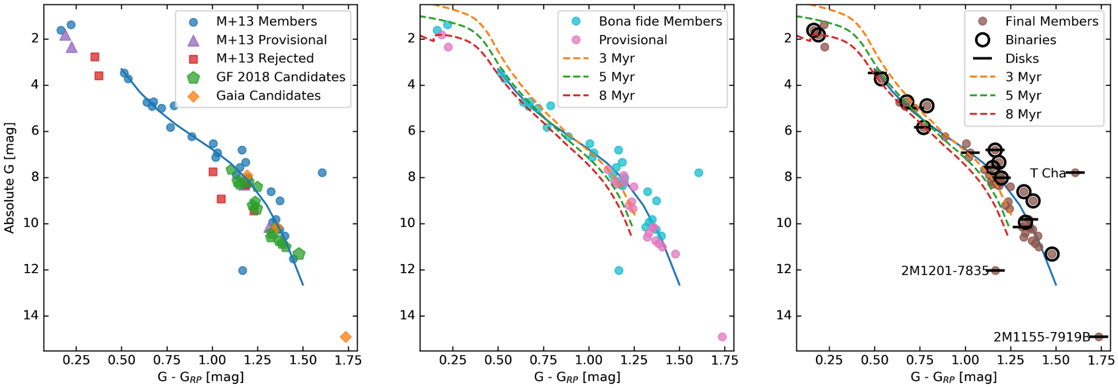

Figure 2.3: Gaia DR2 CMDs for the initial sample of stars considered for ϵCA membership (Table 2.1; left panel) and for our final member lists, both *bona fide* and provisional members (Tables 2.4, 2.5); center and right panels). The empirical isochrone obtained from SLFR analysis of the original 30 *bona fide* members from M+13 (Fig. 2.1) is overlaid in all three panels (blue curves). In the left panel, the blue circles, purple triangles, and red squares indicate M+13 membership candidacy (as in Fig. 2.2); new candidate ϵCA members identified via our wide-separation companion search (Sec 2.4.2.2) are represented by orange diamonds; and candidates originating from GF18 are represented with green pentagons. In the center panel, our final confirmed ϵCA members (Table 2.4 are indicated with brown circles and our provisional ϵCA members (Table 2.5) are indicated with pink circles. This panel and the right panel also include theoretical isochrones (dashed curves) from Tognelli et al. (2018) [5] for ages of 3.0 Myr (orange), 5.0 Myr (green), and 8.0 Myr (red). In the right panel, both provisional and confirmed ϵCA members (Tables 2.4 and 2.5) are represented with brown circles; black dashes indicates stars with disks and black open circles indicate Gaia unresolved binaries and photometric binary candidates. Three stars of particular interest, discussed in the text, are labeled: T Cha (Sec 2.4.1.3), 2MASS J12014343-7835472 (Sec 2.4.1.3), and 2MASS J11550336-7919147 (Sec 2.4.2.2).

2.4.1.2 Candidates rejected on the basis of kinematics, photometry, and/or parallaxes

We corroborate the rejected status of all of the eleven ϵCA members rejected by M+13. Five of the M+13 rejects clearly maintain their non-member status on the basis of the large Gaia-based kinematic and magnitude offsets determined here (Table 2.3). One rejected M+13 member with offsets $< 2\sigma$, 2MASS J12074597-7816064, is unlikely to be a member given its position in the Gaia CMD (Fig. 2.1). This star falls below our empirical isochrone, despite being a suspected spectroscopic binary (M+13). Its kinematic offset is also at the edge of acceptability (K_{kin} = 3.03 km s^{-1}). We hence exclude 2MASS J12074597-7816064 from our final ϵCA membership list. Another five M+13 rejected stars now convincingly lose membership status based on Gaia parallaxes (2MASS J11334926-7618399, RX J1243.1-7458, RX J1150.4-7704, TYC 9238-612-1, and TYC 9420-676-1). VW Cha, which was previously rejected on the basis of a pre-Gaia distance estimate, was not re-considered in this work because no Gaia parallax was reported in DR2.

Two stars previously considered *bona fide* ϵCA members by M+13, 2MASS J11432669-7804454 and RX J1220.4-7407, have CMD positions consistent with young ages and are marginally consistent with ϵCA membership (in terms of ΔM) given our SLFR analysis, although both were flagged as photometric binaries due to their elevation above the single-star locus. Kinematically, RX J1220.4-7407 lies within the distribution of ϵCA members (K_{kin} = 2.11 km s^{-1}), while 2MASS J11432669-7804454 has a large kinematic offset (17.9 km s^{-1}). However, these stars have Gaia parallaxes of 5.54 and 6.71 mas, respectively, a factor of 1.5-2 smaller than the mean for ϵCA (9.81 mas). Notably, both stars have high RUWE and `astrometric_excess_noise` values, suggesting that their parallax solutions may not be reliable. If their parallaxes are in fact accurate, their relatively large distances would indicate they are younger, background T Tauri stars associated with the Cha star-forming region (see, e.g., [66]). Their positions above the single-star locus would be consistent with their belonging to this (generally younger) Cha cloud population. Given these uncertainties, we do not include these two stars in our final roster of *bona fide* ϵ CA members, although their status is worth

Table 2.3: Membership Quality Flags

Name	K_{kin}	$\sigma_{K_{kin}}$	ΔM	$\sigma_{\Delta M}$	Status	Notes
HD 8279	4.35	0.21	1.8911	0.0066	R	Previously rejected (§ 2.4.1.2)
CP-68 1388	2.0	1.0	-0.1975	0.0097	M	
2MJ11183572-7935548A	4.7	1.6	-1.200	0.033	M	
RX J1123.2-7924	15.8	2.9	0.9509	0.0065	R	Previously rejected (§ 2.4.1.2)
HIP 55746	7.1	1.2	1.383	0.027	R	Previously rejected (§ 2.4.1.2)
RX J1137.4-7648	4.6	5.0	1.8790	0.0046	R	Previously rejected (§ 2.4.1.2)
2MJ11404967-7459394	4.2	1.0	0.025	0.016	M	
2MJ11411722-7315369	–	–	1.093	0.012	P	
2MJ11432669-7804454	17.9	4.1	-0.83	0.24	R	Probable Cha Cloud (§ 2.4.1.2)
2MJ11432968-7418377	–	–	0.8659	0.0090	P	
RX J1147.7-7842	1.81	0.90	-0.6586	0.0097	M	
RX J1149.8-7850	1.0	1.3	-0.0002	0.0097	M	
RX J1150.9-7411	2.7	1.3	-0.892	0.042	M	
2MJ11550485-7919108	–	–	-0.059	0.015	M	
T Cha	3.0	1.3	-7.72	0.13	M	Anomalous CMD position (§ 2.4.1.3)
RX J1158.5-7754B	1.3	2.0	0.2454	0.0105	M	
RX J1158.5-7754A	3.6	1.8	-0.7542	0.0091	M	
HD 104036	1.87	0.51	3.5594	0.0092	M	
CXOU J115908.2-781232	1.22	0.25	0.774	0.015	M	
RX J1159.7-7601	1.3	3.7	0.3029	0.0073	M	
2MJ12000269-7444068	–	–	0.799	0.012	P	
HD 104237A	0.69	0.42	2.21	0.016	M	
HD 104237D	–	–	-0.115	0.015	M	
HD 104237E	–	–	-1.027	0.036	M	
2MJ12005517-7820296	3.4	1.3	-0.125	0.020	M	
HD 104467	1.6	1.0	0.010	0.038	M	
2MJ12014343-7835472	5.93	0.65	4.168	0.045	M	Anomalous CMD position (§ 2.4.1.3)
USNO-B 120144.7-781926	0.83	1.11	0.064	0.022	M	
CXOU J120152.8-781840	2.5	1.1	0.33	0.0163	M	
RX J1202.1-7853	3.35	0.23	-0.279	0.013	M	
RX J1202.8-7718	0.77	0.61	0.365	0.010	M	
RX J1204.6-7731	3.6	2.0	-0.1695	0.0091	M	
HD 105234	–	–	3.1047	0.0083	P	
2MJ12074597-7816064	1.5	1.9	1.029	0.014	R	Previously rejected (§ 2.4.1.2)
RX J1207.7-7953	1.01	0.70	0.3388	0.0087	M	
HIP 59243	–	–	3.2697	0.0075	P	
HD 105923	0.9	2.0	0.0231	0.0091	M	
RX J1216.8-7753	1.3	1.9	0.304	0.012	M	
RX J1219.7-7403	9.2	3.3	0.2485	0.0075	M	
RX J1220.4-7407	2.1	1.4	-1.09	0.24	R	Probable Cha Cloud (§ 2.4.1.2)
2MJ12203396-7135188	–	–	-0.216	0.012	P	
2MJ12203619-7353027	–	–	0.4854	0.0086	P	
2MJ12210499-7116493	2.6	2.5	0.0482	0.0080	M	
2MJ12220068-7001041	–	–	0.547	0.011	P	
2MJ12222238-7137040	–	–	0.248	0.014	P	
2MJ12224862-7410203	–	–	-0.822	0.021	P	
2MJ12255824-7551116	–	–	0.784	0.015	P	
2MJ12324805-7654237	–	–	0.08	0.18	P	
2MJ12332483-6848553	–	–	0.613	0.020	P	
2MJ12351540-7043079	–	–	0.473	0.014	P	
RX J1239.4-7502	1.5	2.8	0.0672	0.0077	M	
2MJ12421315-6943484	–	–	0.235	0.019	P	
RX J1243.1-7458	11.1	7.0	0.27	0.11	R	Previously rejected (§ 2.4.1.2)
2MJ12425584-7034207	–	–	0.270	0.018	P	
2MJ12473611-7031135	–	–	0.5594	0.0073	P	
CD-69 1055	2.5	1.9	0.1176	0.0087	M	
MP Mus	2.32	0.21	-0.2265	0.0097	M	

NOTE: Key for status column: M = member; P = provisional member; R = rejected.

revisiting in future Gaia data releases.

Of the six provisional members identified by M+13, two can be rejected outright based on their Gaia parallaxes: TYC 9414-191-1 ($\pi = 1.56$ mas) and CM Cha ($\pi = 5.15$ mas). TYC 9414-191-1 is likely a background star with proper motions similar to those of ϵCA members, and CM Cha (like 2MASS J11432669-7804454 and RX J1220.4-7407) appears to belong to the more distant Cha cloud T Tauri star population. The other four M+13 provisional members are discussed in Section 2.4.1.4.

2.4.1.3 Outliers retained as likely members

T Cha: T Cha was previously established as a kinematic member of ϵCA [32]. The kinematic analysis of T Cha is more complicated than other ϵCA members, however, due to its variable RV; measurements range from ∼6 to ∼30 km s^{-1} [87]. We adopt the RV measured by Guenther et al. (2007) [83], 14.0±1.3, which is near the median of the values reported by Schisano et al. (2009) [87]; with this RV, the UVW of T Cha (presented in § 2.4.1.5) yield a K_{kin} of 3.0 ± 1.3 km s^{-1}, well within the 2σ region. Adopting a larger value for its RV (e.g., the Gaia DR2 RV, 25.52±4.24) would make T Cha a kinematic outlier. However, its XYZ (52.7, -90.1, -31.4 pc) positions T Cha near the median of ϵCA. We conclude that the Gaia DR2 astrometric data for T Cha support its membership in ϵCA, although the variable nature of its RV still remains to be characterized (see discussion insee discussion in [87]).

The Gaia DR2 photometric data for T Cha (Fig. 2.1) show it to be far redder and fainter than expected for an ϵCA star of its spectral type and mass (G8 and 1.3 $M_{\odot}$, respectively; [87]). In DR2, T Cha was flagged as having a suspect `phot_bp_rp_excess_factor` factor (i.e., $E = 2.2$), indicative of poor-quality photometry. This is perhaps due to the star's notable variable behavior: T Cha is known to exhibit variable extinction in the optical regime, as a consequence of its highly inclined, dusty disk ($i = 73°$; [13]). Schisano et al. (2009) [87] found that T Cha shows a visual extinction (corrected for ISM extinction) of ∼0.5 magnitudes on average, but with large excursions, sometimes reaching a maximum of ∼3 magnitudes. Variable extinction in young stars with disks, such as that displayed by T Cha, has been

Table 2.4: Final ϵ Cha Association Membership List[a]

Name	SpT	Distance [pc][b]	G_{BP}	G	G_{RP}	J	H	K	M[c]	Disk?[d]
CP-68 1388	K1	$115.66^{+0.39}_{-0.38}$	10.568	10.023	9.347	8.48	8.01	7.79	–	–
2MJ11183572-7935548A	M4.5	$94.14^{+1.34}_{-1.30}$	15.513	13.869	12.50	10.50	9.89	9.62	P	–
2MJ11183572-7935548B*	–	$93.04^{+3.61}_{-3.35}$	–	16.189	–	–	–	–	–	–
2MJ11404967-7459394	M5.5	$95.68^{+0.64}_{-0.64}$	18.833	16.429	14.983	12.68	12.15	11.77	–	–
RXJ1147.7-7842	M3.5	$100.52^{+0.39}_{-0.39}$	13.814	12.352	11.168	9.52	8.86	8.59	P	–
RXJ1149.8-7850	M0	$100.28^{+0.25}_{-0.25}$	13.0419	11.932	10.904	9.45	8.72	8.49	–	Y
RXJ1150.9-7411	M3.7	$93.61^{+1.62}_{-1.56}$	14.852	13.457	12.133	10.38	9.78	9.48	VP	–
2MJ11550485-7919108	M3	$100.60^{+0.60}_{-0.59}$	16.826	14.818	13.468	11.22	10.47	10.08	C	Y
T Cha	G8	$108.98^{+0.99}_{-0.97}$	13.682	12.974	11.368	8.96	7.86	6.95	–	Y
RXJ1158.5-7754B	M3	$102.92^{+0.37}_{-0.37}$	14.629	13.202	12.031	10.34	9.72	9.44	–	–
RXJ1158.5-7754A	K4	$104.47^{+0.39}_{-0.38}$	10.688	9.980	9.191	8.22	7.56	7.40	VP	–
HD104036	A7	$103.95^{+0.42}_{-0.41}$	6.806	6.693	6.528	6.29	6.22	6.11	V	–
CXOUJ115908.2-781232*	M4.75	$105.50^{+0.69}_{-0.68}$	17.118	15.256	13.942	12.01	11.45	11.17	–	Y
ϵ Cha AaAbB	B9	111H	4.862	4.782	4.931	5.02	5.04	4.98	V	–
RXJ1159.7-7601	K4	$99.21^{+0.23}_{-0.23}$	11.491	10.809	10.040	9.14	8.47	8.30	–	–
HD 104237C	M/L	–	–	–	–	–	–	–	–	–
HD 104237B	K/M	–	–	–	–	–	–	–	–	–
HD 104237A	A7.75	$107.76^{+0.68}_{-0.67}$	6.710	6.543	6.321	5.81	5.25	4.59	–	Y
HD 104237D	M3.5	$100.61^{+0.62}_{-0.62}$	14.440	13.021	11.823	9.62	8.74	8.12	–	?
HD 104237E	K5.5	$101.52^{+0.35}_{-0.34}$	12.653	11.838	10.675	$\geq$9.10	$\geq$8.25	7.49	P	Y
2M J12005517-7820296	M5.75	$102.39^{+0.87}_{-0.85}$	17.865	15.583	14.182	11.96	11.40	11.01	S	Y
HD 104467	G3	$98.11^{+1.62}_{-1.56}$	8.796	8.428	7.914	7.26	6.97	6.85	C	–
2MJ12014343-7835472	M2.25	$104.334^{+1.16}_{-1.13}$	18.205	17.115	15.949	14.36	13.38	12.81	–	Y
USNO-B 120144.7-781926	M5	$101.29^{+0.65}_{-0.64}$	17.248	15.276	13.904	11.68	11.12	10.78	–	Y
CXOUJ120152.8-781840	M4.75	$102.16^{+0.71}_{-0.70}$	16.939	14.982	13.650	11.63	11.04	10.77	–	–
RXJ1202.1-7853	M0	$99.36^{+0.46}_{-0.45}$	12.547	11.510	10.504	9.215	8.46	8.31	V	–
RXJ1202.8-7718*	M3.5	$103.52^{+0.37}_{-0.37}$	14.795	13.375	12.199	10.51	9.83	9.59	–	–
RXJ1204.6-7731	M3	$100.24^{+0.34}_{-0.33}$	13.94	12.571	11.420	9.77	9.13	8.88	–	–
RXJ1207.7-7953	M3.5	$99.30^{+0.30}_{-0.30}$	14.793	13.340	12.154	10.43	9.76	9.57	–	–
HD 105923	G8	$105.78^{+0.41}_{-0.40}$	9.245	8.837	8.300	7.67	7.31	7.18	VC	–
RXJ1216.8-7753	M4	$101.27^{+0.40}_{-0.40}$	14.236	12.921	11.789	10.09	9.47	9.24	–	–
RXJ1219.7-7403	M0	$100.82^{+0.27}_{-0.27}$	13.201	12.140	11.121	9.75	9.05	8.86	–	–
2MJ12210499-7116493	K7	$98.92^{+0.24}_{-0.23}$	12.044	11.203	10.316	9.09	8.42	8.24	–	–
RXJ1239.4-7502	K3	$103.10^{+0.29}_{-0.28}$	10.531	9.975	9.307	8.43	7.95	7.78	–	–
CD-69 1055	K0	$94.32^{+0.26}_{-0.26}$	10.132	9.606	8.967	8.18	7.70	7.55	–	–
MP Mus	K1	$98.34^{+0.30}_{-0.30}$	10.547	9.952	9.231	8.28	7.64	7.29	–	Y

NOTE: a) * = previously not considered a *bona fide* member (M+13).

b) Distances have been calculated using the inverse parallax method with zero-point corrections [90].

c) Multiplicty Key: S = suspected spectroscopic binary (M+13); V = resolved binary [94]; P = possible photometric binary (this work); C = potential wide separation companion (this work).

d) IR excess and/or other evidence indicative of presence of circumstellar disk (M+13 and references therein).

Table 2.5: Provisional ϵ Cha Association Membership List

Name	SpT^{a}	Distance [pc]^{b}	G$_{BP}$	G	G$_{RP}$	J	H	K	M^{c}	Disk?^{d}
2MJ11411722-7315369	M4.5	$95.51^{+0.47}_{-0.47}$	17.382	15.478	14.155	12.16	11.56	11.31	–	–
2MJ11432968-7418377	M3.5	$98.84^{+0.38}_{-0.38}$	15.742	14.176	12.955	11.25	10.60	10.37	–	–
2MJ11550336-7919147	M6	$101.26^{+5.70}_{-5.12}$	20.476	19.925	18.189	15.85	15.03	≥12.64	–	Y
2MJ12000269-7444068	M4	$98.80^{-0.48}_{+0.48}$	15.959	14.324	13.081	11.37	10.67	10.42	–	–
2MJ12011981-7859057	M5	$101.55^{+0.78}_{-0.77}$	17.251	15.179	13.823	11.75	11.20	10.89	–	–
HD 105234	A9‡	$103.96^{+0.38}_{-0.37}$	7.570	7.419	7.195	6.87	6.76	6.68	V	Y
HIP 59243	A6‡	$99.27^{+0.32}_{-0.32}$	6.934	6.794	6.605	6.35	6.23	6.17	V	–
2MJ12115619-7108143	M3	$105.28^{+0.76}_{-0.75}$	14.530	13.021	11.828	10.09	9.51	9.24	–	–
2MJ12203396-7135188	M4	$92.36^{+0.49}_{-0.48}$	14.880	13.219	11.971	10.14	9.57	9.27	–	–
2MJ12203619-7353027	M2.5	$99.40^{+0.35}_{-0.34}$	14.485	13.141	11.998	10.41	9.71	9.48	–	–
2MJ12220068-7001041	M4	$99.39^{+0.47}_{-0.47}$	15.402	14.024	12.787	≥10.40	≥10.00	≥9.90	–	–
2MJ12222238-7137040	M2	$94.61^{+0.25}_{-0.24}$	13.769	12.530	11.425	9.90	9.27	8.99	–	–
2MJ12224862-7410203	M5.5	$93.82^{+0.79}_{-0.78}$	18.688	16.175	14.698	12.26	11.69	11.29	P	–
2MJ12255824-7551116	M4.5	$98.98^{+0.64}_{-0.63}$	17.324	15.366	14.034	12.02	11.49	11.19	–	–
2MJ12324805-7654237	M3	$85.17^{+7.14}_{-6.11}$	14.310	12.835	11.639	9.88	9.26	8.96	–	–
2MJ12332483-6848553	M5	$98.86^{+0.85}_{-0.83}$	17.829	15.712	14.344	12.28	11.68	11.37	–	–
2MJ12351540-7043079	M5	$92.94^{+0.57}_{-0.56}$	17.853	15.701	14.317	12.18	11.66	11.33	–	–
2MJ12421315-6943484	M5	$98.85^{+0.82}_{-0.80}$	17.167	15.144	13.789	11.76	11.15	10.87	–	–
2MJ12425584-7034207	M5	$98.86^{+0.77}_{-0.75}$	18.261	15.975	14.570	12.32	11.79	11.46	–	–
2MJ12473611-7031135	M3	$99.35^{+0.31}_{-0.30}$	14.628	13.269	12.119	10.50	9.86	9.71	–	–

NOTE: a) Spectral types determined

b) Distances have been calculated using the inverse parallax method with zero-point corrections [90].

c) S = suspected spectroscopic binary (M+13); V = resolved binary [94]; P = possible photometric binary (this work); C = potential wide separation companion (this work).

d) IR excess and/or other evidence indicative of presence of circumstellar disk (M+13 and references therein)..

hypothesized to result from a nested inner/outer disk structure wherein a warped inner disk causes quasi-periodic occultations of the photosphere [95]. Modeling of the disk around T Cha shows that instead its variability could be caused by an asymmetric, puffed-up inner disk rim [96].

Based on its position in the Gaia CMD (Fig. 2.3, right) and assuming a spectral type of G8 [87] — which suggests an absolute G magnitude of 3.3, given the SLFR-derived empirical isochrone (Fig 2.1) — and applying a standard ISM reddening law [97], we infer an A_V of 6.0 magnitudes at the time of Gaia observations. This A_V is a factor ∼10 larger than the typical A_V reported by Schisano et al. (2009) [87] — a surprising result, given that (as of DR2) Gaia data included 9 viable visibility periods. Alternatively, if we were to accept the $G - G_{RP}$ of T Cha at face value, then the star displays a color excess $E(G - G_{RP}) = 1.11$, which would imply $A_V \sim 3.5$ assuming T Cha's obscuration follows the same [97] standard reddening law. This is still a factor ∼5 larger than typical for T Cha, and is furthermore discrepant with A_V as determined from its spectral-type-based absolute magnitude. Thus, while T Cha's anomalous position in the ϵCA CMD is likely due in part to obscuration by its disk, and suggests the disk dust exhibits non-ISM-like reddening, we caution that its position (low and red) in the CMD may also be a consequence of suspect Gaia photometry.

2MASS J12014343-7835472: This early-M star (M2.25; [98]), also known as ϵCA 11, is notably underluminous for a star in this spectral type regime ($\Delta M \sim 4$ mag; Fig. 2.1). Previous studies of ϵCA have proposed that 2MASS J12014343-7835472 is orbited by a nearly edge-on disk [98], such that the cold, outer parts of the disk flare to block the stellar photospheric emission, which is then only detected in the form of scattering off the inner disk [99]. The star also appears to be actively accreting disk material, given its large Hα equivalent width [98].

Although 2MASS J12014343-7835472 has a large K_{kin} value (5.7 km s^{-1}), this is mainly due to its low measured RV (11.44±2.53 km s^{-1}); its Gaia DR2 proper motions are generally consistent with those of other ϵCA members. Furthermore, its lithium absorption line (λ6708) equivalent width is consistent with the young age of the ϵCA (M+13). Its membership in ϵCA is hence supported by the available data, provided its photospheric emission is indeed strongly attenuated by a nearly edge-on disk. Unlike T Cha, the $G - G_{R_P}$ color of 2MASS J12014343-7835472 appears consistent with its spectral type (Fig. 2.1), suggesting that the occulting disk dust has a significant component of large grains even as the Gaia photometry is dominated by starlight scattered off the disk surface.

2.4.1.4 Other epsCA Candidates

Provisional M+13 candidates: Two stars designated as provisional ϵCA members in the M+13 ϵCA study, RX J1202.8-7718 and CXOU J115908.2-781232, are upgraded here to *bona fide* members. RX J1202.8-7718 was identified as a kinematic member in M+13 but its status was uncertain, with the possibility remaining that it could belong to the Lower Centaurus Crux (LCC) subgroup of the Scorpius-Centaurus OB association. In our analysis, RX J1202.8-7718 has both low K_{kin} (0.31 km s^{-1}) and ΔM (0.39 mags), suggesting that it is unlikely to be an interloper from the LCC. Likewise, on the basis of its pre-Gaia proper motion and distance, M+13 suspected that CXOU J115908.2-781232 may be associated with the Cha I cloud. However, Gaia DR2 places the star at ~ 105 pc, consistent with ϵCA and much nearer to Earth than Cha I. Given its low K_{kin} (0.31 km s^{-1}) and ΔM (0.82 mag), we include CXOU J115908.2-781232 among our *bona fide* ϵCA member list.

Two other M+13 provisional members, HD 105234 and HIP 59243, lack the requisite RVs to determine their UVW and, hence, kinematic offsets, and are thus also classed as provisional members in our final membership list. Therefore, of the six provisional members presented by M+13, two are rejected, two are upgraded to *bona fide*, and two maintain their provisional status.

Gagné and Faherty (2018) [2] candidates: On the basis of a statistical analysis of Gaia DR2 data (utilizing BANYAN; [93]), GF18 identified a total of 15 stars that are candidate members of ϵCA. These stars were designated as high-probability members (5 stars), possible members (5), and low-probability members (5), based on BANYAN probabilities of membership in ϵCA as well as in other young moving groups. Their XZ distribution (Figure 2.4, left panel) makes apparent that the GF18 high-probability members are found within the spatial locus of stars

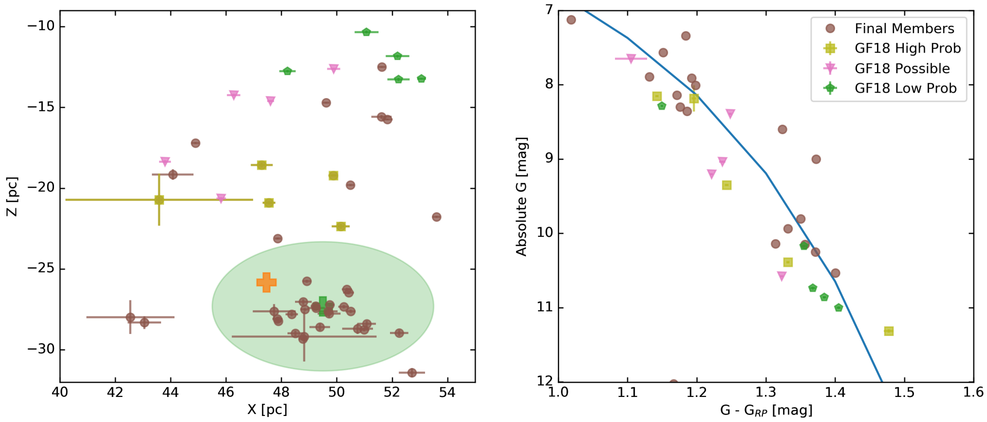

Figure 2.4: Individual components of heliocentric positions (XZ) and the Gaia CMD for both the final membership list of ϵCA (Table 2.4; brown circles) and GF18 ϵCA candidates. Yellow squares, pink triangles, and green pentagons indicate GF18's high probability, possible, and low probability members, respectively. In the left panel, the heliocentric median and mean positions for ϵCA members (Table 2.8) are indicated as green and orange plus signs, respectively. The green shaded region represents the area within the inferred tidal radius (∼4 pc; Section 2.5.2) as centered on the median position.

we designate as *bona fide* ϵCA members — albeit outside the core ϵCA group (centered at $X \sim 49$ pc, $Z \sim -28$ pc), since the GF18 study excluded stars with distances >100 pc — whereas the lower-probability members are found at the upper XZ periphery of the group.

In contrast, there is no such clear distinction between the CMD positions of the three categories of GF18 candidates. All 15 stars lie along the single-star CMD locus of ϵCA determined via our SLFR analysis, although most (13 of 15) lie below the empirical isochrone, by up to a magnitude (Figure 2.4, right panel). While this might cast doubt on their ϵCA membership, we caution that most of the GF18 stars lie in a region of CMD space that is poorly sampled by kinematically verified ϵCA members. Hence, the final membership status of all 15 stars is not easily assessed, and must await measurements of, e.g., RVs and Li absorption line strengths.

To assign spectral types to the provisional ϵCA members gleaned from the GF18 study, as well as other provisional members (§2.4.1.5), we have determined an empirical relationship between spectral subtype and Gaia color for *bona-fide* K- and M-type ϵCA members. For this purpose, we selected those K and M stars from our final membership list (§2.4.1.5) for

Table 2.6: New Wide Separation Companions to ϵCA Members^a

Name	SpT	RA (deg)	Dec (deg)	π (mas)	G (mag)	G−G_{RP} (mag)	PMRA (mas/yr)	PMDec (mas/yr)
2MJ11550485-7919108	M3	178.7692	-79.3198	9.886±0.058	14.818	1.35	-41.18±0.13	-4.34±0.09
2MJ11550336-7919147	M6	178.7628	-79.3208	9.82±0.53	19.92	1.74	-39.74±1.22	-4.66±0.68
HD 104467	G3	180.4120	-78.9881	10.14±0.17	8.428	0.515	-41.11±0.26	-5.41±0.26
2MJ12011981-7859057	M5	180.3316	-78.9849	9.794±0.075	15.179	1.3562	-41.99±0.12	-5.35±0.10
HD 105923	G8	182.9084	-71.1767	9.400±0.036	8.837	0.537	-38.720±0.060	-7.42±0.05
2MJ12115619-7108143	M3	182.9836	-71.1374	9.44±0.68	13.021	1.1928	-38.64±0.11	-8.11±0.09

NOTE: a) Candidate wide-separation comoving systems are listed as pairs, with the previously identified ϵCA member listed first and its candidate wide-separation companion listed second.

which spectral types were determined from optical spectroscopy, and for which $E(B-V) \leq 0.05$, based on data presented in M+13. The resulting empirical relationship is illustrated in Figure 2.5. The best-fit second-order polynomial shown in the Figure is given by

$$Sp(c) = -12.78c^2 + 42.54c - 29.26, \tag{2.4.3}$$

where Sp is the spectral index of the star, defined such that (...−1, 0, +1, ...) = (...K7, M0, M1, ...), and c is $G - G_{RP}$ color. Figure 2.5 demonstrates that Eq. 2.4.3 provides an accuracy of roughly a subtype for K and M stars in the ϵCA. The spectral types determined from this empirical color-subtype relationship for the provisional members from GF18 are, in most cases, 0.5-2.0 subtype later than those reported by GF18. Our determinations are likely to be more reliable, however, given that they are based on the Gaia colors of *bona fide* ϵCA members of known spectral type, and the color-subtype relationship is known to be age-dependent (e.g., [100]).

2.4.1.5 Final epsCA Membership; Provisional Members

Our final ϵCA membership list, including spectral types, distances, Gaia photometry, and 2MASS photometry [10], is presented in Table 2.4. Most ϵCA candidates without RVs are here designated as provisional members — the exceptions being three systems lacking RVs that were classified as *bona fide* members by M+13, for which we find Gaia DR2-based XYZ and CMD positions that are consistent with membership. The provisional members are presented in Table 2.5. The latter list includes three new members revealed via a search for wide-separation companions (Table 2.6; see Section 2.4.2.2).

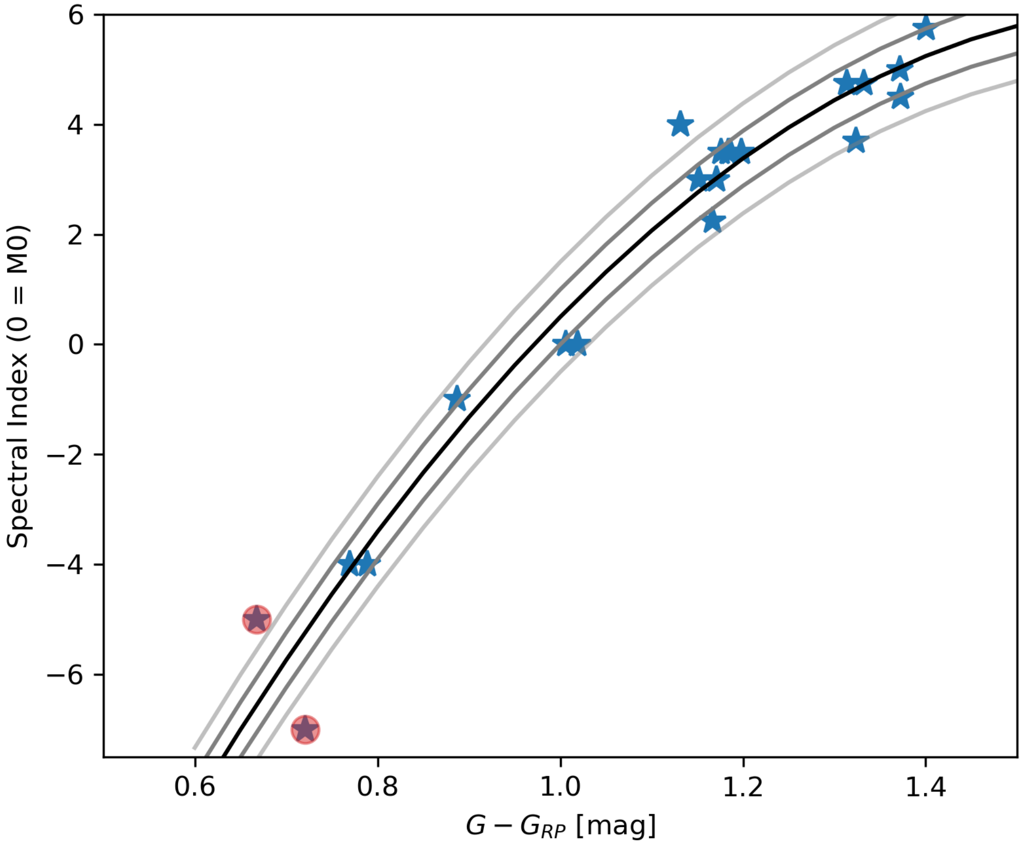

Figure 2.5: Spectral index vs. Gaia $G - G_{RP}$ color for all M+13 members with $E(B-V) \leq 0.05$. Spectral index is here defined such that (...−1, 0, +1, ...) = (...K7, M0, M1, ...). Most stars have inferred $E(B-V) = 0.0$; two stars with $E(B-V) = 0.05$ are marked with red circles. The black curve represents the best-fit 2nd-order polynomial, and the dark and light grey curves represent deviations of 0.5 and 1.0 subtype, respectively.

For each star in Tables 2.4 and 2.5, we also indicate stellar multiplicity and presence/absence of evidence of a circumstellar disk. Multiplicity is further subdivided into photometric binaries (P), visual binaries from Briceño et al. (2017) [94] (V), suspected spectroscopic binaries from M+13 (S), and candidate wide separation companion systems (C). Binarity and multiplicity within the final membership list is further discussed in Section 2.4.2.

Table 2.7 lists the heliocentric space positions (XYZ) and velocities (UVW) of the final ϵCA membership. The medians and (uncertainty-weighted) means of these spatial and kinematic coordinates, as calculated from the positions and velocities of *bona fide* members in Table 2.4, are tabulated in Table 2.8.

Figure 2.6 illustrates the individual and mean positions and velocities. Based on our final membership, the mean distance to the ϵCA is 100.99 pc, with a standard deviation $\sigma = 4.62$ pc. The structure and spectral type distribution of the association are discussed in Section 2.5.2.

2.4.2 Multiplicity

2.4.2.1 Photometric Binaries

On the basis of our SLFR analysis, we identify five photometric binary candidates, i.e., stars that lie above the single-star locus at positions consistent with their being double or perhaps triple systems: RX J1150.9-7411, RX J1158.5-775A, HD 104237E, RX J1147.7-7842, and 2MASS J11183572-7935548. These stars have ΔM values of -1.211, -0.670, -0.903, -0.767, and -1.038, respectively. Two of these systems, RX J1150.9-7411 and RX J1158.5-775A, have been resolved visually (separations $0.875''$ and $0.073''$, respectively; [101, 94]) but evidently even the former is unresolved in Gaia DR2.

HD 104237E is already known to have a companion, HD 104237D (at separation $4.24''$; [94]), and would be a hierarchical triple system if HD 104237E is confirmed as a binary (see §2.4.2.3). The DR2-based binary candidacy of RX J1147.7-7842 is also novel. Both systems warrant spectroscopic followup to search for RV variability, since close binaries can have suspect Gaia DR2 astrometry (e.g., [102]). We note that Briceño et al. (2017) [94] failed to detect companions at separations as small as $\sim 0.1''$ ($\sim$10 au) for these two stars.

Table 2.7: Bona Fide ϵCA Members: Heliocentric Positions and Velocities

Name	X	σ	Y	σ (pc)	Z	σ	U	σ	V	σ (km/s)	W	σ
CP-68 1388	44.89	0.15	-105.20	0.35	-17.209	0.057	-10.86	0.39	-20.69	0.91	-8.72	0.15
2MJ11183572-7935548A	43.049	0.605	-78.8	1.1	-28.32	0.40	-7.80	0.77	-23.6	1.3	-10.37	0.50
2MJ11183572-7935548B	42.5	1.6	-77.9	2.9	-28.0	1.0	–	–	–	–	–	–
RX J1147.7-7842	47.86	0.19	-83.82	0.33	-28.09	0.11	-9.54	0.44	-20.99	0.75	-11.23	0.25
RX J1149.8-7850	47.89	0.12	-83.46	0.21	-28.230	0.071	-10.87	0.62	-18.8	1.1	-10.39	0.37
RX 1150.9-7411	44.08	0.75	-80.3	1.4	-19.16	0.33	-7.88	0.64	-19.3	1.0	-10.57	0.29
2MJ11550485-7919108	48.51	0.29	-83.23	0.49	-28.98	0.17	–	–	–	–	–	–
T Cha	52.712	0.474	-90.06	0.81	-31.43	0.28	-11.98	0.65	-19.4	1.1	-13.03	0.38
RX J1158.5-7754B	49.75	0.18	-85.89	0.31	-27.220	0.098	-10.45	0.97	-18.5	1.7	-10.00	0.53
RX J1158.5-7754A	50.50	0.19	-87.18	0.32	-27.62	0.10	-10.06	0.88	-18.3	1.5	-13.71	0.48
HD 104036	50.25	0.20	-86.80	0.35	-27.34	0.11	-11.49	0.25	-18.26	0.41	-11.07	0.14
CXOU J115908.2-781232	51.08	0.33	-87.83	0.57	-28.40	0.19	-9.45	0.16	-20.27	0.18	-10.398	0.076
RX J1159.7-7601	47.87	0.11	-83.77	0.19	-23.116	0.053	-10.4	1.8	-18.7	3.1	-9.65	0.86
HD 104237A	52.25	0.33	-89.68	0.56	-28.96	0.18	-10.85	0.23	-19.15	0.33	-10.60	0.12
HD 104237D	48.79	0.30	-83.73	0.52	-27.04	0.17	–	–	–	–	–	–
HD 104237E	49.23	0.17	-84.49	0.29	-27.290	0.093	–	–	–	–	–	–
2MJ12005517-7820296	49.72	0.42	-85.09	0.71	-27.76	0.23	-11.92	0.65	-16.9	1.1	-9.01	0.36
HD 104467	47.74	0.77	-81.1	1.3	-27.63	0.45	-10.39	0.55	-18.32	0.81	-9.65	0.30
2MJ12014343-7835472	50.75	0.56	-86.52	0.95	-28.71	0.32	-8.02	0.36	-24.72	0.51	-12.37	0.19
USNO-B 120144.7-781926	49.26	0.32	-84.16	0.54	-27.42	0.18	-10.02	0.55	-20.34	0.92	-10.61	0.30
CXOU J120152.8-781840	49.69	0.34	-84.88	0.59	-27.62	0.19	-9.02	0.55	-21.44	0.92	-11.36	0.30
RX J1202.1-7853	48.37	0.22	-82.22	0.38	-27.80	0.13	-10.18	0.13	-23.05	0.17	-10.661	0.067
RX J1202.8-7718	50.37	0.18	-86.55	0.31	-26.265	0.094	-9.85	0.30	-19.89	0.50	-10.11	0.16
RX J1204.6-7731	48.92	0.17	-83.61	0.28	-25.761	0.087	-11.98	0.98	-16.67	1.67	-9.11	0.52
RX J1207.7-7953	48.77	0.15	-81.38	0.25	-29.325	0.089	-9.88	0.35	-20.29	0.58	-10.92	0.21
HD 105923	51.83	0.20	-90.86	0.35	-15.736	0.060	-9.64	0.52	-20.67	0.91	-8.76	0.16
RX J1216.8-7753	50.43	0.20	-83.74	0.33	-26.46	0.10	-9.7	1.0	-19.5	1.6	-10.39	0.52
RX J1219.7-7403	50.50	0.14	-84.98	0.23	-19.808	0.053	-9.71	0.95	-20.02	1.59	-9.40	0.37
2MJ12210499-7116493	49.61	0.12	-84.31	0.20	-14.713	0.035	-10.5	1.3	-18.16	2.16	-8.38	0.38
RX J1239.4-7502	53.60	0.15	-85.33	0.24	-21.772	0.060	-9.3	1.5	-19.8	2.3	-9.66	0.59
CD-69 1055	51.63	0.14	-77.94	0.22	-12.501	0.034	-9.8	1.0	-18.7	1.6	-8.28	0.25
MP Mus	56.85	0.17	-79.36	0.24	-11.857	0.036	-9.13	0.13	-19.64	0.17	-8.566	0.043

Table 2.8: Mean and Median Heliocentric Positions and Velocities of ϵCA Members

	Mean^a	Median	σ^b
Distance [pc]	100.99	100.81	4.62
X [pc]	49.660	49.650	2.854
Y [pc]	-84.328	-84.232	5.185
Z [pc]	-18.905	-27.378	5.143
U [km s^{-1}]	-9.847	-9.954	1.089
V [km s^{-1}]	-20.667	-19.557	1.788
W [km s^{-1}]	-9.682	-10.382	1.305

NOTE: a) Weighted means and medians as calculated from values listed in Table 2.7.
b) Standard deviation of the corresponding weighted mean.

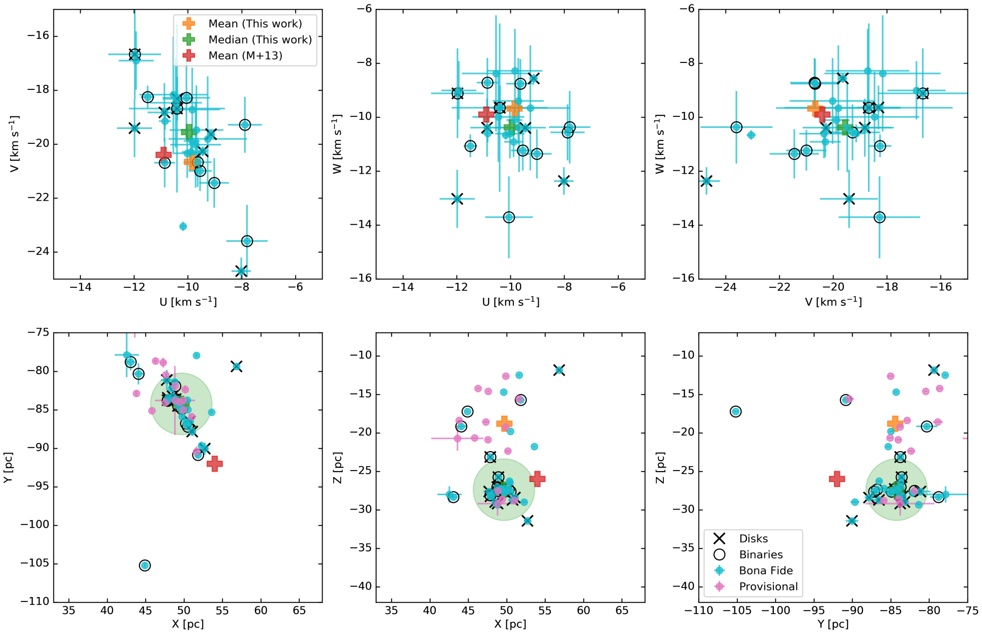

Figure 2.6: Individual components of heliocentric positions (XYZ) and velocities (UVW) plotted against one another for the final membership list (Table 2.4, cyan circles) and the provisional members (Tables 2.5, pink circles), with open black circles marking stars that are unresolved binaries and black x's marking stars with disks. Table 2.4 stars lacking measured RVs (see Table 2.1) are omitted from the UVW plots. The mean and median values of UVW and XYZ are indicated by orange and green crosses, respectively, in each plot; the previously obtained mean values (from M+13) are represented by red crosses. The region within the calculated tidal radius (4 pc, Sec 2.5.2) is indicated as a green circle in the XYZ plots, centered on the median. When no error bar can be seen, the error lies within the marker.

Briceño et al. (2017) [94] found that the 2MASS J11183572-7935548 system (henceforth J1118AB) is a $0.92''$ separation binary consisting of an M4.5 primary and a lower-luminosity companion that may be related to the transition-disk nature of the object. The Gaia DR2 data confirm the angular separation ($0.9''$) and establish that this corresponds to a projected physical separation of 85 au. The parallaxes for J1118AB agree, within the errors, confirming that they constitute a physical pair. Unfortunately, the only Gaia photometry for J1118B is in the G band, so we could not ascertain the CMD location of this companion. J1118A was flagged as a spectroscopic binary in M+13 and, via our SLFR method, we find it is also a candidate photometric binary. In light of the presence of the faint visual companion 2MASS 1118B [94], it appears that 2MASS 1118AB is a possible hierarchical triple system.

2.4.2.2 Wide Separation Binaries

We searched for potential wide separation companions to all ϵCA members retained after applying the criteria described in Section 2.4.1. Specifically, we searched the Gaia DR2 catalog for equidistant, comoving stars by querying the catalog for all Gaia sources within a 500" radius of the position of each of these ϵCA members, and then reordering the resulting source list by parallax. This search radius corresponds to ∼50 kau, or ∼0.25 pc, at the mean distance to ϵCA. While a search of ϵCA member fields within this radius typically returns ∼2000 stars, once ordered by parallax, potential (equidistant) companions to the star originally queried rise to the top of the list and are hence conspicuous. All stars so identified have parallaxes and proper motions within a few percent of the star searched and so were accepted as wide separation companion candidates.

Applying this method, we have identified three new candidate members of ϵCA. Gaia DR2 data for these candidates are listed in Table 2.6. The faintest and reddest of these three, 2MASS J11550336-7919147, is described below. The other two comoving companion candidates, 2MASS J12011981-7859057 and 2MASS J12115619-7108143, are mid-M stars that fall along the empirical single-star isochrone, with $\Delta\mathrm{M} \leq 2\sigma_{\Delta M}$. These two candidate comoving companions have projected physical separations from their primaries of 5.7 kau and 17.7 kau, respectively. We estimated their spectral types (M5 and M3, respectively) from the empirical relationship between Gaia $G - G_{RP}$ color and spectral type for ϵCA members described in § 2.4.1.4. Neither star displays evidence of a dusty disk in the form of an IR excess, i.e., both have 2MASS/WISE colors consistent with those of "diskless" young M stars of similar spectral type [100].

This comoving companion search also recovered multiple stars already considered ϵCA members as components of possible wide binary systems. The RX J1158.5-7754 system was matched with HD 104036. Three stars, 2MASS J12005517-7820296, CXOU J120152.8-781840, and USNO-B 120144.7-781926, were identified as a three-component comoving system. We also identified CXOU J115908.2-781232, a provisional M+13 member, as another possible component of the HD104237 multiple system (see §2.4.2.3).

2MASS J11550336-7919147: The third, newly-identified wide-comoving companion, 2MASS J11550336-7919147 (henceforth 2MASS J1155-7919B), at an absolute G magnitude of ∼15 and $G - G_{RP} \sim 1.75$, is both the faintest and the reddest object thus far identified in ϵCA [65]. As described in Dickson-Vandervelde et al. (2020) [65], we find 2MASS J1155-7919B is comoving with 2MASS 11550485-7919108 (hereafter 2MASS J1155-7919A). The star 2MASS J1155-7919A was itself initially thought to be a wide-separation comoving companion to T Cha [66], before Gaia DR2 data established that T Cha and J1155-7919A are neither equidistant nor precisely comoving [102]. The 2MASS J1155-7919AB pair has a projected separation of 5.75", corresponding to a projected physical separation of 566 AU. In Dickson-Vandervelde et al. (2020) [65], we suggested that the position of 2MASS J1155-7919B at the extreme faint, red end of the single-star locus of the ϵCA CMD reflected its likely status as a substellar object, with a bolometric luminosity ($\log L_{bol}/L_{\odot} = -3.2$) that would imply its mass is a mere ∼10 M_{Jup}. This would make 2MASS J1155-7919B the lowest-mass ϵCA member presently known — even less massive than WISEA J120037.79-784508.3, a recently identified brown dwarf candidate and possible ϵCA member [103][1] However, a potential alternative model to explain the large absolute G magnitude and red color of 2MASS J1155-7919B is that the object is in fact a mid-M star — possibly a near-twin to host 2MASS J1155-7919A — that is obscured by a

---

[1] WISEA J120037.79-784508.3, which has an absolute G magnitude of 11.3, is not included in Table 2.5.

large column density of gray dust in a nearly edge-on disk. Under this interpretation, 2MASS J1155-7919B would be analogous to 2MASS J12014343-7835472 (= ϵCA 11; 2.4.1.3), but even more highly obscured by its disk. Such an alternative explanation is motivated by the fact that 2MASS J1155-7919B is consistently 5 magnitudes dimmer than its host in G, B_p, R_p, J and H (Table 2.6), and that its spectral type, as obtained from its color (via the relationship in Fig. 2.5), is M6. In a forthcoming paper (Dickson-Vandervelde et al., in prep), we further explore these these two possible scenarios for the nature of 2MASS J1155-7919B.

2.4.2.3 HD 104237

HD 104237 is a proposed quintuplet system within ϵCA, consisting of a triple system dominated by the bright Herbig Ae/Be star HD 104237A and including close binary HD 104237DE [76, 82]. Our wide-separation companion search (Sec. 2.4.2.2) also suggests that previously identified ϵCA member CXOU J115908.2-781232 is a possible additional companion to HD 104237A. We also flagged HD 104237E as a possible photometric binary, as noted in § 2.4.2.1. While stellar components A, D, and E were all resolved within Gaia DR2, B and C were not, most likely being incorporated into the Gaia point spread function of HD 104237A.

The majority of stars in the HD 104237 system lie near the spatial median of ϵCA, the densest region of ϵCA, and the system is well within the group's tidal radius (Sec 2.5.2). However, the Gaia DR2 parallaxes of HD 104237D and E place these two stars 6–7 pc closer to Earth than HD 104237A. Indeed, during our wide-separation companion search, HD104237D+E flagged each other, while HD104237A only matched (in terms of parallax and proper motion tolerances) with the star CXOU J115908.2-781232. If HD 104237A+E is in fact a bound system, this would imply that the Gaia DR2 parallaxes for components D and E are spurious. On the other hand, as in the case of T Cha and J1155-7919A, the star originally designated T Cha B [66, 102], it is possible that the apparent D and E components of the HD 104237 system are in fact merely ϵCA members that are seen in projection near the bright primary star. This would not be surprising, given the system's position near the median XYZ of ϵCA. If the potential new components of HD 104237, CXOU J115908.2-781232 and HD104237Eb, are, in fact, bound to HD 104237A, this could be a seven-star system. Alternatively, the bound components may in fact consist of a triple system comprised of HD104237Ea+Eb+D plus a quadruple system comprised of HD104237A+B+C and CXOU J115908.2-781232. Gaia DR3 should help resolve some of this uncertainty concerning the composition of the HD 104237 system, by confirming and/or refining the DR2 parallaxes to its individual components.

2.5 Discussion

2.5.1 Multiplicity Fraction and Spectral Type Distribution

In light of the preceding, we can now revisit the ϵCA multiplicity fraction (MF), or the number of systems consisting of more than one star. Previous to this work, it was found that higher mass stars of ϵCA all have companions, while the lower mass stars have a low companion frequency [94]. The binary fraction, including suspected binaries, was reported in M+13 as 36^{+10}_{-8}%. The MF of our final membership list (Table 2.4) is 40%, with 12 of 30 systems in multiple systems, which is consistent within the errors with the MF determined by M+13.

We further separate the MF of ϵCA into mass groups, bearing in mind small number statistics. For the population of intermediate mass (A and B, n=5), solar-type (F, G, and K, n=11), and low mass (M, n=19) star systems in ϵCA we find MF = 100%, MF = 36%, and MF = 42%, respectively. This can be compared with the MFs of intermediate-mass, solar-type mass, and low mass stars on the main sequence, for which the multiplicity fractions are on average MF $\geq$ 50%, MF = 44 ± 2%, and MF = 26 ± 3%, respectively [104]. In contrast, the MF of T associations lies in the range ~66-75% [104]. The MF of ϵCA is hence less than that of T associations and greater than that of main-sequence stars. This is consistent with the ~5 Myr age of ϵCA (§ 2.5.3), which is intermediate between T associations and the main-sequence field. The ϵCA hence appears to be a key group in which to study the dissolution of young binary systems as T associations evolve toward the field population.

Figure 2.7 presents the spectral type distribution obtained from our final membership list (Table 2.4). For purposes of this histogram, stars whose published spectral types span a range

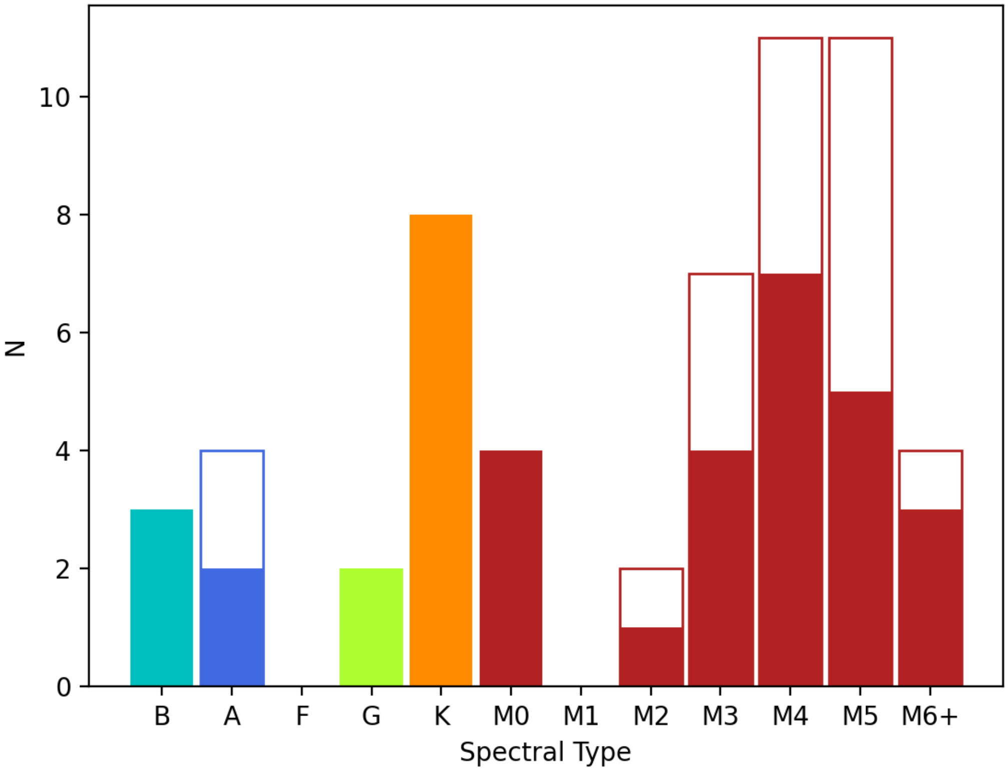

Figure 2.7: Spectral type histogram compiled from the final ϵCA membership lists (Table 2.4, 2.5). Unfilled portions of histogram bars indicate provisional members. Non-M spectral types are grouped across subtypes, while the M subtypes are plotted individually. The color scheme follows that of Figure 9 of Lee et al. (2019) [6].

(e.g., “M3–5”) are assumed to have a spectral type in the middle of that range, and K stars of all subtypes are grouped together. The Figure demonstrates that the ϵCA spectral type distribution, which peaks at M4, resembles that of the χ^1 For cluster (see Figure 6 in [72]) and other nearby associations like TWA, BPMG, and Columba, many of which have far better statistics (see, e.g., Figure 9 in [6]).

2.5.2 Structure of the Association

With accurate heliocentric positions, we can analyze the structure of the ϵCA NYMG in the Galactic context. Following Zuckerman et al. (2019) [72], the tidal radius of the group can be roughly estimated as $r = R(M_c/3M_g)^{1/3}$ [105], where R is the distance between Earth and the Galactic Center ($\sim$ 8200 pc), M_c is the mass of the stellar group, and M_g is the Galactic mass interior to the Sun ($\sim 10^{11}$ $M_\odot$). In order to obtain a rough estimate for M_c, we adopt masses of 3.0, 2.0, 1.0, 0.7, and 0.3 $M_\odot$ for B, A, G, K, and M stars, respectively. We then obtain an estimate for the group mass, based on the spectral types of individual *bona fide* members of the Association (Table 2.4), of $M_c \sim 28$ $M_\odot$[2]. Adopting this value of M_c, the tidal shredding radius of the group is found to be 4 pc, with a large uncertainty (given the large uncertainties in the estimates of the ϵCA and Galactic masses). Given the estimated group mass and this tidal radius, and assuming (for simplicity) a spherical stellar distribution, the mass density is $\sim$0.13 $M_\odot$ pc^{-3} and the stellar density is $\sim$0.18 pc^{-3}. This mass density is within a factor of 2 of the estimated local Galactic disk density ($\sim 0.1 M_\odot$ pc^{-3}; [106]), reflecting the fact that ϵCA is a diffuse association (as opposed to cluster). Inclusion of provisional members would increase the Association mass estimate to $36 M_\odot$ but negligibly change the aforementioned tidal radius and density calculations.

The spatial and kinematic structure of the final membership of the ϵCA is illustrated in Figure 2.6. The vast majority of group members ($\sim$80%) fall within the tidal shredding radius of the median group XYZ position, shown as the green shaded circle and red cross, respectively. The binaries in the group fall both inside and outside of the central region of the association, with no obvious correlation with position. Figure 2.8 illustrates the disk fraction versus distance from the median XYZ position of ϵCA. The figure indicates that 9 of the 11 ϵCA systems known to host disks lie within 5 pc of the median position, a volume roughly coincident with that defined by the group's tidal shredding radius; the disk fraction falls from $\sim$50% within 5 pc of the median position to $\sim$15% beyond 5 pc of the median. This centrally concentrated distribution suggests that stars in the core region of the ϵCA are more likely to retain dusty disks, hinting at the possibility that the nascent planetary systems orbiting stars in this region are subject to more frequent and/or more catastrophic dust-generating collisions. The distribution in Figure 2.8 stands in contrast to that of the (older) χ^1 For cluster (age $\sim$40

---

[2] Note that this estimate neglects the potential contribution to M_c of molecular gas possibly associated with ϵCA — or at least with T Cha — as evidenced by detection of interstellar CO at coincident RV [67].

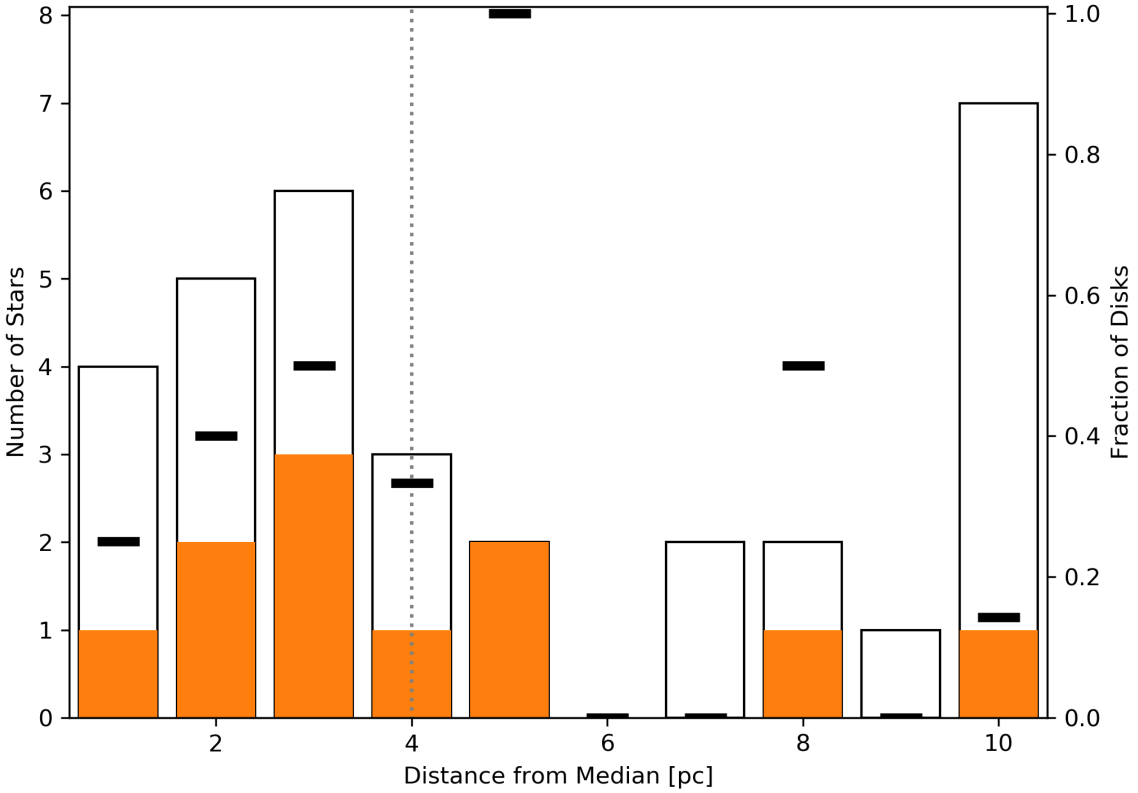

Figure 2.8: Histogram of the distance from the median XYZ position for the final list of ϵCA members (Table 2.4). The filled orange bars indicate stars with disks, and the disk fractions are represented as horizontal black lines. The tidal shredding radius (4 pc; Sec 2.5.2) is denoted by a vertical gray dashed line.

Myr), for which the majority of stars with IR excesses (hence dusty disks) lie in a narrow, spherical annulus just outside the tidal shredding radius of the cluster [72]. However, as noted by those authors, χ^1 For also represents a particularly striking and unusual case of a large disk frequency in a ∼40 Myr-old cluster.

2.5.3 Age of the Association

The SLFR analysis applied to ϵCA (§2.3.1) was additionally performed for two other NYMGs, the TW Hya Association (TWA) and β Pic Moving Group (BPMG). These NYMGs are both slightly older than ϵCA, at 8 Myr [107] and 24 Myr [108] respectively, and hence provide good references for the relative age of ϵCA as determined from their respective SLFR-based empirical isochrones. For our SLFR analysis, we used lists of stars considered *bona fide* members of each group [6], totaling 30 stars for TWA and 113 stars for BPMG.

The empirical isochrones for the three NYMGs are compared in the right panel of Figure 2.9. With the exception of BPMG, the blue ends of the empirical isochrones are not well fit, due to the small sample sizes in these regions, and are hence not plotted in Figure 2.9 (and are excluded from this discussion). All three of the empirical isochrones fit their respective NYMG data well in the regions $0.2 \leq G - R_p \leq 1.2$. In this CMD region, the empirical isochrones show the expected hierarchical pattern — i.e., with ϵCA highest, BMPG lowest, and TWA intermediate between the two — reflecting the relative ages of these three NYMGs. At redder colors, all three groups drop off in population and appear to display a larger degree of scatter, and hence the empirical isochrones (4th-order polynomials) do not provide as good a fit in these regions.

Three representative isochrones from Tognelli et al. (2018) [5] are shown in the right panel of Figure 2.9[3]. While the theoretical isochrones well match the Gaia NYMG data blueward of $G - R_p \sim 0.8$ (apart from the TWA, which lacks stars in this region), these curves fall below the Gaia data at regions redder than $\simeq$0.9 in $G - R_p$. This divergence between theoretical isochrones and data is commonly observed in Gaia CMDs, as previously noted (§ 2.3.1), and can likely be ascribed to the high levels of magnetic activity of late K and M stars (e.g., [74]).

Based on the close correspondence of the theoretical 5 Myr isochrone and the empirical (SLFR-generated) single-star isochrone in the region $0.5 \leq G - R_p \leq 1.0$, we estimate an age of 5^{+3}_{-2} Myr for ϵCA, where the range of uncertainty is based on the vertical offset of the 3 and 8 Myr theoretical isochrones in this same domain of $G - R_p$. This is consistent with the age range determined via theoretical isochrone analysis in the (pre-Gaia) M+13 study, i.e., a median of 3–5 $M_\odot$ for lower-mass stars (albeit with somewhat older inferred ages for solar-mass stars), as well as with the age obtained from a reanalysis of the M+13 data by Schutte et al. (2020) ($3.7^{+4.6}_{-1.4}$ Myr) [103]. Future age estimates for the ϵCA should be informed by spectroscopic observations designed to confirm the membership status of provisional members

---

[3] We found MIST isochrones [109, 110, 111, 112, 113] to be indistinguishable from the [5] curves, so only the latter are used as representative of the expected temporal behavior.

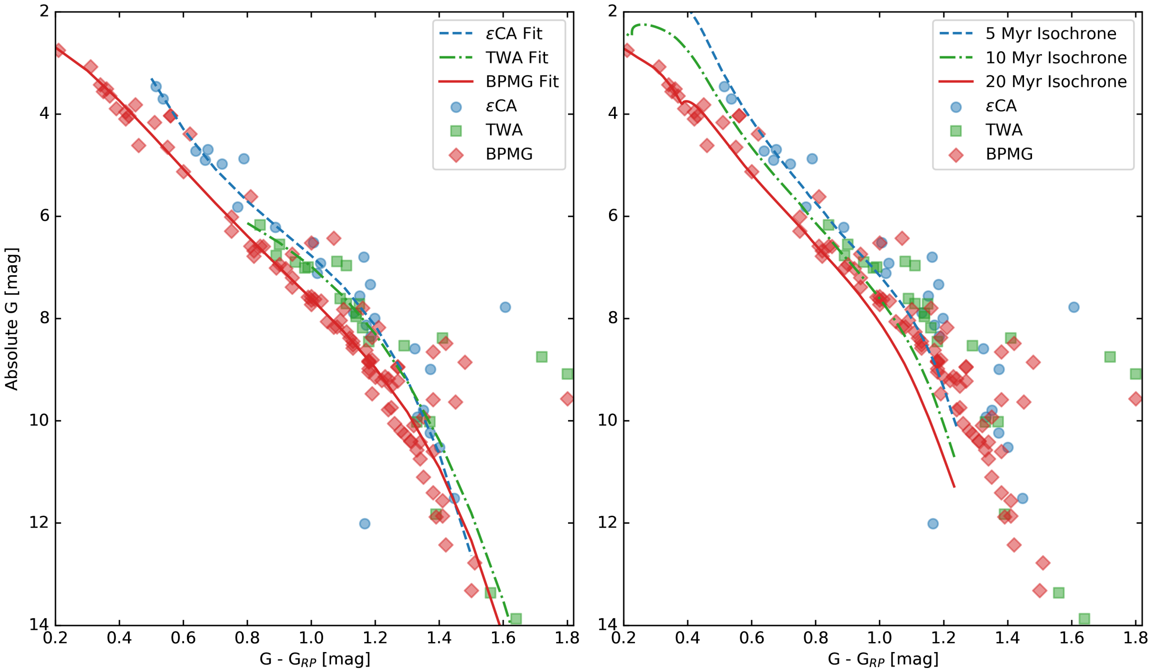

Figure 2.9: Gaia DR2 CMDs for ϵCA (Table 2.4; blue circles), the TW Hya Association (green squares), and the β Pic Moving Group (red diamonds), where data for the latter two groups are based on for the membership lists in Lee et al. (2019) [6]. In the left panel, the data for the three groups are overlaid with the corresponding empirical isochrones obtained from SLFR analysis (Secs. 2.3.1, 2.5.3). In the right panel, the data are overlaid with theoretical isochrones from Tognelli et al. (2018) [5] for ages of 5, 10, and 20 Myr.

(Table 2.5), a DR3-based search for additional members, and application of isochrones obtained from "magnetic" pre-main sequence evolution models (e.g., [114]).

2.6 Summary

We have used Gaia DR2 astrometric and photometric data to refine the membership of ϵCA, and have thereby established the distance (mean $D = 100.99$ pc, $\sigma_D = 4.62$ pc), age (5^{+3}_{-2} Myr), and spatial and kinematic distributions (Fig 2.6; Table 2.8) of the association. We confirm that ϵCA is significantly younger than both the TW Hya Association and β Pic Moving Group (Fig 2.9) and, hence, that ϵCA represents the youngest NYMG within ~100 pc of Earth. Our analysis includes the determination of an empirical relationship between Gaia $G - G_{RP}$ color and spectral type that should provide an accurate means to determine the spectral subtypes of ~5 Myr-old K and M stars from dereddened Gaia photometry.

Our analysis yields a final ϵCA membership list consisting of 36 *bona fide* members and 20 provisional members (Table 2.4; Table 2.5). The provisional members require followup study (in particular, RV determinations) in order to confirm their membership status kinematically. These include 3 new members of the ϵCA that we have identified via a search of Gaia DR2 for wide-separation, co-moving companions to previously identified members. One of these newly identified members is either a substellar object or an M star viewed through (and hence highly obscured by) a nearly edge-on circumstellar disk. We identified 5 photometric binaries among the group members, 3 of which are new binary star candidates.

Like other nearby stellar groups, the presently known membership of ϵCA is dominated by M stars, and the spectral type distribution peaks in the mid-M range. The multiplicity fraction of ϵCA (40%) is intermediate between those of the field star population and T associations. We find an overall circumstellar disk fraction of 30% for ϵCA, with the vast majority of disk-bearing stars lying within ~5 pc (Figures 2.6 and 2.8).

In providing a well-defined region of XYZ and UVW space encompassing this NYMG, this work sets the stage for a more complete search of Gaia DR2 (and eventual DR3) data for new members of ϵCA. This work thereby provides the framework for future investigations of the initial mass function as well as multiplicity and disk fractions of ϵCA.

Chapter 3

Investigating 2M1155-7919B: a Nearby, Young, Low-Mass Star Actively Accreting from a Nearly Edge-on, Dusty Disk

The following Chapter has been submitted and reflects revisions from the referee as [“Investigating 2M1155-7919B: a Nearby, Young, Low-Mass Star Actively Accreting from a Nearly Edge-on, Dusty Disk”, D.A. Dickson-Vandervelde, J. Kastner, J. Gagné, A. Schneider, J. Faherty, E. Wilson, C. Pinte, and F. Ménard, The Astrophysical Journal, September/October 2022]

3.1 Introduction

Nearby associations of young, comoving stars (generally referred to as Nearby Young Moving Groups; hereafter NYMGs) are prime candidates for studies of the early evolution of low-mass pre-main sequence (pre-MS) stars, juvenile brown dwarfs, and newly formed planets [115, 2]. In recent years there have been a handful of identifications of very wide (∼100–1000 AU projected

Table 3.1: 2M1155−79AB: Gaia EDR3 Astronomy and Photometry

Name	RA (deg)	Dec (deg)	π (mas)	PMRA (mas/yr)	PMDec (mas/yr)	G (mag)	G−G_{RP} (mag)	RUWE
2M1155−7919A	178.769132	-79.319756	9.81±0.03	-41.35±0.03	-4.56±0.031	14.803	1.333	1.196
2M1155−7919B	178.762736	-79.320829	9.49±0.43	-41.59±0.55	-4.63±0.51	19.954	1.396	1.104

separation) binaries consisting of young stars and substellar objects in these NYMGs, as well as in nearby star formation regions (HD 106906 b, 1RXS 160929.1-210524 B, CT Cha B, and DENIS-P J1538317-103850 [116, 117, 118, 119]). The 1RXS 160929.1-210524 B, HD 106096, and DENIS-P J1538317-103850 systems belong to the sprawling Upper Scorpius association and the CT Cha system to the Chamaeleon I star-forming region.

The faint 2MASS source J11550336-79191147 (henceforth 2M1155−79B) is a curious young, low-mass object that was discovered via a Gaia Data Release 2 (DR2, [33]) search for wide, comoving companions to known members of the ϵ Cha Association (ϵCA; $D \sim 100$ pc, age $\sim$5 Myr), which represents the nearest region of star formation of age <8 Myr [65, 64]. 2M1155−79B is the companion to 2MASS J11550486-7919108 (henceforth 2M1155−79A) with a projected separation of 5”.75, equivalent to 582 AU at PA 227.9° [63, 65]. Astrometry from Gaia Early Data Release 3 (EDR3) confirms that 2M1155−79A and 2M1155−79B are equidistant ($D = 101.4 \pm 0.3$ pc, [120]) and comoving, to within the uncertainties (Table 1). The M3 type star 2M1155−79A was previously known as T Cha B, following its identification as an apparent very wide-separation comoving companion to T Cha, host to one of the nearest known examples of a highly inclined protoplanetary disk [66]. However, Gaia DR2 subsequently revealed small but statistically significant differences between the parallaxes and proper motions of T Cha and 2M1155−79A [102][1].

Using substellar object population properties, Dickson-Vandervelde et al. (2020) [65] found that the J magnitude and J-H color of 2M1155−79B corresponded to a spectral type of M9/L0, which would place it just below the boundary between brown dwarfs and massive planets assuming its age is 5 Myr. This mass estimate would place 2M1155−79B in the interesting position of a planet orbiting its host (2M1155−79A) at a projected semimajor axis of ∼600

---

[1] Gaia EDR3 data appear to confirm that T Cha and 2M1155−79A are neither equidistant nor comoving (within the uncertainties).

AU — similar to the projected separations of the aforementioned substellar-object-hosting systems HD 106906, 1RXS 160929.1-210524, CT Cha, and DENIS-P J1538317-103850.

Very large separations between host star and orbiting substellar object appear in conflict with broadly accepted theories of planet formation, i.e. core accretion or gravitational instability, because there is not enough material within protoplanetary disks at radii beyond 100 AU to form planets [3]. The observed wide separations of these systems may be better explained via dynamical models where the planet either formed at smaller radii and was ejected, or has been gravitationally captured into the system from other systems within the group [121, 122]. A study of the Upper Scorpius young stellar association finds an excess of free floating planets that are best accounted for by dynamical instabilities within the first 10 Myr [123]. It is possible that both a young star and its wide-separation, substellar companion have formed via "standard" star formation mechanisms; indeed, studies of planetary-mass objects in NYMG suggests that substellar objects down to a few Jupiter masses may form in such a manner (e.g. [124]).

In this paper, we present near-infrared (NIR) spectroscopy of the 2M1155−79AB system along with analysis of available Gaia EDR3, 2MASS, and WISE photometry. The results suggest a different nature for 2M1155−79B: namely, that it is a low-mass star partially occulted by, and actively accreting from, a highly inclined, dusty disk. In Section 3.2, we describe the NIR spectroscopic observations. In Section 3.3, we present the results of these observations along with analysis of archival photometry of the 2M1155−79AB system. In Section 3.4, we discuss the evidence for a disk around 2M1155−79B and compare the object to 2M1155−79A. We also compare the 2M1155−79B star-disk system to a set of potentially analogous very low-mass star-disk systems: fellow ϵCA member 2MASS J12014343-7835472, member of the 8 Myr TW Hys Association TWA 30B, and the 1-5 Myr-old DENIS-P J1538317-103850.

3.2 Observations

Near-IR spectra were obtained on February 12 and 13, 2020 (hereafter Night 1 and Night 2, respectively) using the FIRE instrument on the 6.5 m Magellan telescope. FIRE spectra

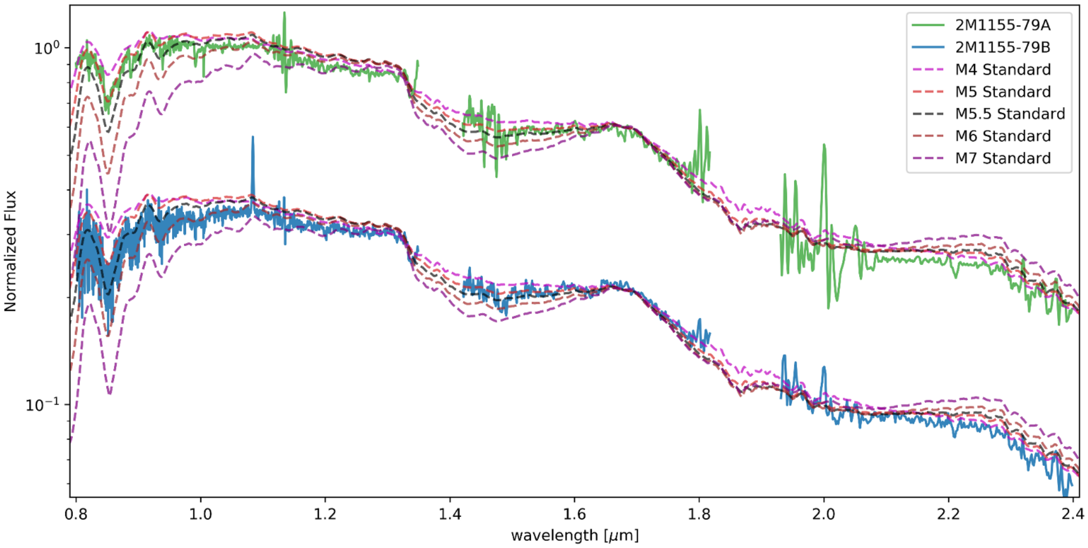

Figure 3.1: Near-IR spectra obtained with the FIRE instrument on Magellan for 2M1155−79A (green) and 2M1155−79B (blue). The flux of both FIRE spectra has been normalized and then a constant offset was applied to separate the two spectra for visualization. Five spectra from the Luhman et al. (2017) Young Star Spectral Library, M4 (magenta) M5 (red), M5.5 (black), M6 (brown), and M7 (purple), are also displayed with intensities adjusted to match the FIRE spectra at 1.7 μm [7].

were obtained in prism mode, which has a resolving power of ∼450 across the 0.8–2.5 μm spectral range. Observations of 2M1155−79B were obtained both nights and observations of 2M1155−79A were obtained on Night 2 (Fig. 3.1).

The FIRE data were reduced using a custom version of the FIREHOSE pipeline based on the MASE pipeline [125] written in the Interactive Data Language (IDL)[2]. This modified version includes subroutines of the SpexTool package [126, 127] to facilitate the rejection of bad pixels and detector hot spots when the 1D extracted spectra of individual exposures. All raw exposures were flat-fielded, and then extracted using the optimal extraction algorithm included in FIREHOSE, and finally combined using the default Robust Weighted Mean option (Robust threshold = 8.0). We used Neon-Argon lamp exposures to determine the wavelength calibration. The signal-to-noise per resolution element is approximately 180 (70 per pixel) for 2M1155−79B and about 260 (100 per pixel) for 2M1155−79A.

---

[2] Available at `https://github.com/jgagneastro/FireHose_v2`

While the overall shape and features of the spectra for 2M1155−79B did not change between Night 1 and Night 2, the spectrum obtained on Night 1 displays lower signal-to-noise ratio (SNR), especially in the ∼2 μm region. Hence, the analysis and discussion in this paper refers to the Night 2 spectrum, unless otherwise specified.

Although the majority of ϵCA members show no significant intervening reddening, 2M1155−79AB is seen projected toward the middle of a small dust cloud [63]. Hence, the spectra of both components were dereddened via the python package `dust_extinction` using the Fitzpatrick et al. (2019) [128] reddening model. We adopted $E(B-V) = 0.5$ for 2M1155−79A [63], which equates to $A_J \approx 0.44$, assuming the standard value of $R_V = 3.1$ (e.g., [97]). Note that this dereddening process does not account for other sources of spectral distortion, such as obscuration or scattering by circumstellar disk material.

3.3 Results

3.3.1 NIR Spectra

In Figure 3.1, we present the dereddened Magellan/FIRE spectra for both 2M1155−79A and 2M1155−79B overlaid with a range of near-IR spectra of late-M young star spectral standards from Luhman et al. (2017) [7] (henceforth referenced as L17). With no adjustments on the flux of the two spectra, the 2M1155−79A spectrum is on average 10.2× brighter than its companion. After accounting for the factor of 10 difference in flux from the two objects, the spectral shapes of 2M1155−79A and 2M1155−79B are very similar, with some small differences in the depth of the 0.8 μm absorption feature that could be due to noise (see the two spectra overlaid in Fig. 3.2). The center of the 1.4−1.8 μm region of the spectrum of 2M1155−79B also potentially shows a larger bump than that of 2M1155−79A, indicative of a slightly later spectral type. Notably, the spectrum of 2M1155−79B displays a strong 1.083 μm He I emission feature that is absent from the spectrum of 2M1155−79A.

The overall strong similarity of the Magellan/FIRE spectrum of 2M1155−79B to that of 2M1155−79A indicates that the two components are very similar in spectral type, notwithstanding the factor ∼10 smaller flux from 2M1155−79B. As is discussed in detail below, this is a surprising result, given that (as noted) 2M1155−79A has been classified as M3 [66, 63] whereas 2M1155−79B was initially considered a candidate substellar object [65]. The previous optical spectral type for 2M1155−79A was from a limited wavelength range, which may account for the earlier spectral type. Additionally, while the comparison of the near-IR spectra of the 2M1155−79AB paired with those of the L17 standard spectra in Figure 3.1 does leave some ambiguity as to the M spectral subtypes of 2M1155−79A and 2M1155−79B, it is readily apparent that the near-infrared spectral type of the former component is later than M3.

The comparison of the overall shapes of the FIRE spectra with those of the L17 young star standard spectra demonstrates that a spectral type of M7 or later can be ruled out; note in particular the flatter slope of both 2M1155−79A and B in the 1.4–1.8 and 1.9–2.4 μm regions relative to the M7 standard. The 2.2 μm Na I absorption line is present in both FIRE spectra, although it is not present in the standards, and the line depth is in agreement with a mid- to late-M spectral type. The 0.8–0.9 μm range of 2M1155−79B has a lower SNR than other regions of the spectrum and so the TiO feature matches with a larger range of spectral types; 2M1155−79A is less noisy in that range and more precisely matches to the M5–M6 standard. Again, the slope of the M7 standard is more pronounced than either 2M1155−79A or B. Hence, a spectral type in the range of M5–M6 is the best match for both 2M1155−79A and B.

3.3.1.1 The He I Feature

Both (Night 1 and 2) spectra of 2M1155−79B data show the presence of a strong He I 1.083 μm emission line (Figures 3.2 and 3.3). The emission line is unresolved, placing an upper limit of ∼670 km s^{-1} on its velocity width. The equivalent widths (EWs) of the 1.083 μm emission line, as measured via Gaussian fitting, were 11.9 ± 0.6 Å and 12.6 ± 0.4 Å for the Night 1 and 2 spectra, respectively.

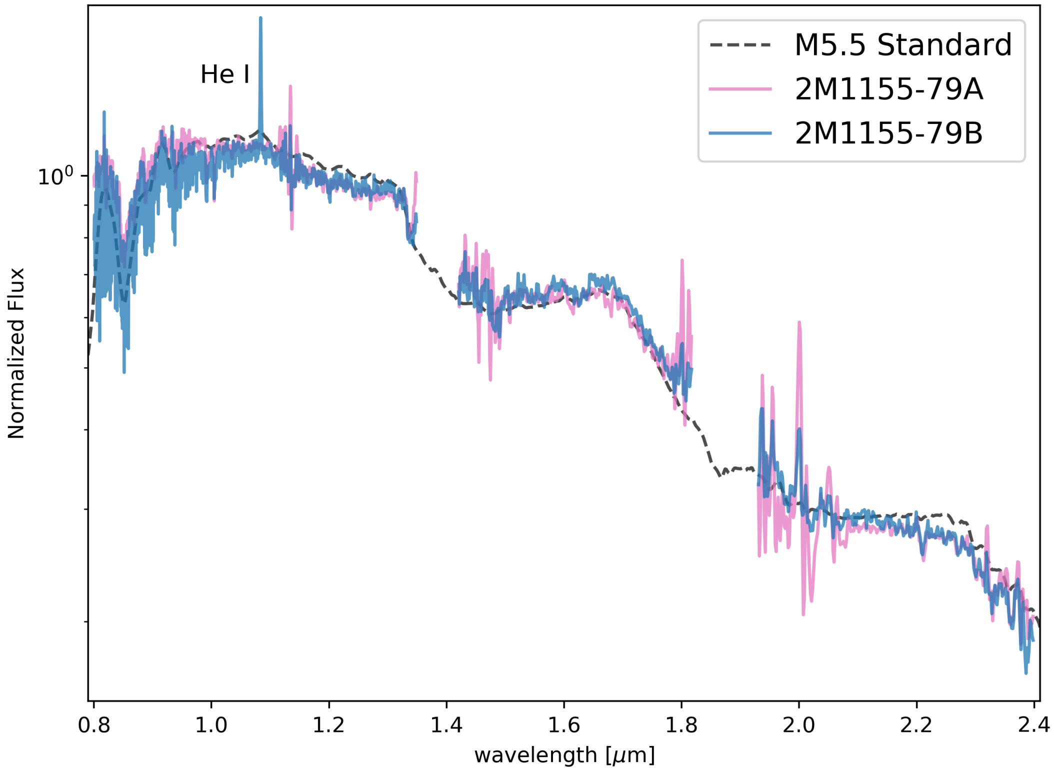

Figure 3.2: Near-IR spectra of 2M1155−79A (green), 2M1155−79B (blue), and a M5.5 standard (dashed black) are displayed with fluxes normalized so that the flux value is 1 at 0.85 μm. Aside from the 1.083 μm He I emission line seen in 2M1155−79B, no other emission lines are detected in either star. Notably, the two companions have very similar morphologies with the exception of the He I emission line.

3.3.1.2 Low Gravity Features

In Figure 3.3, we present the Night 1 and 2 FIRE spectra for 2M1155−79B split into the J band (0.80–1.35 μm), H band (1.42–1.82 μm), and K band (1.93–2.40 μm) regions. We highlight regions of potential spectral features that are sensitive to stellar surface gravity and useful for gravity indexing spectral types of M6 and later [129], along with the previously noted He I emission line. Both the 1.14 and 2.21 μm Na I absorption lines are visible, consistent with a mid/late-M classification (see above); the Na I feature is not present in lower-mass objects. The three FeH features (0.99, 1.20, and 1.55 μm) are not detected at the current signal-to-noise ratio; this is in agreement with with the morphological spectral type of M5–M6

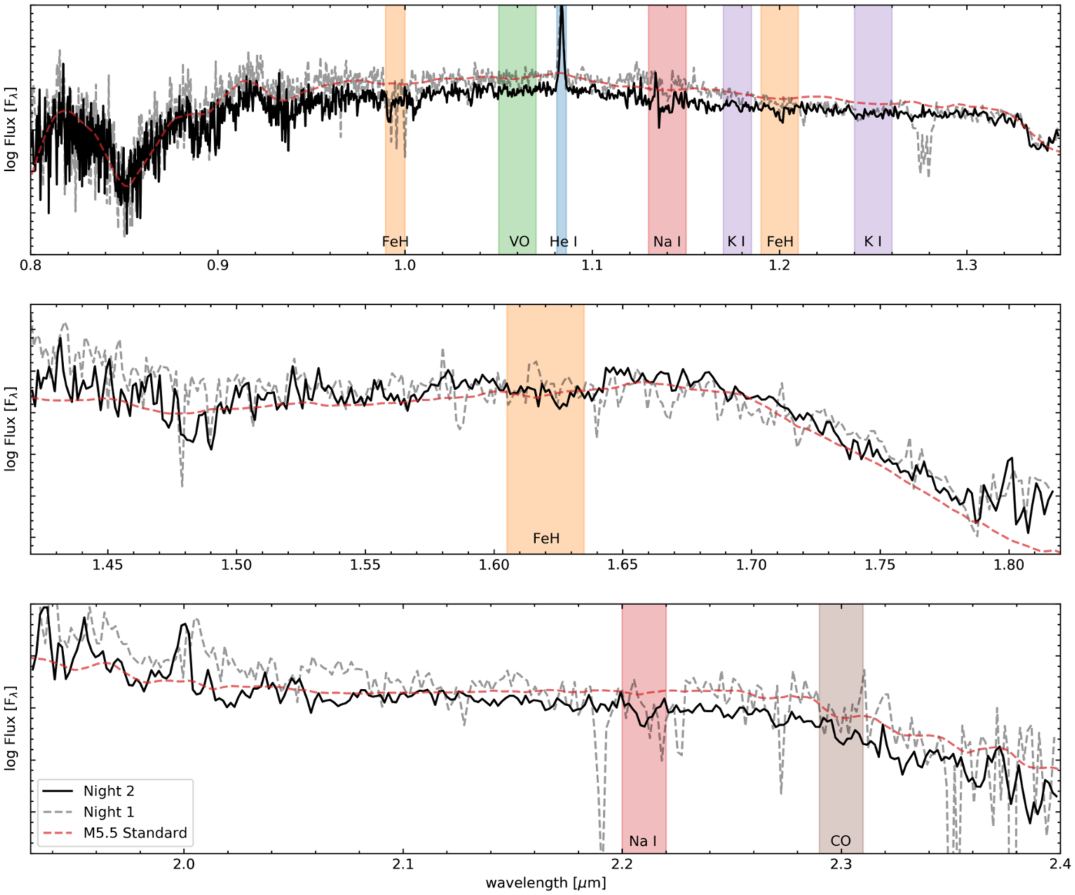

Figure 3.3: Both nights of FIRE spectra for 2M1155−79B, Night 1 (dashed grey) and Night 2 (solid black), along with the M5.5 young star standard spectra (dashed red), are split into three wavelength windows, 0.80 - 1.35 μm, 1.42 - 1.82 μm, and 1.93 - 2.40 μm. Windows for multiple low-gravity features are overlaid and labeled: FeH, VO, Na I, K1, and CO. The He I emission line is also labeled.

for 2M1155−79B indicated by Figure 3.1 as deeper FeH spectral lines are indicative of later (late-M to early-L) spectral types.

3.3.2 WISE Image Centroids

Mid-infrared 3.6, 4.5, 12, and 22 μm (W1, W2, W3, W4 band) images of the 2M1155−79AB binary system obtained by Wide-field Infrared Survey Explorer (WISE) are presented in Fig. 3.4. The angular resolution of WISE is comparable to the 2M1155−79AB system separation ($\sim$6″); however, it is apparent that the source centroid shifts from W1 (3.6 μm) to W4 (22 μm) by a displacement similar to this angular offset. In order to determine which component dominates each WISE band, we performed a centroid analysis on all four WISE bands and calculated the shift of center of the point spread function (PSF) between the four bands. We used two methods to determine the center of the WISE emission: Gaussian PSF centroid fitting and peak-pixel position determination. The two methods yield the same results to within the uncertainties (Fig. 3.4). Considering the SED morphologies of 2M1155−79A and 2M1155−79B (see Sec 3.3.3, Fig. 3.5), the majority of the flux in W1 is presumed to be from 2M1155−79A and, ergo, we consider the photocenter found via our analysis of the W1 image to be the position of 2M1155−79A.

The measured offsets with respect to W1 are 0.03" (PA = 270°), 1.44" (PA = 242°), and 4.14" (PA = 229°) in the W2, W3, and W4 band images, respectively. The W4 angular offset and PA, relative to W1, are similar to the projected separation (5.75") and PA (227°) of 2M1155−79B, relative to 2M1155−79A [65]. Analysis of unWISE yields similar results [130]. We conclude that 2M1155−79A dominates the flux in the shorter WISE bands (W1 and W2), while the contribution from 2M1155−79B becomes significant at 12 μm (W3) and dominates the flux at 22 μm (W4). Thus, the mid-IR excess due to thermal emission from circumstellar dust — originally attributed to 2M1155−79A [66, 63] — is in fact associated with 2M1155−79B (see next).

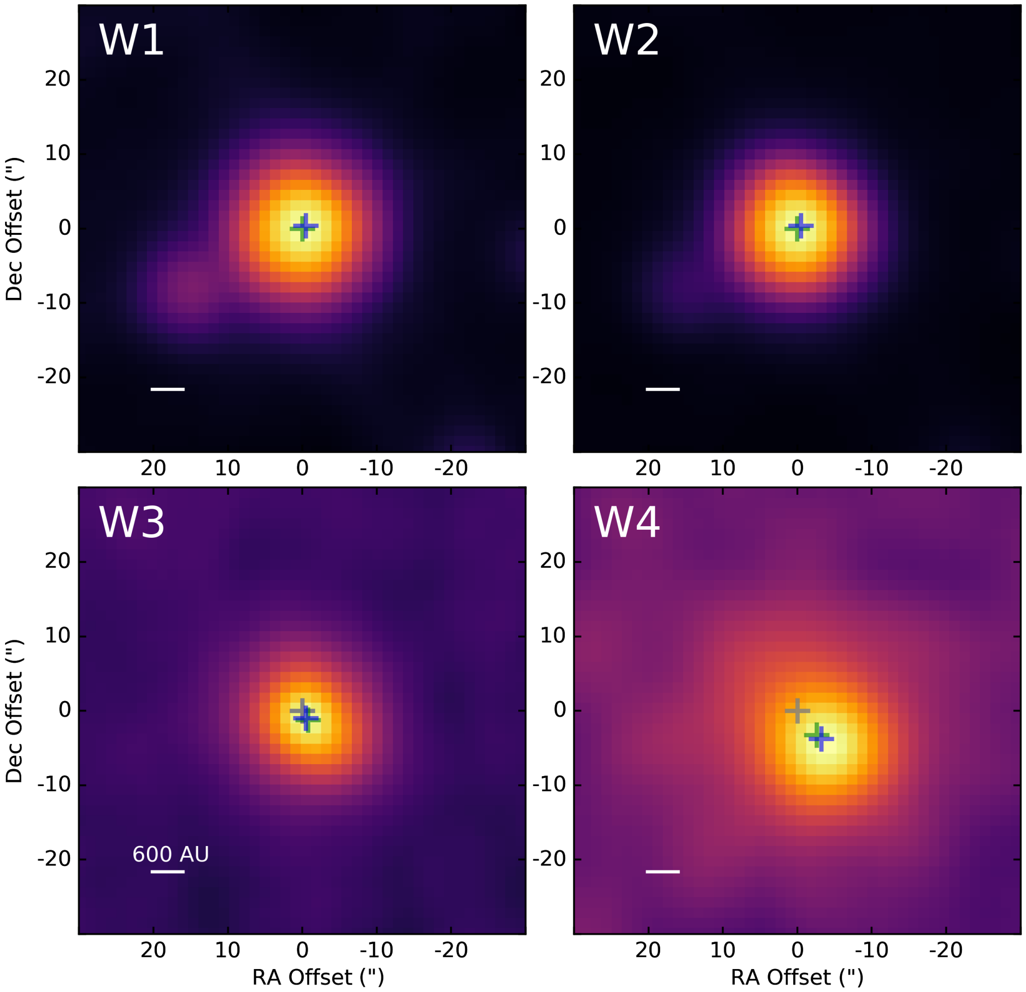

Figure 3.4: Four WISE archival log-scaled images of the 2M1155−79AB system, W1, W2, W3, and W4 (3.6, 4.5, 12, and 22 microns) as labeled. Images are aligned in RA/Dec coordinates, (0,0) being the position of the W1 centroid and are 60″x60″. The white bar on each image represents the equivalent distance of ∼600 AU, the green plus sign marks the center of the PSF as found via a Gaussian, the blue plus sign marks the center of the PSF as found via the peak pixel value, and the grey plus sign in the W3 and W4 images marks the W1 (0,0) position.

3.3.3 SEDs

In addition to photometry from WISE [11], archival photometry is available for both 2M1155−79B and 2M1155−79A from Gaia EDR3 [9], 2MASS [10], and the Vista Hemisphere Survey [131]. The visible and NIR magnitudes were de-reddened for 2M1155−79A and 2M1155−79B following the same procedure used for the FIRE spectra (see Sec 3.2). The resulting spectral energy distributions (SEDs) generated from these archival data are presented in Fig. 3.5. Throughout the optical and mid-IR SED, there is a factor of ∼100 luminosity difference between A and B. This is discrepant with the near-IR flux ratio seen in the FIRE data (∼10). Although the flux ratio measured in the FIRE spectra may be unreliable, due to possible chromatic effects from slit placement as well as possible saturation in the J-band portions of the spectra of 2M1155−79A and the (A0) flux calibration standard, the large discrepancy between the 2MASS flux ratios and the FIRE spectral ratio is indicative of possible variable obscuration of 2M1155−79B (see below).

Based on the W3 flux upper limit and the W4 flux, using a blackbody we find that the upper limit on the temperature of the warmest circumstellar dust associated with 2M1155−79B is ∼200 K. Presuming that the W4 flux arises primarily from 2M1155−79B (Sec 3.3.2), there appears to be no significant circumstellar dust component associated with 2M1155−79A.

3.4 Discussion

3.4.1 The Two Components of 2M1155-79

As noted in Sec 3.3.1, the near-IR SED revealed by the FIRE spectra of 2M1155−79B is strikingly similar to — albeit significantly fainter than — that of 2M1155−79A (Fig. 3.1). In addition to the large flux ratio, a glaring distinction between the two spectra is the presence of the He I 1.083 μm emission line in 2M1155−79B. The WISE analysis reveals that the IR excess originally associated with 2M1155−79A, instead arises from 2M1155−79B (see Sec. 3.3.2). This, combined with the He I emission, constitute strong evidence for the presence of a disk surrounding, and accreting onto, 2M1155−79B. Edge-on disks appear unusually faint in optical

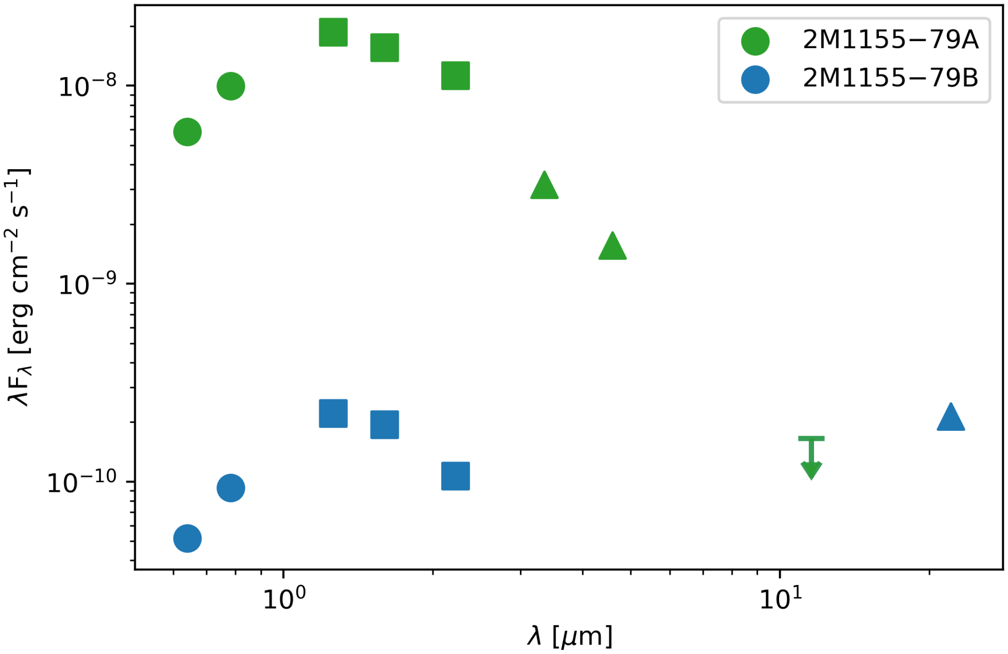

Figure 3.5: The SED of both 2M1155−79B (in blue) and 2M1155−79A (in green) from available archival visual and infrared data. Circles represent fluxes from Gaia EDR3 (G and G_{RP}), squares represent fluxes from 2MASS (J, H, and K), and triangles represent fluxes from WISE (W1, W2, W3, and W4). The J and K fluxes for 2M1155−79B are from the Vista Survey. Due to the WISE PSF being larger than the separation of 2M1155−79A and B, the WISE fluxes are separated by which object dominates the band (see Sec 3.3.2). The downward arrow represents the W3 upper limit on the flux for both objects since the photometry is ambiguous for which source dominates it.

and NIR bands compared to the expected luminosities of a given spectral type, while still presenting an IR excess at longer wavelengths. This is because scattered stellar light off of the disk dominates the luminosity in the optical and NIR (accounting for the faintness), while thermal emission from the dust dominates longer wavelengths. Its very low apparent luminosity and red Gaia/2MASS colors [65] hence could be due to obscuration of the stellar photosphere by this orbiting, dusty accretion disk.

As an initial investigation of this hypothesis, we used the radiative transfer modeling code MCFOST [61, 62] to generate two models for the combined star and disk system of 2M1155−79B that can reproduce its double-peaked optical through mid-IR SED, as illustrated in Fig. 3.6. These models represent two extremes of stellar luminosity, 0.010 $L_\odot$ and 0.025 $L_\odot$, with the stellar effective temperature fixed at 3000 K using the Baraffe et al. (2015) [31] stellar spectra models, corresponding to the expected range of stellar properties for ∼5 Myr-old M5/M6 pre-MS stars. For both scenarios, we utilized a tapered-edge disk model composed of astronomical silicates — separated into small (0.01–7 μm) and large (7–3000 μm) grains — with a flaring exponent of 1.07 and a disk scale height of 7 AU at a reference radius of 100 AU [62]. We fixed the large grain dust disk mass at 2.0×10^{-5} $M_\odot$ and the small grain dust disk mass at 1.5×10^{-6} $M_\odot$. The small dust grain component remained the same between both models with an inner radius of 0.015 AU and outer radius of 60 AU. To match the observed SED, we find that the 0.010 $L_\odot$ model requires a disk inclination of 75° and an inner radius of 0.2 AU for the large dust grains, while the 0.025 $L_\odot$ model requires an inclination of 81° and an inner radius of 0.45 AU for the large dust grains. We also display the corresponding models for an inclination of 0° (i.e., pole-on) in Fig. 3.6; these models support the conclusion that obscuration by the disk is responsible for the observed weak stellar photospheric emission signature in the 2M1155−79B SED. These initial MCFOST modeling results (Fig. 3.6) thus lend strong support to the scenario wherein the observed SED of 2M1155−79B results from a highly inclined circumstellar disk.

In contrast, given the WISE data (and lack of He I emission), we can now conclude that there is no evidence for a circumstellar disk around 2M1155−79A. The NIR spectra (Fig. 3.1) indicate that both 2M1155−79A and B are mid- to late-M (M5/6) type stars, whereas optical spectroscopy of 2M1155−79A previously established the star as spectral type M3 [66, 63]. The discrepancy between these near-IR (M5/6) and optical (M3) spectral classifications is not without precedent; it has been previously noted that the optical spectral classifications of pre-MS stars can be 3–5 subclasses earlier than their NIR-based classifications [132, 133]. As noted in Sec. 3.3.1, the earlier spectral type could instead by erroneous due to the limited wavelength range in the spectrum used for classification.

Furthermore, our MCFOST modeling demonstrates that the occultation of 2M1155−79B by this disk — rather than a difference in stellar mass (hence luminosity) — also most likely

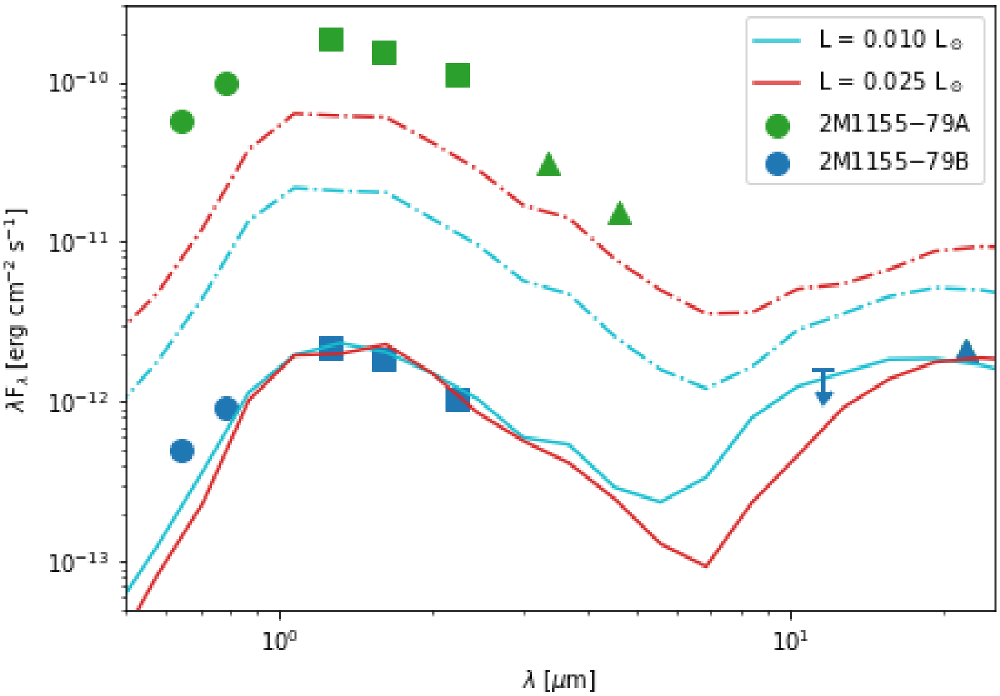

Figure 3.6: The SED of 2M1155−79B (blue points) with two MCFOST models overplotted; the SED of 2M1155−79A (green points) are also plotted as a reference. The data markers are indicative of the same photometric bands as is listed in the caption of Fig 3.5. The cyan line is the highly-inclined model corresponding to a stellar luminosity of 0.010 $L_\odot$ and the red line is the highly-inclined model corresponding to 0.025 $L_\odot$. The dash-dot lines correspond to the respective pole-on models for 0.010 and 0.025 $L_\odot$.

accounts for much of the enormous flux difference between 2M1155−79B and 2M1155−79A throughout the optical and NIR. The strong similarity of the FIRE spectra of 2M1155−79A and 2M1155−79B, and their factor ∼10 difference in flux levels, should translate to very similar 2MASS colors and a systematic difference of ∼2.5 mag in the 2MASS photometry. The redder 2MASS $J - H$ color of 2M1155−79B, and the overall ∼5 mag difference between the two components in the 2MASS data hence strongly suggests that, at the epoch of the 2MASS survey (1998), 2M1155−79B was more heavily occulted by its disk than when we observed in 2020. Additionally, the Gaia EDR3 photometry of 2M1155−79B is not as red as the photometry from DR2 ($G - G_{RP}$ = 1.40 vs. 1.74), which might constitute additional evidence for variable obscuration of the star by its disk or could be an erroneous measurement of G_{RP} from DR2.

Such variable obscuration is frequently observed in analogous highly inclined star/disk systems (see § 3.4.2). Gaia color variability would seem to be inconsistent with the very highly inclined (i∼80°), optically thick disk invoked in our models, however; the photospheric component in these models is dominated by scattering, such that the optical/near-IR colors should be saturated and (hence) constant. Additional photometric monitoring of this system, along the lines of that conducted for TWA 30AB (see next), is clearly warranted.

3.4.2 Comparison to Analogous Systems

Various systems share qualities with the 2M1155−79AB system and provide useful comparisons. We compare some of the more well-studied objects in this section. The first two interesting objects for comparison are two nearby, low-mass pre-MS systems that also display evidence for a highly inclined disk: 2MASS J12014343-7835472 (henceforth 2M1201−78) and TWA 30B. 2M1201−78 is an early M-type star (∼M2.25) that is also a member of the ∼5 Myr ϵCA [98, 64]. As well as hosting a highly inclined disk (i∼84°), optical spectroscopy showed some signs of ongoing accretion in the form of emission from lines of He I, [S II], and the Ca II triplet, although other signatures were not detected. Fang et al. (2013) attribute the lack of some accretion signatures to a sparse inner disk [99].

A known member of the TW Hya Association (∼8 Myr), TWA 30B is an M-type (M3/M4) pre-MS star that is a wide-separation (∼ 3400 AU) companion to TWA 30A [134]. Like the 2M1155−79AB system, TWA 30B is fainter than its companion TWA 30A in optical and NIR; it has 5 magnitudes fainter than TWA 30A despite having a slighter earlier spectral type. The TWA 30B disk has been detected via its WISE excess emission and ALMA sub-mm continuum emission [135, 8]. Optical and NIR spectra of TWA 30B not only show He I emission lines, but also multiple forbidden lines (such as [OI], [OII], and [CI]) indicating that the system is actively accreting and likely drives jets [134].

In Fig. 3.7, we compare the SEDs of 2M1155−79B, 2M1201−78, and TWA 30B, as compiled from data from Gaia EDR3, 2MASS, the Vista Hemisphere Survey, and WISE. The SEDs are overlaid with composite blackbody curves approximating the stars' photospheric and disk

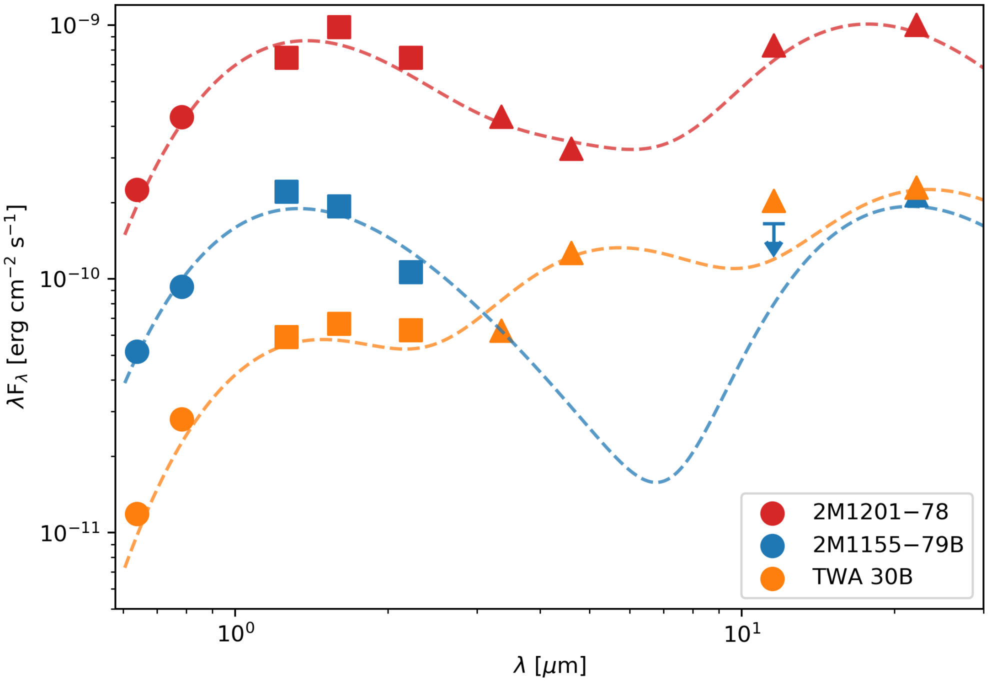

Figure 3.7: The SEDs of 2M1155−79B (in blue), TWA 30B (in orange), and 2M1201−78 (in red) displayed on a log-log scale. Circles represent fluxes from Gaia EDR3 (G and G_{RP}), squares represent fluxes from 2MASS (J, H, and K), and triangles represent fluxes from WISE (W1, W2, W3, and W4). The J and K fluxes for 2M1155−79B are from the Vista Survey. The downward arrow denotes the 2M1155−79B W3 flux as an upper limit. The fluxes of all three systems have been normalized to a uniform distance of 10 pc. The dashed lines indicate the combined blackbody model for each system. The stellar photospheres are modeled as simple blackbodies and are not indicative of the actual stellar effective temperatures. The photospheric blackbodies for each system, scaled to the H-band flux, are 2750 K for 2M1155−79B, 2500 K for TWA 30B, and 2650 K for 2M1201−78. The remaining excesses (corresponding to the disks) are modeled using two blackbodies for 2M1201−78 ($T = 200, 750$ K) and TWA 30B ($T = 150, 620$ K; [8]) and a single blackbody for 2M1155−79B ($T = 170$ K).

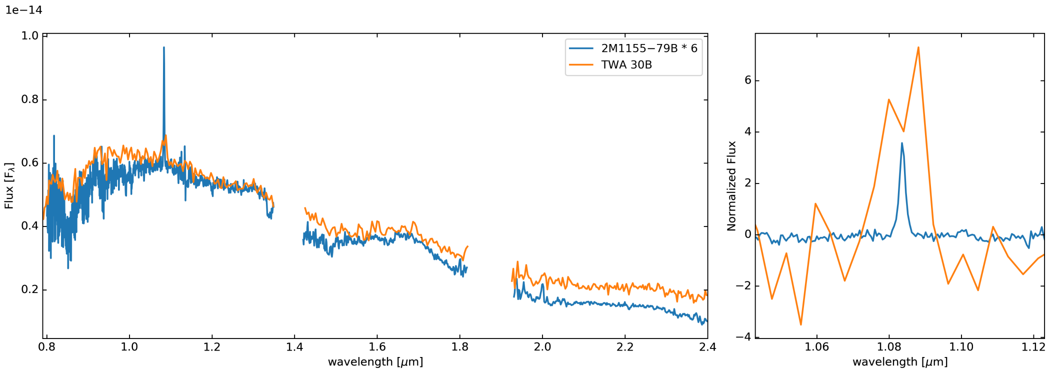

Figure 3.8: Two IR spectra are displayed in both panels: 2M1155−79B (blue, taken with the FIRE instrument) and TWA 30B (orange, taken with the SPeX instrument). In the left panel, the 2M1155−79B spectrum has been normalized for visualization with the TWA 30B spectrum by the entire spectrum being multiplied by a constant of 6 and shows the full wavelength coverage. The right panel is centered on the He I 1.083 emission line and both fluxes have had the continuum flux subtracted and normalized to 0.

emission (dashed lines). Only the photometric data for 2M1155−79B have been dereddened; the ϵCA region toward 2M1201−78 appears to show minimal interstellar reddening [63], while the TWA 30B system displays variable reddening due to its dusty circumstellar disk [134, 136].

While the three objects are similar in nature, their corresponding SEDs indicate two separate disk morphologies. TWA30B has a flat SED, indicative of a ‘full’ disk with no significant inner cavity, while 2M1201 appears to have a clear break between the stellar and disk blackbodies, indicative of an inner disk cavity, as hypothesized by Fang et al. (2013) [99]. This is also congruous with the accretion signatures from the two objects: 2M1201 has weaker accretion signatures than TWA 30B [99, 134]. Because of WISE’s inability to cleanly resolve 2M1155−79B from A, we are unable to establish which of these contrasting disk structures might best characterize 2M1155−79B.

Figure 3.8 compares the NIR spectra of 2M1155−79B and TWA 30B, including the strengths of the He I 1.083 μm emission lines. The TWA 30B IRTF-SpeX spectrum (obtained on 8 June 2011) was among the NIR spectra presented in [136] least affected by the variable reddening of TWA 30B. The comparison shows that TWA 30B, at M4 [134, 136], is of earlier M type than 2M1155−79B, further supporting our earlier determination of a NIR spectral type of M5/6 for 2M1155−79B (Sec 3.3.1). As noted in Sec 3.4.1, the apparent optical/near-IR photometric and color variability of 2M1155−79B suggests that it experiences variable obscuration by its highly inclined disk; curiously, this behavior more closely resembles that of TWA 30B's wide-separation companion, TWA 30A, than TWA 30B itself [134, 136]. The disk surrounding TWA 30A is most likely less highly inclined than its companion, as TWA 30A is brighter in the optical/near-IR and, unlike TWA 30B, has been detected in X-rays [134, 136].

The 1.083 μm He I line EWs of the two systems are similar: we measure 20 Å for TWA 30B, i.e., slightly larger than measured for 2M1155−79B (12 Å; Sec 3.3.1). The line is unresolved in both spectra and hence the EW could be underestimated, in addition to the high SNR in the TWA 30B spectrum making the EW less reliable. The low resolution also means we are unable to reliably compare the linewidths.

Another low-mass pre-MS star pair that warrants comparison to 2M1155−79AB is the potential wide binary DENIS-P J1538316-103900 (DENIS1538-1039) and DENIS-P J1538317-103850 (DENIS1538-1038). DENIS1538-1038 is a ∼1 Myr-old brown dwarf (spectral type M5.5) with an IR-excess indicative of a disk [119]. The M3 star DENIS1538-1039 is seen at 10″ projected separation from DENIS1538-1038. The two stars are potential members of the Upper Scorpius Association, although they are much younger than the average age of the association (∼10 Myr [137]). On the basis of Gaia DR2 data, Nguyen-Thanh et al. (2020) [119] concluded that the pair represent a chance line of sight alignment of two members of the same NYMG. However, in Gaia EDR3, the two components have the same proper motions and parallaxes within the uncertainties, indicating the two stars could be a wide binary. This would make this system analogous to 2M1155−79AB: a wide separation pair of young M-stars near the stellar/sub-stellar boundary, one with a disk and one without.

Two other systems merit mention here, as potential younger analogs to the 2M1155−79AB wide binary. Like 2M1155−79B, the companion to the 1–2 Myr-old 2MASS J19005804−3645048 was initially thought to be a planet-mass object before follow-up spectroscopy instead suggested that the star was a young late-M dwarf [138]. Christiaens et al. (2021) [138] discuss the implication that the companion is an obscured low-mass star for which only a small fraction of its light emerges due to an edge-on disk, as well as the possibility that the companion is an accreting protoplanet that is being heated by accretion shocks. It is unlikely that 2M1155−79B falls into this second category, given the lack of WISE detection of warm dust around 2M1155−79A (§ 3.3.2). The second system, HK Tau AB, is a low-mass, wide binary in the Taurus star forming region that, like 2M1155−79AB, consists of two stars of similar (in this case, early-M) spectral type, but with B many magnitudes fainter than A [139]. NIR imaging of the system revealed that HK Tau B is occulted by an edge-on disk [140]. Subsequent scattered light and sub-mm observations demonstrate that both components possess extensive gas and dust disks, but with sharply contrasting inclinations (i∼43° and i∼85° respectively; [141, 142]).

It is also worth considering whether 2M1155−79AB, as well as some of the aforementioned systems, constitute examples of young, hierarchical multiples wherein at least one component harbors a relatively long-lived, dusty disk [102]. There are multiple instances of circumbinary disks in such systems, as well as young hierarchical multiple systems showing the presence of disks around some components and not others; the HD 104237 system within ϵCA is an example of a particularly complex system with both of these characteristics [63, 64]. Thus far, however, there is no evidence that 2M1155−79AB is such a (hierarchical) multiple system (in particular, DR2 photometry are consistent with 2M1155−79A being a single star; [64]).

3.4.3 The Nature of 2M1155-79B

While the original evidence in Dickson-Vandervelde et al. (2020) [65] pointed towards 2M1155−79B being a nascent, 10 M_{jup} planet, the spectral type determined here, M5/6, is inconsistent with this picture. Nonetheless, 2M1155−79B is potentially still below the hydrogen burning limit; pre-MS model evolutionary tracks place the stellar versus brown dwarf boundary around a spectral type of M6 at 3-5 Myr [31]. A firm conclusion as to the fate of 2M1155−79B — low-mass star or brown dwarf — will require optical spectroscopy to confirm the spectral type of this enigmatic system.

To our knowledge, 2M1155−79B is the latest M-type pre-MS star in which the He I 1.083 μm emission line has yet been detected. In higher-mass pre-MS (T-Tauri) stars, this line is a sensitive probe of accretion shocks and accretion-driven winds [143], manifested in the form of red- and blueshifted absorption features that are a consequence of the high 1.083 μm line opacity [144, 145, 146]. For a high-inclination star-disk system with stellar and/or disk winds, the He I 1.083 μm emission has a narrow, blue-shifted absorption feature due to the emission passing through the slow disk wind component [143]. Given the resolution of our spectra, we cannot retrieve any information about potential blue-shifted absorption; however, the EW of the emission line from 2M1155−79B is similar to that of mid-K classical T Tauri star disks [147], and our initial modeling supports the presence of a nearly edge-on circumstellar disk in the system (Fig 3.6). Modeling by Kwan & Fisher (2011) [145] indicates that He I emission could be arising from the accretion flow close to a stellar impact shock, resulting in UV photoionization and temperatures of at least 10^4K. However, since 2M1155−79B has a much lower mass and therefore should have a lower shock temperature than in the Kwan & Fisher (2011) [145] models, the He I 1.083 μm could be indicative of the presence of a large-scale wind or jet. NIR imaging of this object might reveal a jet origin for the He I 1.083 μm emission, while higher resolution spectroscopy of the He I 1.083 μm emission will allow for analysis of intervening kinematic structures through the study of potential absorption components within the line profile. The large EW of this line in the spectrum of 2M1155−79B makes this object a strong candidate for the use of both of these methods.

3.5 Conclusions

2M1155−79B is a low-mass member of the ∼5 Myr moving group, ϵCA, and a wide separation companion (5.75", 580 AU) to another ϵCA member, 2M1155−79A. The extreme faintness and redness of 2M1155−79B in archival photometry presented the scenario that 2M1155−79B was a planet-mass object (M∼10 M_{jup}), but this is in discordance with the follow-up spectroscopy that is best matched with a M5–M6 young star standard spectrum (Fig. 3.1). The follow-up spectroscopy also shows that the spectra of 2M1155−79B and 2M1155−79A are near identical in shape, revealing that the two stars may be near-twins, with a spectral type of M5/M6. 2M1155−79B is much fainter in the optical and NIR than what is expected of this spectral type, which implies occultation of the stellar luminosity by a disk. The 2M1155−79A spectral type is in disagreement with previous optical spectral typing of M3 [66]. Follow-up optical spectroscopy of 2M1155−79B is needed to clarify the stellar properties of 2M1155−79B and verify whether it and 2M1155−79A are indeed near-twin stars.

We have presented evidence demonstrating that 2M1155−79B hosts a highly inclined circumstellar disk. Analysis of the WISE photometry for the 2M1155−79AB system (Sec 3.3.2, Fig. 3.4) demonstrates that the infrared excess originally associated with 2M1155−79A instead originates from 2M1155−79B. The SED of 2M1155−79B is ∼10–100 times fainter than 2M1155−79A throughout the optical and NIR (Figs. 3.1, 3.5). SED models of the 2M1155−79B star-disk system with MCFOST (Fig. 3.6) show that a highly inclined disk (i∼75-81°) can account for the flux difference. The He I 1.083 μm emission line observed in both nights of the FIRE spectra is indicative of ongoing accretion and potentially accretion driven winds and/or jets (see Sec 3.4.3). This places 2M1155−79B among a small subset of pre-MS, low-mass stars (as discussed in Sec 3.4.2) that are both highly obscured by edge-on disks and show signs of active accretion. Like these other, analogous systems, the 2M1155−79B system is a particularly promising subject for studies of star and planet formation around low-mass stars.

Chapter 4

A Vertical Analysis of Gas and Dust in the Disk around T Cha

4.1 Introduction

The study of protoplanetary disks has been greatly advanced over recent years due to high angular resolution imaging of both millimeter dust and molecular line emission with Atacama Large Millimeter Array (ALMA). But, as the high percentage of disks that are observed are low- to moderate-inclination systems, information about the vertical structure of millimeter grains and gas has been limited.

Archival ALMA observations of the early M-type member of the ϵ Chamaeleontis Association (~5 Myr), T Chamaeleontis (T Cha), provide an ideal opportunity for probing vertical structures of planet-forming disks. T Cha is an intermediate-mass star (K0, ~1.3 $M_{\odot}$ [89, 87]) with a gaseous CO disk that extends out to R~230 AU [12]. The disk surrounding T Cha is the nearest ($102.7^{+0.5}_{-0.4}$ pc [120]) known transition disk around a near solar-mass star viewed at a high inclination angle ($i = 67 \pm 5^{\circ}$ [12]); it is ~1.5 times closer than other, well-studied, highly inclined disks in nearby star-forming clouds, like SSTC2D J163131.2-242627 (Oph16313, [148, 149]) and 2MASS J16281370−243139 (the Flying Saucer, [44, 150]).

The dust component of T Cha disk has been the subject of many sub-mm imaging analyses (see [96, 67, 12]) and is thought to have two main disk components: an inner disk composed of smaller, sub-μm, dust particles that is detected in the near infrared (NIR) and a larger, outer disk composed of the larger dust grains that dominate the flux in the sub-mm. The warm inner dust component extends to R$\sim$0.1 AU, after which there is a gap, a region with little to no dust, until the outer disk begins at R$\sim$19 AU [96, 12]. Scattered-light observations of the disk using VLT/SPHERE have established that the gap extends to R$\sim$30 AU in the sub-mm regime [4]. The mm-wave emission extends to R$\sim$80 AU [12, 13]. The optical spectrum of the star shows signs of variable accretion onto its host along with photometric variability; the variability is most likely an effect of asymmetries within the disk and/or a misalignment between the two disk components [95, 96, 87, 151].

The gas component of this disk has been imaged with ALMA in CO(3-2), ^{13}CO(3-2) and CS(7-6), but at too low angular resolution to resolve structure within the gas [12]. The higher angular resolution archival ALMA images presented in this work are necessary to see the finer structure of the disk. Section 4.2 reviews the Cycle 2 ALMA observations of 338 GHz continuum, ^{12}CO(3-2), and ^{13}CO(3-2). In Section 4.3, we present radial and vertical profiles for the ALMA observations and a radiative transfer model (MCFOST) of the disk. In Section 4.4, we compare the model to the ALMA data and discuss the physical properties of the disk. We also present qualitative comparison of T Cha to the two aforementioned nearby, nearly edge-on disks that have been imaged in CO: Oph16313 and the Flying Saucer.

Table 4.1: Beam size, radii, and integrated intensities for T Cha

Species	Frequency GHz	Integrated Intensity^{a}	RMS Jy/beam	r_{in} "(AU)	r_{out} "(AU)
Continuum	338	0.216$\pm$0.002 Jy	1.3×10^{-4}	0.25" (25)	0.45" (50)
^{12}CO (3-2)	330.588	14.6$\pm$0.5 Jy*km s^{-1}	8.1×10^{-3}	0.14" (15)^{b}	1.85" (200)
^{13}CO (3-2)	345.796	5.9$\pm$0.9 Jy*km s^{-1}	1.0×10^{-2}	0.20" (20)^{b}	0.95" (100)

NOTE: a. Integrated intensities were found using the casaviewer tool and are therefore approximate. b. the estimates for the inner gaps should be taken as no more than upper limits since the size is at the limitations of the beam size.

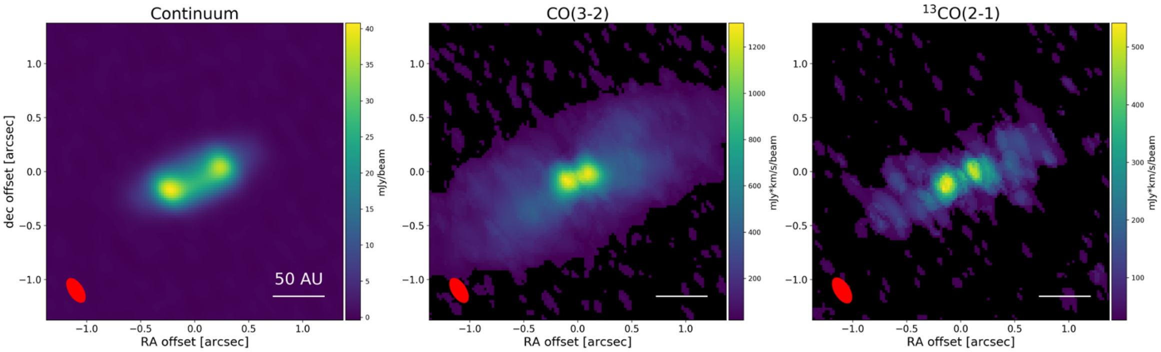

Figure 4.1: The cleaned and calibrated Cycle 2 ALMA images of the the 338 GHz continuum emission and the integrated emission map of ^{12}CO (3-2) and ^{13}CO (3-2) (from left to right). The red ellipse represents the synthesized beam for the set of images and the white line represents 50 AU (at a distance of 102.7 pc).

4.2 Data

The data used for this analysis are from the ALMA archive taken from a single ALMA program, 2012.1.00182.S (Cycle 2; PI Joanna Brown). They were obtained in ALMA band 7 spectral setup in the 12 m configuration. These observations were carried out on 2015 July 17 for a duration of 333 s with antennas in a configuration with baselines in the range of 83–606 m. The observations were optimized to include ^{12}CO (3-2), ^{13}CO (3-2), and CS (7-6) line emissions, and 338 GHz continuum. CS was a weak detection with a low signal-to-noise ratio and is not part of this analysis. The reconstructed beam was highly elliptical (0.26” × 0.14”).

The data were originally calibrated by the ALMA/NAASC staff. Subsequent data reduction and calibration was performed using the CASA 4.4.2 pipeline. The 338 GHz continuum data were previously published as part of a survey of disks in Pinilla et al. (2018) [152], although it was re-reduced for this project and different analysis performed.

4.3 Results

4.3.1 ALMA Data

Figure 4.1 displays the 3 final images from the reduction process — the 338 GHz continuum image, the ^{12}CO moment 0 (frequency-integrated intensity) image, and the ^{13}CO moment

0 image. The approximated integrated intensities are listed in Table 4.1. given the ∼10% calibration uncertainties, these ^{12}CO and ^{13}CO integrated intensities are consistent with the previous previous, lower spatial resolution, ALMA imaging (12.46±0.11 and 4.31±0.07 Jy*km s^{-1} respectively [12]) and the single-dish, APEX observations (12.7±1.2 and 7±2.1 Jy*km s^{-1}[67]).

The continuum shows two connected peaks that can be interpreted as a highly inclined, limb-brightened ring. The sub-mm and millimeter continuum ring morphology has been noted before in previous analysis of similar resolution images [12, 152] and in higher resolution imaging of the disk [13], although we see no evidence for the small inner disk observed in the 3 mm continuum at this resolution. Both the ^{12}CO and ^{13}CO moment 0 images also show a double-peaked morphology, but with a smaller inner void. Line emission from both CO isotopologues has a greater extent than the continuum. In addition to its radially extended emission, the ^{12}CO emission line also appears to be significantly more extended in the vertical direction compared to the continuum. The outer regions of the ^{12}CO disk present an X-like, or butterfly wing, morphology that extends ∼1". This morphology is also only present in ^{12}CO; ^{13}CO is less well-resolved but appears to be vertically thinner.

Emission Surface Brightness (Intensity) Profiles

From the ALMA images, we generated both radial and vertical profiles of the continuum and (velocity-integrated) CO emission line intensities. The radial profiles, presented in Fig 4.2, are extracted along the midplane of the emission of all three images. The vertical profiles, presented in Fig 4.3, are extracted at 0.000” (0 AU), 0.115” (12 AU), 0.552” (57 AU), and 0.828” (85 AU) radially from the center of the disk and reflected on both sides. In both figures the left hand panel shows where the location(s) along which the profiles were generated.

The radial intensity profiles of both CO isotoplogues and the continuum emission (Fig. 4.2) show structure similar structure to the initial morphological interpretations; all three images have shapes which can be interpreted as rings viewed at high inclination and are hence limb-brightened. Interestingly, the radial profiles reveal that both CO isotoplogues have a maximum

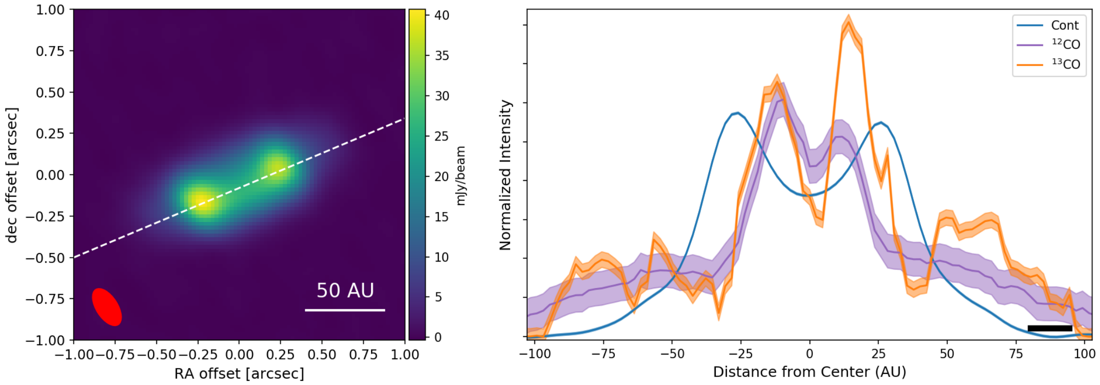

Figure 4.2: *Left:* The 338 GHz Continuum image overlaid with the placement of the radial cut in dashed white. *Right:* Normalized intensity profiles of the ^{12}CO, ^{13}CO, and 338 GHz continuum along the disk plane for T Cha in purple, orange, and blue respectively. The shaded regions above and below both CO intensity profiles are representative of the RMS noise, as obtained from off-source regions of the image. The beam size from the images in the cross-section of the midplane, and resulting shape resolution, is ∼0.14" and is marked by a black bar on the bottom right.

intensity at a smaller radius than that of the continuum (0.115" versus 0.255"), implying that a large portion of the CO gas within the disk is "nested" inside of the millimeter dust grains (see discussion in § 4.4.1). The intensity profiles along the disk plane obtained from the processed images were used to find the radii estimates presented in Table 4.1. Pinilla et al. (2018) [152] used the 338 GHz continuum data that is presented here, and through a model analysis found that the ring most probably has inner radius of ∼20 AU and an outer radius of ∼45 AU, which agrees with our values of 25 and 50 AU respectively.

Of note, the inner cavity of ^{13}CO is more pronounced than the more abundant ^{12}CO, which is likely because ^{12}CO tends to be more optically thick and the ^{13}CO comes from closer to the midplane. The ^{13}CO is less extended vertically than ^{12}CO. We estimated the vertical extent of the emission by measuring the width of the vertical profiles where the intensity approached zero. This yields a width for ^{12}CO of ∼1.2" (∼125 AU) and for ^{13}CO of ∼0.6" (∼62 AU). The profiles from the disk plane and perpendicular to the disk plane also indicate that the relative intensities of the CO isotoplogues are fairly consistent throughout the full extent of the emission from both lines.

We also utilized vertical cuts at the peak intensity of the continuum (R∼0.23", 24 AU) to

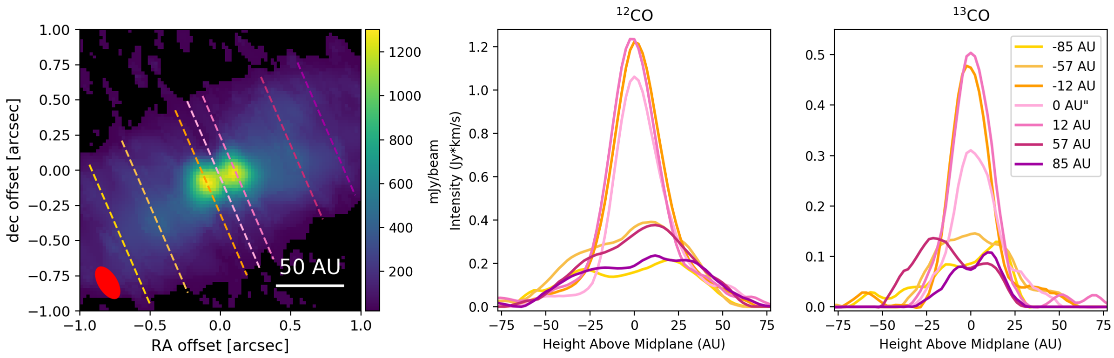

Figure 4.3: *Left:* The ^{12}CO image overlaid with the (7) positions from which vertical intensity profiles were extracted (dashed lines). The dashed lines are colored so as to match the profiles presented in the right panel. *Right:* Intensity profiles of the ^{12}CO emission along the vertical plane of the emission for T Cha. There are 7 vertical cuts mapped, defined by their distance to the radial center: 0.000" (0 AU), ±0.115" (12 AU), ±0.552" (57 AU), and ±0.828" (85 AU). The projected beam size along thise (vertical) direction is 0.27". *Middle:* Same as for the right but for ^{13}CO.

estimate its width, as described above. Figure 4.4 compares the width of both CO isotopologues at a few representative radii to this continuum profile; the vertical continuum profile width does not change with radial position. At the peak intensity of both CO isotopolgues, R∼0.115" (12 AU), the line and continuum emission appear to have similar characteristic heights within the resolution; the profiles are near identical when the intensity is normalized. The relative heights of the line and continuum emission regions then diverge at large radii, as illustrated by both the R∼0.552" (57 AU) and ∼0.828" (85 AU) cuts — there is an extended portion of the ^{12}CO emission that has a height double that of the continuum. By 85 AU, the 13CO emission appears to return to a similar characteristic vertical height as that of the continuum while the 12CO emission continues to remain vertically extended. The more vertically extended 12CO emission is most likely due to the differences in abundances between the two CO isotoplogues which translates to the 12CO being more optically thick.

4.3.2 Radiative Transfer Modelling

Previous studies have utilized the radiative transfer code MCFOST [61, 62] to model the SED of T Cha [153, 96, 12, 13], providing a good basis for our models. The stellar parameters for

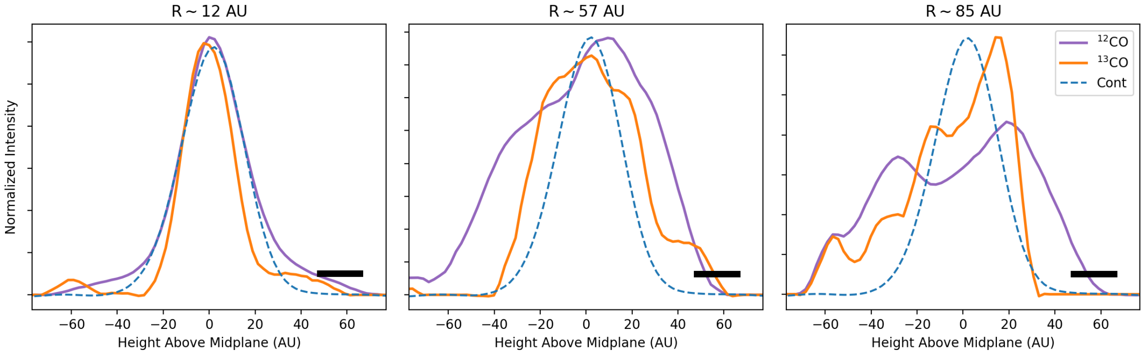

Figure 4.4: Three selected vertical intensity profiles of the ^{12}CO emission (purple) and the ^{13}CO emission (orange) of T Cha compared to a profile of peak emission vertical intensity profile of the 338 GHz continuum (blue dashed line). From left to right the selected cuts are: 0.115” (12 AU), 0.552” (57 AU), and 0.828” (85 AU). The projected beam size for this projection is 0.27” and is noted on each panel with a black bar.

T Cha ($T_* = 5250$ K, $R_* = 1.8$ $M_\odot$, and $M_* = 1.3$ $M_\odot$) are taken from Schisano et al. (2009) [87] and refs. therein following the stellar models of Baraffe et al. (2015) [31].

Following directly from Huelamo et al. (2015) [12], we began our MCFOST modelling of T Cha using two sub-disks — an inner, smaller grain ($0.01 - 1000\mu$m) disk, and an outer, slightly larger grain ($0.1 - 3000\mu$m) disk — both subdisks using silicate dust composition and a tapered exponential shape. We used a standard gas-to-dust ratio of 100 and standard CO abundance values. We used parameters from Oloffson et al. (2013) [96] for the inner disk properties, choosing the median value for all but the dust mass, for which we used the upper limit (4×10^{-11} $M_\odot$). Because the inner disk properties are more closely tied to NIR emission, we chose to keep these values constant and did not vary them during the course of the modeling.

For the outer disk, we used the parameters from Huelamo et al. (2015) [12] as a starting point before varying parameters to better match the data; the scale height (h_0) of 4 AU at 50 AU, surface density exponent (α) of -0.5, flaring exponent (β) of 1.07, an outer radius of 80 AU, PA of 113°, and dust mass of $9{\times}10^{-5}$ $M_\odot$ were kept constant. We tried a range of values for the inclination from 68 – 73° and eventually adopted a value of 73° as it best matched the optical regime of the SED (see Fig 4.5 [1]).

---

[1] The Combined Atlas of Sources with Spitzer IRS Spectra (CASSIS) is a product of the IRS instrument

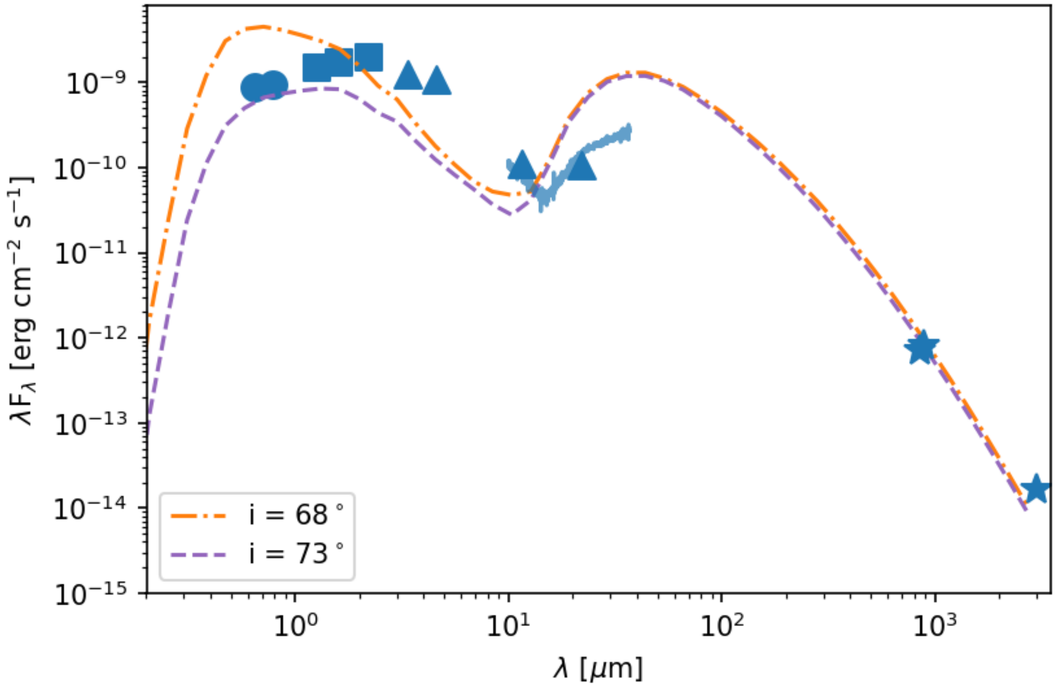

Figure 4.5: Spectral Energy Distribution of T Cha with two MCFOST generated SEDs overlaid on top for an inclination of 68° (orange dash-dot) and 73° (purple dashed). Circles represent fluxes from Gaia EDR3 (G and G$_{RP}$)[9], squares represent fluxes from 2MASS (J, H, and K) [10], triangles represent fluxes from WISE (W1, W2, W3, and W4) [11], and stars represent sub-mm/mm ALMA fluxes (this work, [12, 13]). The blue line beginning at the W4 is the IRS spectrum from T Cha retrieved from CASSIS [14].

The parameters that most heavily impacted the model in the millimeter regime were the critical radius (R_c) and the inner radius (R_{in}) of the large disk component. The critical radius is defined as the radius where the disk surface density prescription changes from a power-law to an exponential taper. We varied R_c and R_{in} from their original values from Huelamo et al. (2015) [12], 50 AU and 20 AU respectively, between ranges of 35 – 65 AU and 15 – 40 AU. The emission images produced by MCFOST were convolved by a Gaussian matching the beam size to simulate and better match the ALMA data. We also adjusted the inclination value within the literature range (as mentioned in the above paragraph) and found that for the range of

---

team, supported by NASA and JPL. CASSIS is supported by the “Programme National de Physique Stellaire” (PNPS) of CNRS/INSU co-funded by CEA and CNES and through the “Programme National Physique et Chimie du Milieu Interstellaire” (PCMI) of CNRS/INSU with INC/INP co-funded by CEA and CNES.

inclination values, the resulting beam-convolved continuum and CO emission morphologies did not vary significantly.

We present the final model SED in Fig. 4.5 and the continuum and the ^{12}CO (2-1) convolved models in Fig. 4.6. We find that an inner radius of the outer disk of $R_{in} = 25$ AU best matches the 338 GHz continuum morphology which is consistent with the inner radius we found via the radial profile. While the model CO gas morphology does appear to have an inner vacancy akin to the ALMA data, the inner radius of the model CO is larger than that which is observed. But the model does accurately reproduce the nested CO and continuum emission peaks, where the former nestles inside the latter. The best value for the critical radius is slightly smaller than the Huelamo et al. (2015) value of $R_c = 45$ AU. We found that this value best matched the slope of the decreasing intensity of the outer radii of both CO (3-2) and the continuum. Although the MCFOST parameters do match the ALMA portion of the SED fairly well, the WISE data, IRS spectrum, and 2MASS data are not matched well by this model, which would suggest that there is yet an unaccounted-for inner region of hot dust. Potentially this issue could be addressed if the mass of the inner disk was increased further from that of the Oloffson et al. (2013) [96] parameters.

While we do not accurately recreate the intensity distribution of the CO line emission, the overall shape is well recreated by the model. We see a general "butterfly" shape in both the data and the model, and the southern region (the side of the disk that is facing the earth) is seen to be enhanced in intensity relative to the north side. Both the morphology and the relative intensity of the 338 GHz continuum emission is well matched by the MCFOST model, with the limb brightened ring structure apparent in both data and model.

Model Surface Brightness (Intensity) Profiles

We generated radial and vertical profiles of the MCFOST emission images for comparison with the data. These are (model) velocity-integrated intensity profiles of line emissions. The radial profiles, as displayed in Fig. 4.7, are sampled from the midplane of the model's emission. The model continuum closely matches the data, with the main difference being that the central

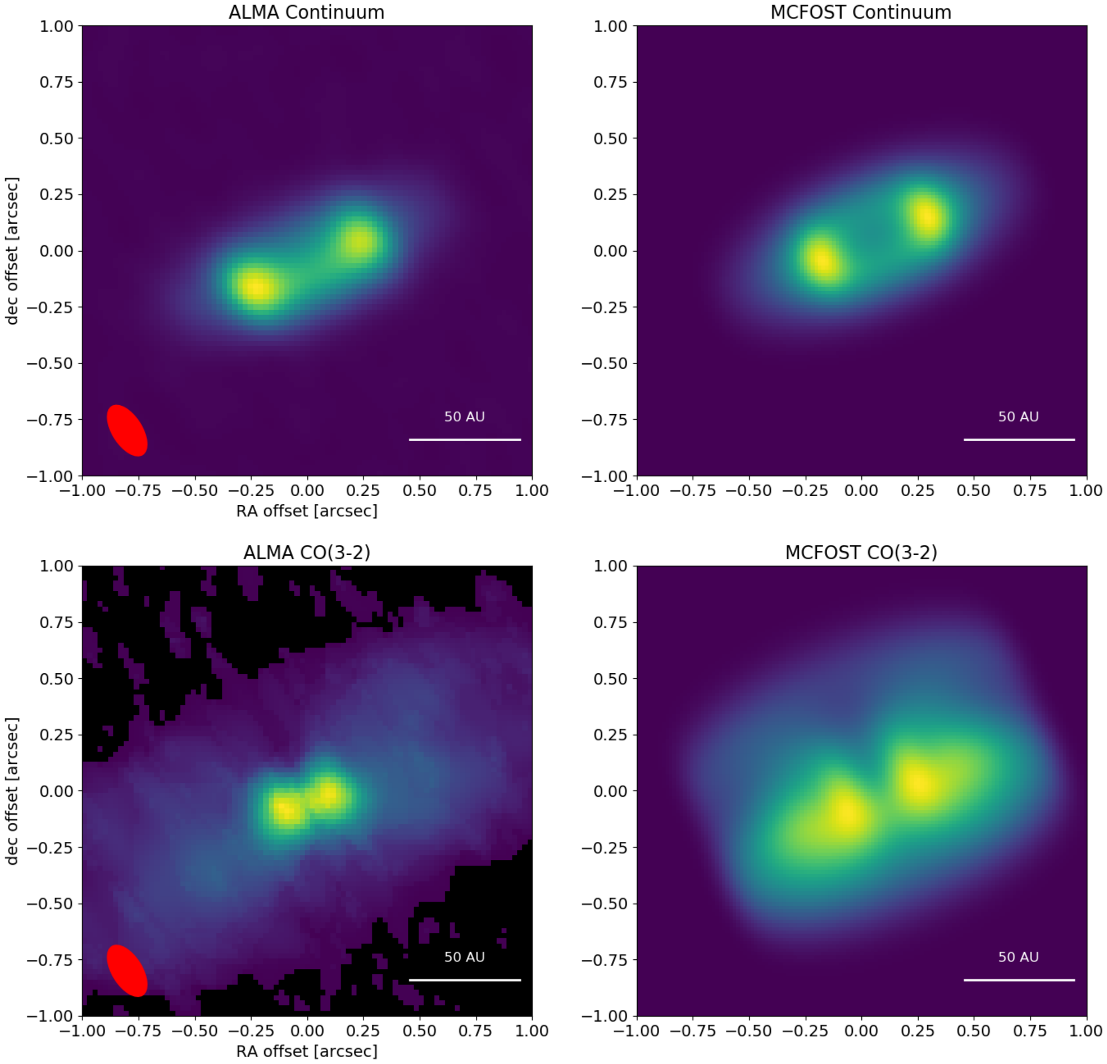

Figure 4.6: Four emission images (2”×2”) for the ALMA data and their MCFOST counterparts: ALMA 338 GHz Continuum (top left), MCFOST 338 GHz Continuum (top right), ALMA ^{12}CO (3-2) Line Emission (bottom right), and MCFOST ^{12}CO (3-2) Line Emission (bottom left). The red ellipse is representative of the ALMA beam and the white line represents 50 AU.

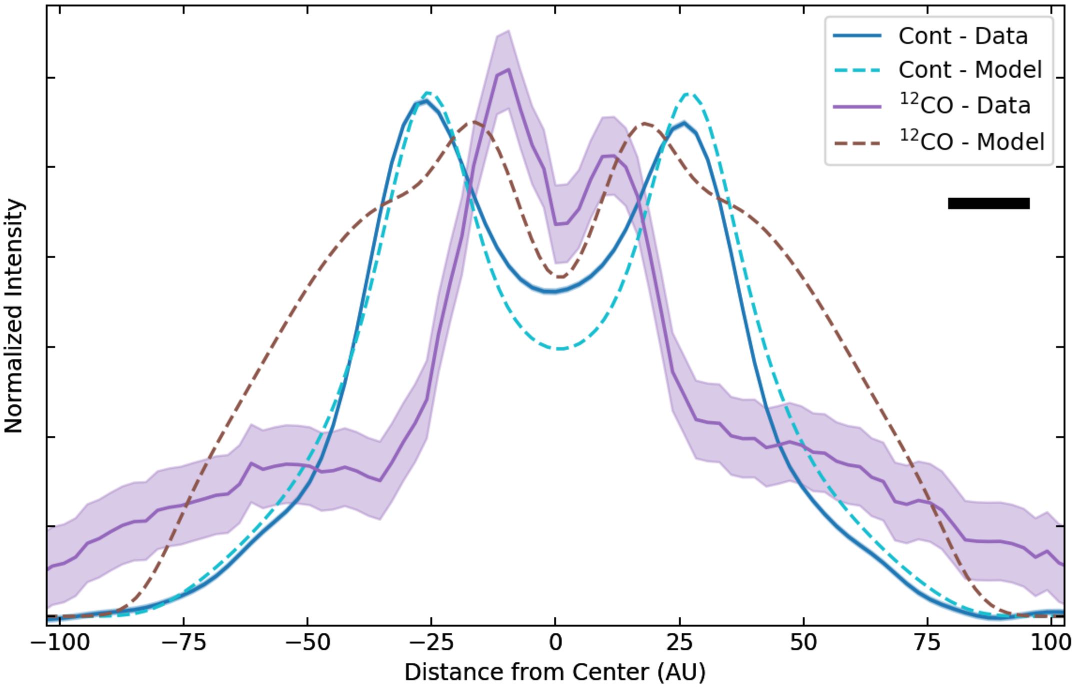

Figure 4.7: Normalized Intensity Profiles of the ^{12}CO and 338 GHz Continuum along the radial plane of the emission for T Cha, in purple and blue lines respectively, and their model counterparts, in teal and brown dashed lines. The shaded regions above and below the CO intensity profiles are representative of the RMS noise, as obtained from off-source regions of the image. The beam size from the images in the cross-section of the midplane, and resulting shape resolution, is ∼0.14" and is marked by a black bar underneath the legend in the top right.

regions of the model disk appear deficient in continuum emission relative to the data. This could be an indication that the model is missing a dust component in the inner disk that is contributing to added emission in the central regions — which could also increase the mid-IR luminosity to better match the SED. The 3 mm continuum shows a small, resolved disk near the central star which could be the unresolved component in the 338 GHz continuum that could be elevating the intensity in the central regions of the disk as observed by ALMA[13].

The ^{12}CO model is less well-matched to its data counterpart – although the total intensity is similar. The model correctly predicts the central emission cavity seen in the ALMA data with peaks that lie within the corresponding continuum peaks, reproducing the intensity of the emission peaks. But the model overestimates the radius of the CO cavity and overpredicts the CO emission surface brightness at radii beyond $\sim$25 AU until radii of $\sim$80 AU, where the model underpredicts the surface brightness compared to the extended emission region of the ALMA data. Interestingly, the location where the change in behavior occurs align with the models outer disk's inner radius, R_{in} = 25 AU, potentially meaning there is a link between these two radii (see Discussion in § 4.4.1).

The vertical profiles illustrate the difference in morphology of the model compared to the data very clearly; these profiles of the ^{12}CO (3-2) model compared to the data are presented in Fig. 4.8. While the overall heights of the model and the data are fairly similar, $\sim$0.6" (62 AU), the enhanced intensity of the inner radii of the model affects the height of the vertical profiles, especially the 12 AU vertical profile (near peak intensity). Despite having a much higher relative total intensity, both 57 AU vertical profiles for the model and data show the two-peaked structure with the maximum intensity slightly above the midplane and the second maxima below the midplane. This illustrates that the model is matching the butterfly wing effect witnessed in the data fairly well, despite problems with relative intensity.

The ^{12}CO (3-2) still has an elevated profile beyond a radii of 0.828" (85 AU), but the model equivalent ends at that radius. This is most likely due to the model generating the temperature profile of the disk via the dust grains, which has an outer radius of 80 AU, so it would follow that beyond that radius it would be too cold for CO emission. This could potentially be adjusted with adding a third disk component with MCFOST of small particles that would effect the 338 GHz continuum emission, but there is no observational evidence (beyond the extent of the CO) for its presence.

4.4 Discussion

4.4.1 Disk Morphology

We measure an inner radius for the 338 GHz thermal dust emission of 25 AU; other analyses of the millimeter continuum have found similar inner radii for the dust, ranging from 19 to 30 AU, of which our measurement sits in the center [96, 12, 13]. The disk extends to a radius of 80 AU, while the CO extends beyond 100 AU. The gas component of T Cha has a larger extant than the millimeter-emitting dust component, which is similar to many other protoplanetary disks (e.g. [154, 155]). This phenomenon is most likely caused by two processes within the disk. The first is dust evolution causing sub-mm and millimeter dust grains to decouple from the gas which causes the grains to migrate radially inwards as well to settle in the midplane. The second process is the much higher optical depth of ^{12}CO comparatively to the continuum optical depth (especially at the warm, upper layers of the disk), and therefore the detection threshold for ^{12}CO extends much farther throughout the disk radially. The ^{12}CO emission seems to be more extended than ^{13}CO — although ^{13}CO appears to have a larger inner cavity (see radii estimates in Table 4.1) — which could also be due to optical depth effects, ^{13}CO usually being the optical thinner emission line.

Noticeable at the outer radii of the ^{12}CO (3-2) velocity-integrated image is a butterfly wing effect, the x-shape. This effect is also seen in ^{12}CO another nearby edge on disk, the Flying Saucer [44]; Dutrey et al. (2017) [44] suggest that this effect is due to the CO emission being an optically thick line and is more sensitive to the warm, less dense gas that resides above the disk mid-plane. The ^{12}CO emission in the mid-plane region has a lower apparent brightness due to self-absorption by colder, intervening gas, but they suggest that since the butterfly effect is only seen along the edges of the disk, where the effect of this should be small,

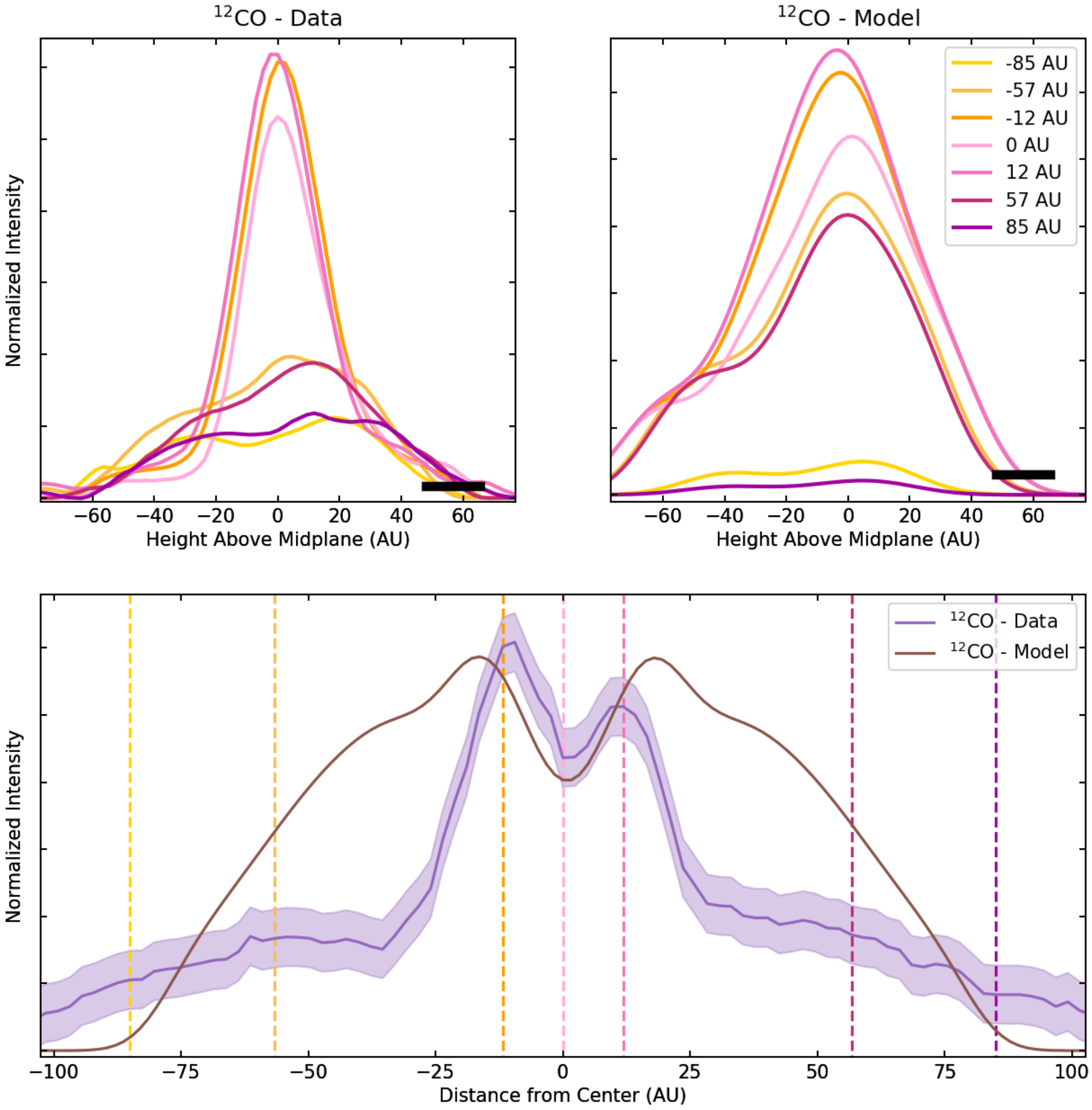

Figure 4.8: *Top:* Vertical line emission profiles of ^{12}CO (3-2) for both the ALMA data (left) and the MCFOST model (right). The projected beam size of the ALMA observations is 0.14" and is marked with a black bar in the bottom right corner of both plots. *Bottom:* Radial line emission profiles as taken from the midplane of ^{12}CO (3-2) for both the ALMA data (purple) and the MCFOST model (brown) with the locations of the vertical cuts of the top panel marked in dashed lines of the corresponding color.

that this morphology is instead effectively probing the vertical temperature gradient. It is safe to assume that since the ^{12}CO observed from T Cha is most likely also optically thick, and with the high inclination of T Cha, that this is also the most likely scenario for what is being witnessed in T Cha. This effect is not apparent in the ^{13}CO emission line because it is a less optically thick emission as well as significantly fainter due to its lower abundance.

Van Der Marel et al. (2018) [156] presented a suite of CO observations for 11 transition disks with large gas cavities. Of their sample, three disks have larger dust cavities than the cavities seen in their gas counterparts, like T Cha (Fig. 4.2). Through their modeling, they were able to conclude that for the gas cavities smaller than the dust cavities, the holes were consistent with planet-disk interaction models. These models predict that gas will be trapped at the outer edge of the dust cavity. Modelling of T Cha done by Hendler et al. (2018) [13] show that the gap witnessed in the 3 mm continuum is consistent with one large Jupiter-sized planet, or potentially multiple smaller planets, occupying that space.

Our observations support the presence of a planet (or planets) in the gap, but do not provide any more conclusive evidence of this; we were able to mostly recreate the observations with a simple two-disk model with an inner radius for the sub-mm dust at 25 AU, which coincides with the bright central region of ^{12}CO having an outer radius of 26 AU. Potentially, our issues recreating the morphology of the gas could be due to the CO morphology being enhanced by the presence of a planet and inserting a planet into the model could solve this.

4.4.2 Temperature Structure

The disk temperature information from the MCFOST modelling is displayed in Fig. 4.9. The inner disk experiences the highest temperatures (T$\sim$1000 K) while the outer disk ranges between 20–100 K. The temperature regime required for CO disk freeze out is $<$20 K which is not reached until the outermost radii of the disk, where the butterflying wing structure begins to split. This implies that the wing structure, that also appears in the modelled ^{12}CO images (Fig. 4.6), is intrinsically linked to the radii at which CO experiences freeze out in the midplane and thus the emission is isolated to the warm upper layers of the disk. More precise modelling

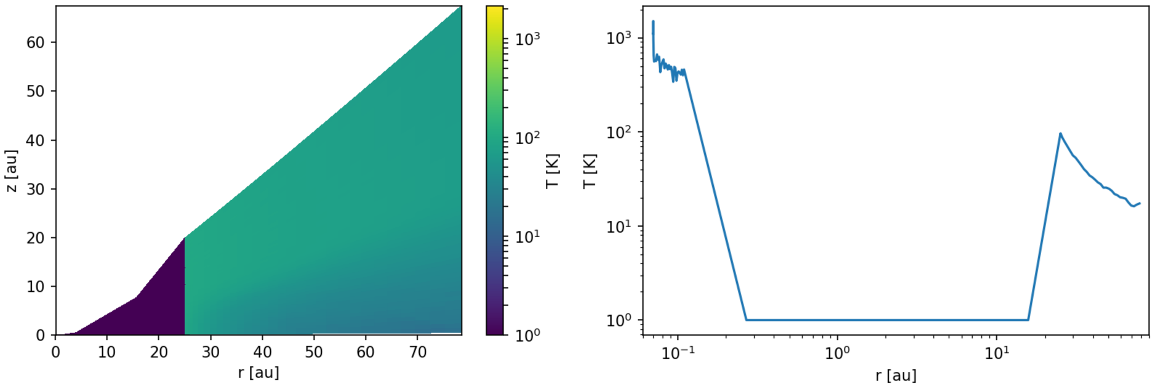

Figure 4.9: *Left:* The temperature (color bar) of the MCFOST disk model shown versus both radial (r, AU) and vertical position (z, AU). *Right:* The temperature of the MCFOST disk model averaged across the vertical height of the disk versus the radial position (in AU).

and further higher resolution imaging of the ^{12}CO emission will predict more accurately the location of the snowline, but our analysis places the radius of the midplane snowline at ∼85 AU.

4.4.3 Comparison with Other Edge-on Disks

The Flying Saucer system hosts a disk viewed nearly edge-on (i∼87°) around a low-mass (0.57 $M_\odot$) stellar object at a distance of ∼ 120 pc [157, 44, 150]. It has been imaged in sub-mm continuum, CO, CS, and CN. As mentioned in Sec 4.4.1, imaging of ^{12}CO in the Flying Saucer also shows a butterfly wing effect — in the (2-1) rotational line rather than the (3-2) rotational line — although the emission does not appear to show a central cavity. Another nearby (D∼147 pc [158]) highly-inclined (i∼84°) disk has been imaged in sub-mm continuum, ^{12}CO (2-1), and ^{13}CO (2-1) around Oph163131 [148, 149]. Again, the butterfly, or X shape, is clearly displayed in the ^{12}CO images of this system, but it also displays an additional flat outer region that extends to larger radii. The break between the two disks aligns with the outer radius of both the sub-mm continuum emission and the scattered light [148]. With the current resolution of the CO images of T Cha, it is unclear if there is an extended disk in this same manner.

4.5 Summary

We present analysis of archival Cycle 2 ALMA images of the 338 GHz continuum and the 12CO and ^{13}CO emissions from the edge-on disk around T Cha. We found inner and outer radii for all images (Table 4.1), as well as estimates of the vertical extent of the emissions. The 12CO line emission is the most extensive and illustrates a butterfly wing morphology indicative of CO freeze-out in the midplane at the outer radii of the disk (Fig 4.1). We also present radial profiles of the continuum and the CO isotoplogues which reveal that the CO is "nested" inside of the inner radius of the continuum (Fig. 4.2) – this is commonly seen in systems where there are one or more planets trapping the gas on the edges of a dusty ring.

We present MCFOST modelling of the disk around T Cha in both dust and 12CO (Fig. 4.6). We find that overall the literature properties are well matched by the ALMA data with the exception of a few parameters: i = 73°, R_{in} = 25 AU, and R_c = 45 AU. Vertical and radial emission profiles of the model emission images confirms that while the continuum is being modelled adequately, the observed 12CO emission morphology has an enhanced inner region (R∼0.25") that is not seen in the model. We do recreate the butterfly wing effect in the model and present the vertical temperature gradient this results from. We estimate the radial CO freeze-out line at 85 AU, although higher resolution imaging and more advanced modelling is needed to better probe the vertical temperature gradient.

Chapter 5

Summary and Future Work

5.1 Summary

The ϵ Cha Association (ϵCA) is not only the youngest co-eval group of stars within ~100 pc, but it also has many systems within it that are unique in their own right. The work presented in this dissertation reevaluates the NYMG with the addition of more precise parallaxes and space motions due to the Gaia mission, as well as presents the close evaluation of two young stars with edge-on disks.

Working forward from the candidate list presented by Murphy et al (2013) [63], we reassessed the membership of ϵCA using updated distances and proper motions from Gaia DR2. I present a new membership list for ϵCA that consists of 36 *bona fide* members and 20 provisional members, as well as an updated age estimate of age 5^{+3}_{-2} Myr. Using the new members, we find an updated mean distance ($D = 100.99$ pc, $\sigma_D = 4.62$ pc) and Galactic positions and velocities which can be used in future searches for new members. We identified 5 photometric binaries among the group members, 3 of which are new binary star candidates, which gives ϵCA an updated multiplicity fraction of 40%.

The additional three new ϵCA binary candidates, identified via a search of Gaia DR2 for wide-separation, co-moving companions to previously identified members, include the interesting object, 2M1155−79B, a 5.75"(~580 AU) separation companion to low-mass (M3) ϵCA member 2M1155−79A. We present NIR spectra of 2M1155−79A and B from the FIRE instrument on the Magellan telescope, which reveals that the two stars have spectra that are identical in shape, revealing that the two stars may be near-twin M5/M6 stars. Through modelling the system using MCFOST, I showed that the ∼10–100 times more fainter SED of 2M1155−79B can be accounted for by a highly inclined (i∼75-81°) disk. Analysis of the WISE photometry of the system also agrees with this and reveals that the infrared excess originally associated with 2M1155−79A instead originates from 2M1155−79B.

Using archival Cycle 2 ALMA images of 338 GHz, 12CO, and ^{13}CO emissions from the edge-on disk around T Cha and radiative transfer modelling with MCFOST, we were able to determine new constraints on the properties of the gaseous disk surrounding T Cha. I present radial profiles of the continuum and the CO isotoplogues which reveal that the CO is “nested” inside of the inner radius of the continuum (Fig. 4.2) – this is commonly seen in systems where there are one or more planets trapping the gas on the edges of a dusty ring. We find updated paramters for the disk, via MCFOST modelling, of: $i = 73°$, $R_{in} = 25$ AU, and $R_c = 45$ AU.

The two ϵCA studied in this thesis present a fraction of the potential that the NYMG has for advancing our knowledge of planet formation and protoplanetary disk morphology. They exhibit the groundwork for future studies of the many interesting star-disk systems within ϵCA — like HD 104237A and MP Mus — and future analysis comparing disk composition versus stellar mass at ∼5 Myr.

5.2 Future Work

5.2.1 High Resolution Infrared Imaging of 2M1155-79B and its Analogs

Building on my work to date on 2M1155−79B and its similarities to 2M1201−78 and TWA 30B, I am initiating a pilot observing program concentrating on nearby, edge-on disks around young M-stars that utilizes both spectra and imaging of these three systems. I have already developed and submitted HST and JWST proposals to obtain both scattered-light and emission line images (HST) as well as mid-IR spectroscopy (JWST) of all three objects.

Edge-on disks provide useful insight into fundamental disk parameters such as inclination, surface density, and dust grain size distributions and opacities which can be inferred from scattered-light disk imaging observations. Accretion and accretion-driven processes in these disks also play an important role in disk lifetimes and ongoing planet formation, which makes it important to quantify these processes. While both TWA 30B and 2M1155−79B show strong signs of active accretion, 2M1201−78 has weaker accretion signatures. This implies that the disk is potentially more evolved and has cleared out its inner most regions and is, therefore, a more evolved version of the other two systems. The narrow-band imaging of forbidden lines and Hα of these objects will establish the nature of the accretion, and potentially show accretion-driven jets from these objects. Imaging of [S II], which has been seen in the spectra of TWA 30B and 2M1201−78, will be used to to probe shocks formed by outflows.

5.2.2 Gaia DR3 and the Eps Cha Association

There is already in progress a followup EDR3 search for new ϵCA members that has yielded ~100 new candidate members including at least a dozen objects that show (Gaia /2MASS/WISE) SED evidence for dusty disks (Varga, Dickson-Vandervelde, Kastner, et al., in prep). Some of these new M-star disk candidates, as well as possible brown dwarf star/disk systems would provide a natural follow-up study to the pilot HST + JWST + Magellan study of 2M1155−79B. I will re-run my empirical isochrone analysis, the content of Chapter 2, using the updated Gaia Data Release 3 which was released in June of 2022.

5.2.3 Protoplanetary Disk Chemistry with ALMA

There is untapped potential in an ALMA disk chemistry study that exploits a population of disks that are all from the same coeval parent stellar population. Targeting a sample of coeval disks ensures any diversity seen in the disk chemistries and chemical structures would be due to differences in the physical structures of the disk (reflective of dynamical histories) and stellar irradiation exposures, as opposed to different evolutionary states (ages) or chemical inheritances (parent cloud chemistries). As a natural extension of my studies of two disks within the ϵCA, it naturally follows to continue utilizing this group with a ALMA molecular line study on four bright, gaseous disks within it that have already been imaged in the continuum and CO: T Cha, MP Mus, HD104237A, and HD104237E.

MP Mus is an analog to the nascent solar system, given its estimated stellar mass ($\sim$1.2 $M_{\odot}$), its lack of a close binary companion, and the apparent similarity of the outer radius of its molecular disk ($\sim$100 au) to that of the solar nebula ($\sim$80 au[159]). The nearest known example of a highly inclined transition disk, with spectroscopily established evidence of HCO^+, HCN, and CN [67] T Cha presents a unique opportunity to probe vertical chemical structures. HD 104237A is a Herbig Ae/Be star and the most massive component of an X-ray-luminous quintuple system that includes the fourth target, HD 104237E. It has a close (K3 type) companion and its circumbinary disk is exposed to both the bright UV from the A4 primary and X-rays from the K3 secondary. HD 104237E hosts another edge-on disk, like T Cha, that appears to have no central cavity and will provide a good contrast to the vertical chemistry seen from T Cha – i.e. a comparison of chemistries with and without a central disk cavity.

Bibliography

[1] Karin I. Öberg and Edwin A. Bergin. Astrochemistry and compositions of planetary systems. *Physics Reports*, 893:1–48, January 2021. (document), 1.1, 1.4.1, 1.4.2, 1.4.2

[2] Jonathan Gagné and Jacqueline K Faherty. BANYAN. XIII. A First Look at Nearby Young Associations with Gaia Data Release 2. *The Astrophysical Journal*, 862(2):138, 2018. (document), 1.2, 1.2.1, 2.1, 2.2, 2.4.1.4, 3.1

[3] Sean M. Andrews. Observations of Protoplanetary Disk Structures. *ARA&A*, 58:483–528, August 2020. (document), 1.3, 1.3.1, 1.4.1, 1.3, 3.1

[4] A. Pohl, E. Sissa, M. Langlois, A. Müller, C. Ginski, R. G. van Holstein, A. Vigan, D. Mesa, A. L. Maire, Th. Henning, R. Gratton, J. Olofsson, R. van Boekel, M. Benisty, B. Biller, A. Boccaletti, G. Chauvin, S. Daemgen, J. de Boer, S. Desidera, C. Dominik, A. Garufi, M. Janson, Q. Kral, F. Ménard, C. Pinte, T. Stolker, J. Szulágyi, A. Zurlo, M. Bonnefoy, A. Cheetham, M. Cudel, M. Feldt, M. Kasper, A. M. Lagrange, C. Perrot, and F. Wildi. New constraints on the disk characteristics and companion candidates around T Chamaeleontis with VLT/SPHERE. *A&A*, 605:A34, September 2017. (document), 1.4, 1.6, 4.1

[5] E. Tognelli, P. G. Prada Moroni, and S. Degl'Innocenti. Theoretical uncertainties on the radius of low- and very-low-mass stars. *MNRAS*, 476(1):27–42, May 2018. (document), 1.2, 2.1, 2.3.1, 2.3, 2.5.3, 3, 2.9

[6] Jinhee Lee and Inseok Song. Development of models for nearby young stellar moving groups: Creation, revision, and finalization of the models. *Monthly Notices of the Royal Astronomical Society*, 486(3):3434–3450, 2019. (document), 2.1, 2.7, 2.5.1, 2.5.3, 2.9

[7] K. L. Luhman, E. E. Mamajek, S. J. Shukla, and N. P. Loutrel. A Survey for New Members of the Taurus Star-forming Region with the Sloan Digital Sky Survey. *AJ*, 153(1):46, January 2017. (document), 3.1, 3.3.1

[8] David R. Rodriguez, Gerrit van der Plas, Joel H. Kastner, Adam C. Schneider, Jacqueline K. Faherty, Diego Mardones, Subhanjoy Mohanty, and David Principe. An ALMA survey for disks orbiting low-mass stars in the TW Hya Association. *A&A*, 582:L5, October 2015. (document), 1.5, 3.4.2, 3.7

[9] Gaia Collaboration, A. G. A. Brown, A. Vallenari, T. Prusti, J. H. J. de Bruijne, C. Babusiaux, M. Biermann, O. L. Creevey, D. W. Evans, L. Eyer, A. Hutton, F. Jansen, C. Jordi, S. A. Klioner, U. Lammers, L. Lindegren, X. Luri, F. Mignard, C. Panem, D. Pourbaix, S. Randich, P. Sartoretti, C. Soubiran, N. A. Walton, F. Arenou, C. A. L. Bailer-Jones, U. Bastian, M. Cropper, R. Drimmel, D. Katz, M. G. Lattanzi, F. van Leeuwen, J. Bakker, C. Cacciari, J. Castañeda, F. De Angeli, C. Ducourant, C. Fabricius, M. Fouesneau, Y. Frémat, R. Guerra, A. Guerrier, J. Guiraud, A. Jean-Antoine Piccolo, E. Masana, R. Messineo, N. Mowlavi, C. Nicolas, K. Nienartowicz, F. Pailler, P. Panuzzo, F. Riclet, W. Roux, G. M. Seabroke, R. Sordo, P. Tanga, F. Thévenin, G. Gracia-Abril, J. Portell, D. Teyssier, M. Altmann, R. Andrae, I. Bellas-Velidis, K. Benson, J. Berthier, R. Blomme, E. Brugaletta, P. W. Burgess, G. Busso, B. Carry, A. Cellino, N. Cheek, G. Clementini, Y. Damerdji, M. Davidson, L. Delchambre, A. Dell'Oro, J. Fernández-Hernández, L. Galluccio, P. García-Lario, M. Garcia-Reinaldos, J. González-Núñez, E. Gosset, R. Haigron, J. L. Halbwachs, N. C. Hambly, D. L. Harrison, D. Hatzidimitriou, U. Heiter, J. Hernández, D. Hestroffer, S. T. Hodgkin, B. Holl, K. Janßen, G. Jevardat de Fombelle, S. Jordan, A. Krone-Martins, A. C. Lanzafame, W. Löffler, A. Lorca, M. Manteiga, O. Marchal, P. M. Marrese, A. Moitinho, A. Mora, K. Muinonen, P. Os-

borne, E. Pancino, T. Pauwels, J. M. Petit, A. Recio-Blanco, P. J. Richards, M. Riello, L. Rimoldini, A. C. Robin, T. Roegiers, J. Rybizki, L. M. Sarro, C. Siopis, M. Smith, A. Sozzetti, A. Ulla, E. Utrilla, M. van Leeuwen, W. van Reeven, U. Abbas, A. Abreu Aramburu, S. Accart, C. Aerts, J. J. Aguado, M. Ajaj, G. Altavilla, M. A. Álvarez, J. Álvarez Cid-Fuentes, J. Alves, R. I. Anderson, E. Anglada Varela, T. Antoja, M. Audard, D. Baines, S. G. Baker, L. Balaguer-Núñez, E. Balbinot, Z. Balog, C. Barache, D. Barbato, M. Barros, M. A. Barstow, S. Bartolomé, J. L. Bassilana, N. Bauchet, A. Baudesson-Stella, U. Becciani, M. Bellazzini, M. Bernet, S. Bertone, L. Bianchi, S. Blanco-Cuaresma, T. Boch, A. Bombrun, D. Bossini, S. Bouquillon, A. Bragaglia, L. Bramante, E. Breedt, A. Bressan, N. Brouillet, B. Bucciarelli, A. Burlacu, D. Busonero, A. G. Butkevich, R. Buzzi, E. Caffau, R. Cancelliere, H. Cánovas, T. Cantat-Gaudin, R. Carballo, T. Carlucci, M. I. Carnerero, J. M. Carrasco, L. Casamiquela, M. Castellani, A. Castro-Ginard, P. Castro Sampol, L. Chaoul, P. Charlot, L. Chemin, A. Chiavassa, M. R. L. Cioni, G. Comoretto, W. J. Cooper, T. Cornez, S. Cowell, F. Crifo, M. Crosta, C. Crowley, C. Dafonte, A. Dapergolas, M. David, P. David, P. de Laverny, F. De Luise, R. De March, J. De Ridder, R. de Souza, P. de Teodoro, A. de Torres, E. F. del Peloso, E. del Pozo, M. Delbo, A. Delgado, H. E. Delgado, J. B. Delisle, P. Di Matteo, S. Diakite, C. Diener, E. Distefano, C. Dolding, D. Eappachen, B. Edvardsson, H. Enke, P. Esquej, C. Fabre, M. Fabrizio, S. Faigler, G. Fedorets, P. Fernique, A. Fienga, F. Figueras, C. Fouron, F. Fragkoudi, E. Fraile, F. Franke, M. Gai, D. Garabato, A. Garcia-Gutierrez, M. García-Torres, A. Garofalo, P. Gavras, E. Gerlach, R. Geyer, P. Giacobbe, G. Gilmore, S. Girona, G. Giuffrida, R. Gomel, A. Gomez, I. Gonzalez-Santamaria, J. J. González-Vidal, M. Granvik, R. Gutiérrez-Sánchez, L. P. Guy, M. Hauser, M. Haywood, A. Helmi, S. L. Hidalgo, T. Hilger, N. Hładczuk, D. Hobbs, G. Holland, H. E. Huckle, G. Jasniewicz, P. G. Jonker, J. Juaristi Campillo, F. Julbe, L. Karbevska, P. Kervella, S. Khanna, A. Kochoska, M. Kontizas, G. Kordopatis, A. J. Korn, Z. Kostrzewa-Rutkowska, K. Kruszyńska, S. Lambert, A. F. Lanza, Y. Lasne, J. F. Le Campion, Y. Le Fustec, Y. Lebreton, T. Lebzelter, S. Leccia,

N. Leclerc, I. Lecoeur-Taibi, S. Liao, E. Licata, E. P. Lindstrøm, T. A. Lister, E. Livanou, A. Lobel, P. Madrero Pardo, S. Managau, R. G. Mann, J. M. Marchant, M. Marconi, M. M. S. Marcos Santos, S. Marinoni, F. Marocco, D. J. Marshall, L. Martin Polo, J. M. Martín-Fleitas, A. Masip, D. Massari, A. Mastrobuono-Battisti, T. Mazeh, P. J. McMillan, S. Messina, D. Michalik, N. R. Millar, A. Mints, D. Molina, R. Molinaro, L. Molnár, P. Montegriffo, R. Mor, R. Morbidelli, T. Morel, D. Morris, A. F. Mulone, D. Munoz, T. Muraveva, C. P. Murphy, I. Musella, L. Noval, C. Ordénovic, G. Orrù, J. Osinde, C. Pagani, I. Pagano, L. Palaversa, P. A. Palicio, A. Panahi, M. Pawlak, X. Peñalosa Esteller, A. Penttilä, A. M. Piersimoni, F. X. Pineau, E. Plachy, G. Plum, E. Poggio, E. Poretti, E. Poujoulet, A. Prša, L. Pulone, E. Racero, S. Ragaini, M. Rainer, C. M. Raiteri, N. Rambaux, P. Ramos, M. Ramos-Lerate, P. Re Fiorentin, S. Regibo, C. Reylé, V. Ripepi, A. Riva, G. Rixon, N. Robichon, C. Robin, M. Roelens, L. Rohrbasser, M. Romero-Gómez, N. Rowell, F. Royer, K. A. Rybicki, G. Sadowski, A. Sagristà Sellés, J. Sahlmann, J. Salgado, E. Salguero, N. Samaras, V. Sanchez Gimenez, N. Sanna, R. Santoveña, M. Sarasso, M. Schultheis, E. Sciacca, M. Segol, J. C. Segovia, D. Ségransan, D. Semeux, S. Shahaf, H. I. Siddiqui, A. Siebert, L. Siltala, E. Slezak, R. L. Smart, E. Solano, F. Solitro, D. Souami, J. Souchay, A. Spagna, F. Spoto, I. A. Steele, H. Steidelmüller, C. A. Stephenson, M. Süveges, L. Szabados, E. Szegedi-Elek, F. Taris, G. Tauran, M. B. Taylor, R. Teixeira, W. Thuillot, N. Tonello, F. Torra, J. Torra, C. Turon, N. Unger, M. Vaillant, E. van Dillen, O. Vanel, A. Vecchiato, Y. Viala, D. Vicente, S. Voutsinas, M. Weiler, T. Wevers, Ł. Wyrzykowski, A. Yoldas, P. Yvard, H. Zhao, J. Zorec, S. Zucker, C. Zurbach, and T. Zwitter. Gaia Early Data Release 3. Summary of the contents and survey properties. *A&A*, 649:A1, May 2021. (document), 1.2.1, 3.3.3, 4.5

[10] M. F. Skrutskie, R. M. Cutri, R. Stiening, M. D. Weinberg, S. Schneider, J. M. Carpenter, C. Beichman, R. Capps, T. Chester, J. Elias, J. Huchra, J. Liebert, C. Lonsdale, D. G. Monet, S. Price, P. Seitzer, T. Jarrett, J. D. Kirkpatrick, J. E. Gizis, E. Howard, T. Evans, J. Fowler, L. Fullmer, R. Hurt, R. Light, E. L. Kopan, K. A. Marsh, H. L.

McCallon, R. Tam, S. Van Dyk, and S. Wheelock. The Two Micron All Sky Survey (2MASS). *AJ*, 131(2):1163–1183, Feb 2006. (document), 2.4.1.5, 3.3.3, 4.5

[11] Edward L. Wright, Peter R. M. Eisenhardt, Amy K. Mainzer, Michael E. Ressler, Roc M. Cutri, Thomas Jarrett, J. Davy Kirkpatrick, Deborah Padgett, Robert S. McMillan, Michael Skrutskie, S. A. Stanford, Martin Cohen, Russell G. Walker, John C. Mather, David Leisawitz, III Gautier, Thomas N., Ian McLean, Dominic Benford, Carol J. Lonsdale, Andrew Blain, Bryan Mendez, William R. Irace, Valerie Duval, Fengchuan Liu, Don Royer, Ingolf Heinrichsen, Joan Howard, Mark Shannon, Martha Kendall, Amy L. Walsh, Mark Larsen, Joel G. Cardon, Scott Schick, Mark Schwalm, Mohamed Abid, Beth Fabinsky, Larry Naes, and Chao-Wei Tsai. The Wide-field Infrared Survey Explorer (WISE): Mission Description and Initial On-orbit Performance. *AJ*, 140(6):1868–1881, December 2010. (document), 3.3.3, 4.5

[12] N. Huélamo, I. de Gregorio-Monsalvo, E. Macias, C. Pinte, M. Ireland, P. Tuthill, and S. Lacour. High-resolution observations of the outer disk around T Chamaeleontis: the view from ALMA. *A&A*, 575:L5, March 2015. (document), 1.6, 4.1, 4.3.1, 4.3.2, 4.5, 4.4.1

[13] Nathanial P. Hendler, Paola Pinilla, Ilaria Pascucci, Adriana Pohl, Gijs Mulders, Thomas Henning, Ruobing Dong, Cathie Clarke, James Owen, and David Hollenbach. A likely planet-induced gap in the disc around T Cha. *MNRAS*, 475(1):L62–L66, March 2018. (document), 2.1, 2.4.1.3, 4.1, 4.3.1, 4.3.2, 4.5, 4.3.2, 4.4.1

[14] V. Lebouteiller, D. J. Barry, H. W. W. Spoon, J. Bernard-Salas, G. C. Sloan, J. R. Houck, and D. W. Weedman. CASSIS: The Cornell Atlas of Spitzer/Infrared Spectrograph Sources. *ApJ Supplements*, 196(1):8, September 2011. (document), 4.5

[15] A. Wolszczan and D. A. Frail. A planetary system around the millisecond pulsar PSR1257 + 12. *Nature*, 355(6356):145–147, January 1992. 1

[16] Michel Mayor and Didier Queloz. A Jupiter-mass companion to a solar-type star. *Nature*, 378(6555):355–359, November 1995. 1

[17] Courtney D. Dressing and David Charbonneau. The Occurrence Rate of Small Planets around Small Stars. *ApJ*, 767(1):95, April 2013. 1

[18] A. Sozzetti, P. Giacobbe, M. G. Lattanzi, G. Micela, R. Morbidelli, and G. Tinetti. Astrometric detection of giant planets around nearby M dwarfs: the Gaia potential. *MNRAS*, 437(1):497–509, January 2014. 1

[19] Abraham Loeb, Rafael A. Batista, and David Sloan. Relative likelihood for life as a function of cosmic time. *JCAP*, 2016(8):040, August 2016. 1

[20] Ravi Kumar Kopparapu, Ramses M. Ramirez, James SchottelKotte, James F. Kasting, Shawn Domagal-Goldman, and Vincent Eymet. Habitable Zones around Main-sequence Stars: Dependence on Planetary Mass. *ApJL*, 787(2):L29, June 2014. 1

[21] Courtney D. Dressing and David Charbonneau. The Occurrence of Potentially Habitable Planets Orbiting M Dwarfs Estimated from the Full Kepler Dataset and an Empirical Measurement of the Detection Sensitivity. *ApJ*, 807(1):45, July 2015. 1

[22] Savita Mathur, Daniel Huber, Natalie M. Batalha, David R. Ciardi, Fabienne A. Bastien, Allyson Bieryla, Lars A. Buchhave, William D. Cochran, Michael Endl, Gilbert A. Esquerdo, Elise Furlan, Andrew Howard, Steve B. Howell, Howard Isaacson, David W. Latham, Phillip J. MacQueen, and David R. Silva. Revised Stellar Properties of Kepler Targets for the Q1-17 (DR25) Transit Detection Run. *ApJS*, 229(2):30, April 2017. 1

[23] Christopher F. McKee and Eve C. Ostriker. Theory of Star Formation. *ARA&A*, 45(1):565–687, September 2007. 1.1

[24] Kevin L. Luhman. The Formation and Early Evolution of Low-Mass Stars and Brown Dwarfs. *ARA&A*, 50:65–106, September 2012. 1.1

[25] Hans Zinnecker and Harold W. Yorke. Toward Understanding Massive Star Formation. *ARA&A*, 45(1):481–563, September 2007. 1.1

[26] Richard B. Larson. Numerical calculations of the dynamics of collapsing proto-star. *MNRAS*, 145:271, January 1969. 1.1

[27] Charles J. Lada and Elizabeth A. Lada. Embedded Clusters in Molecular Clouds. *ARA&A*, 41:57–115, January 2003. 1.1

[28] Z. Y. Li, R. Banerjee, R. E. Pudritz, J. K. Jørgensen, H. Shang, R. Krasnopolsky, and A. Maury. The Earliest Stages of Star and Planet Formation: Core Collapse, and the Formation of Disks and Outflows. In Henrik Beuther, Ralf S. Klessen, Cornelis P. Dullemond, and Thomas Henning, editors, *Protostars and Planets VI*, page 173, January 2014. 1.1

[29] B. Zuckerman and Inseok Song. Young Stars Near the Sun. *ARA&A*, 42(1):685–721, September 2004. 1.2

[30] Adric R. Riedel, Victoria DiTomasso, Emily L. Rice, Munazza K. Alam, Ellianna Abrahams, James Crook, Kelle L. Cruz, and Jacqueline K. Faherty. Radial Velocities, Space Motions, and Nearby Young Moving Group Memberships of Eleven Candidate Young Brown Dwarfs. *AJ*, 157(6):247, June 2019. 1.2

[31] Isabelle Baraffe, Derek Homeier, France Allard, and Gilles Chabrier. New evolutionary models for pre-main sequence and main sequence low-mass stars down to the hydrogen-burning limit. *A&A*, 577:A42, May 2015. 1.2, 3.4.1, 3.4.3, 4.3.2

[32] C. A. O. Torres, G. R. Quast, C. H. F. Melo, and M. F. Sterzik. *Young Nearby Loose Associations*, volume 5, page 757. Astronomical Society of the Pacific, 2008. 1.2, 2.4.1.3

[33] Gaia Collaboration, T. Prusti, J. H. J. de Bruijne, A. G. A. Brown, A. Vallenari, C. Babusiaux, C. A. L. Bailer-Jones, U. Bastian, M. Biermann, D. W. Evans, L. Eyer, F. Jansen, C. Jordi, S. A. Klioner, U. Lammers, L. Lindegren, X. Luri, F. Mignard, D. J. Milligan, C. Panem, V. Poinsignon, D. Pourbaix, S. Randich, G. Sarri, P. Sartoretti, H. I. Siddiqui, C. Soubiran, V. Valette, F. van Leeuwen, N. A. Walton, C. Aerts, F. Arenou, M. Cropper, R. Drimmel, E. Høg, D. Katz, M. G. Lattanzi, W. O'Mullane, E. K. Grebel,

A. D. Holland, C. Huc, X. Passot, L. Bramante, C. Cacciari, J. Castañeda, L. Chaoul, N. Cheek, F. De Angeli, C. Fabricius, R. Guerra, J. Hernández, A. Jean-Antoine-Piccolo, E. Masana, R. Messineo, N. Mowlavi, K. Nienartowicz, D. Ordóñez-Blanco, P. Panuzzo, J. Portell, P. J. Richards, M. Riello, G. M. Seabroke, P. Tanga, F. Thévenin, J. Torra, S. G. Els, G. Gracia-Abril, G. Comoretto, M. Garcia-Reinaldos, T. Lock, E. Mercier, M. Altmann, R. Andrae, T. L. Astraatmadja, I. Bellas-Velidis, K. Benson, J. Berthier, R. Blomme, G. Busso, B. Carry, A. Cellino, G. Clementini, S. Cowell, O. Creevey, J. Cuypers, M. Davidson, J. De Ridder, A. de Torres, L. Delchambre, A. Dell'Oro, C. Ducourant, Y. Frémat, M. García-Torres, E. Gosset, J. L. Halbwachs, N. C. Hambly, D. L. Harrison, M. Hauser, D. Hestroffer, S. T. Hodgkin, H. E. Huckle, A. Hutton, G. Jasniewicz, S. Jordan, M. Kontizas, A. J. Korn, A. C. Lanzafame, M. Manteiga, A. Moitinho, K. Muinonen, J. Osinde, E. Pancino, T. Pauwels, J. M. Petit, A. Recio-Blanco, A. C. Robin, L. M. Sarro, C. Siopis, M. Smith, K. W. Smith, A. Sozzetti, W. Thuillot, W. van Reeven, Y. Viala, U. Abbas, A. Abreu Aramburu, S. Accart, J. J. Aguado, P. M. Allan, W. Allasia, G. Altavilla, M. A. Álvarez, J. Alves, R. I. Anderson, A. H. Andrei, E. Anglada Varela, E. Antiche, T. Antoja, S. Antón, B. Arcay, A. Atzei, L. Ayache, N. Bach, S. G. Baker, L. Balaguer-Núñez, C. Barache, C. Barata, A. Barbier, F. Barblan, M. Baroni, D. Barrado y Navascués, M. Barros, M. A. Barstow, U. Becciani, M. Bellazzini, G. Bellei, A. Bello García, V. Belokurov, P. Bendjoya, A. Berihuete, L. Bianchi, O. Bienaymé, F. Billebaud, N. Blagorodnova, S. Blanco-Cuaresma, T. Boch, A. Bombrun, R. Borrachero, S. Bouquillon, G. Bourda, H. Bouy, A. Bragaglia, M. A. Breddels, N. Brouillet, T. Brüsemeister, B. Bucciarelli, F. Budnik, P. Burgess, R. Burgon, A. Burlacu, D. Busonero, R. Buzzi, E. Caffau, J. Cambras, H. Campbell, R. Cancelliere, T. Cantat-Gaudin, T. Carlucci, J. M. Carrasco, M. Castellani, P. Charlot, J. Charnas, P. Charvet, F. Chassat, A. Chiavassa, M. Clotet, G. Cocozza, R. S. Collins, P. Collins, G. Costigan, F. Crifo, N. J. G. Cross, M. Crosta, C. Crowley, C. Dafonte, Y. Damerdji, A. Dapergolas, P. David, M. David, P. De Cat, F. de Felice, P. de Laverny, F. De Luise, R. De March, D. de Martino, R. de Souza, J. Debosscher, E. del Pozo,

M. Delbo, A. Delgado, H. E. Delgado, F. di Marco, P. Di Matteo, S. Diakite, E. Distefano, C. Dolding, S. Dos Anjos, P. Drazinos, J. Durán, Y. Dzigan, E. Ecale, B. Edvardsson, H. Enke, M. Erdmann, D. Escolar, M. Espina, N. W. Evans, G. Eynard Bontemps, C. Fabre, M. Fabrizio, S. Faigler, A. J. Falcão, M. Farràs Casas, F. Faye, L. Federici, G. Fedorets, J. Fernández-Hernández, P. Fernique, A. Fienga, F. Figueras, F. Filippi, K. Findeisen, A. Fonti, M. Fouesneau, E. Fraile, M. Fraser, J. Fuchs, R. Furnell, M. Gai, S. Galleti, L. Galluccio, D. Garabato, F. García-Sedano, P. Garé, A. Garofalo, N. Garralda, P. Gavras, J. Gerssen, R. Geyer, G. Gilmore, S. Girona, G. Giuffrida, M. Gomes, A. González-Marcos, J. González-Núñez, J. J. González-Vidal, M. Granvik, A. Guerrier, P. Guillout, J. Guiraud, A. Gúrpide, R. Gutiérrez-Sánchez, L. P. Guy, R. Haigron, D. Hatzidimitriou, M. Haywood, U. Heiter, A. Helmi, D. Hobbs, W. Hofmann, B. Holl, G. Holland , J. A. S. Hunt, A. Hypki, V. Icardi, M. Irwin, G. Jevardat de Fombelle, P. Jofré, P. G. Jonker, A. Jorissen, F. Julbe, A. Karampelas, A. Kochoska, R. Kohley, K. Kolenberg, E. Kontizas, S. E. Koposov, G. Kordopatis, P. Koubsky, A. Kowalczyk, A. Krone-Martins, M. Kudryashova, I. Kull, R. K. Bachchan, F. Lacoste-Seris, A. F. Lanza, J. B. Lavigne, C. Le Poncin-Lafitte, Y. Lebreton, T. Lebzelter, S. Leccia, N. Leclerc, I. Lecoeur-Taibi, V. Lemaitre, H. Lenhardt, F. Leroux, S. Liao, E. Licata, H. E. P. Lindstrøm, T. A. Lister, E. Livanou, A. Lobel, W. Löffler, M. López, A. Lopez-Lozano, D. Lorenz, T. Loureiro, I. MacDonald, T. Magalhães Fernandes, S. Managau, R. G. Mann, G. Mantelet, O. Marchal, J. M. Marchant, M. Marconi, J. Marie, S. Marinoni, P. M. Marrese, G. Marschalkó, D. J. Marshall, J. M. Martín-Fleitas, M. Martino, N. Mary, G. Matijevič, T. Mazeh, P. J. McMillan, S. Messina, A. Mestre, D. Michalik, N. R. Millar, B. M. H. Miranda, D. Molina, R. Molinaro, M. Molinaro, L. Molnár, M. Moniez, P. Montegriffo, D. Monteiro, R. Mor, A. Mora, R. Morbidelli, T. Morel, S. Morgenthaler, T. Morley, D. Morris, A. F. Mulone, T. Muraveva, I. Musella, J. Narbonne, G. Nelemans, L. Nicastro, L. Noval, C. Ordénovic, J. Ordieres-Meré, P. Osborne, C. Pagani, I. Pagano, F. Pailler, H. Palacin, L. Palaversa, P. Parsons, T. Paulsen, M. Pecoraro, R. Pedrosa, H. Pentikäinen, J. Pereira, B. Pichon, A. M. Piersimoni, F. X. Pineau,

E. Plachy, G. Plum, E. Poujoulet, A. Prša, L. Pulone, S. Ragaini, S. Rago, N. Rambaux, M. Ramos-Lerate, P. Ranalli, G. Rauw, A. Read, S. Regibo, F. Renk, C. Reylé, R. A. Ribeiro, L. Rimoldini, V. Ripepi, A. Riva, G. Rixon, M. Roelens, M. Romero-Gómez, N. Rowell, F. Royer, A. Rudolph, L. Ruiz-Dern, G. Sadowski, T. Sagristà Sellés, J. Sahlmann, J. Salgado, E. Salguero, M. Sarasso, H. Savietto, A. Schnorhk, M. Schultheis, E. Sciacca, M. Segol, J. C. Segovia, D. Segransan, E. Serpell, I. C. Shih, R. Smareglia, R. L. Smart, C. Smith, E. Solano, F. Solitro, R. Sordo, S. Soria Nieto, J. Souchay, A. Spagna, F. Spoto, U. Stampa, I. A. Steele, H. Steidelmüller, C. A. Stephenson, H. Stoev, F. F. Suess, M. Süveges, J. Surdej, L. Szabados, E. Szegedi-Elek, D. Tapiador, F. Taris, G. Tauran, M. B. Taylor, R. Teixeira, D. Terrett, B. Tingley, S. C. Trager, C. Turon, A. Ulla, E. Utrilla, G. Valentini, A. van Elteren, E. Van Hemelryck, M. van Leeuwen, M. Varadi, A. Vecchiato, J. Veljanoski, T. Via, D. Vicente, S. Vogt, H. Voss, V. Votruba, S. Voutsinas, G. Walmsley, M. Weiler, K. Weingrill, D. Werner, T. Wevers, G. Whitehead, Ł. Wyrzykowski, A. Yoldas, M. Žerjal, S. Zucker, C. Zurbach, T. Zwitter, A. Alecu, M. Allen, C. Allende Prieto, A. Amorim, G. Anglada-Escudé, V. Arsenijevic, S. Azaz, P. Balm, M. Beck, H. H. Bernstein, L. Bigot, A. Bijaoui, C. Blasco, M. Bonfigli, G. Bono, S. Boudreault, A. Bressan, S. Brown, P. M. Brunet, P. Bunclark, R. Buonanno, A. G. Butkevich, C. Carret, C. Carrion, L. Chemin, F. Chéreau, L. Corcione, E. Darmigny, K. S. de Boer, P. de Teodoro, P. T. de Zeeuw, C. Delle Luche, C. D. Domingues, P. Dubath, F. Fodor, B. Frézouls, A. Fries, D. Fustes, D. Fyfe, E. Gallardo, J. Gallegos, D. Gardiol, M. Gebran, A. Gomboc, A. Gómez, E. Grux, A. Gueguen, A. Heyrovsky, J. Hoar, G. Iannicola, Y. Isasi Parache, A. M. Janotto, E. Joliet, A. Jonckheere, R. Keil, D. W. Kim, P. Klagyivik, J. Klar, J. Knude, O. Kochukhov, I. Kolka, J. Kos, A. Kutka, V. Lainey, D. LeBouquin, C. Liu, D. Loreggia, V. V. Makarov, M. G. Marseille, C. Martayan, O. Martinez-Rubi, B. Massart, F. Meynadier, S. Mignot, U. Munari, A. T. Nguyen, T. Nordlander, P. Ocvirk, K. S. O'Flaherty, A. Olias Sanz, P. Ortiz, J. Osorio, D. Oszkiewicz, A. Ouzounis, M. Palmer, P. Park, E. Pasquato, C. Peltzer, J. Peralta, F. Péturaud, T. Pieniluoma, E. Pigozzi,

J. Poels, G. Prat, T. Prod'homme, F. Raison, J. M. Rebordao, D. Risquez, B. Rocca-Volmerange, S. Rosen, M. I. Ruiz-Fuertes, F. Russo, S. Sembay, I. Serraller Vizcaino, A. Short, A. Siebert, H. Silva, D. Sinachopoulos, E. Slezak, M. Soffel, D. Sosnowska, V. Straižys, M. ter Linden, D. Terrell, S. Theil, C. Tiede, L. Troisi, P. Tsalmantza, D. Tur, M. Vaccari, F. Vachier, P. Valles, W. Van Hamme, L. Veltz, J. Virtanen, J. M. Wallut, R. Wichmann, M. I. Wilkinson, H. Ziaeepour, and S. Zschocke. The Gaia mission. *A&A*, 595:A1, Nov 2016. 1.2.1, 2.1, 3.1

[34] Gaia Collaboration, A. G. A. Brown, A. Vallenari, T. Prusti, J. H. J. de Bruijne, C. Babusiaux, C. A. L. Bailer-Jones, M. Biermann, D. W. Evans, L. Eyer, F. Jansen, C. Jordi, S. A. Klioner, U. Lammers, L. Lindegren, X. Luri, F. Mignard, C. Panem, D. Pourbaix, S. Randich, P. Sartoretti, H. I. Siddiqui, C. Soubiran, F. van Leeuwen, N. A. Walton, F. Arenou, U. Bastian, M. Cropper, R. Drimmel, D. Katz, M. G. Lattanzi, J. Bakker, C. Cacciari, J. Castañeda, L. Chaoul, N. Cheek, F. De Angeli, C. Fabricius, R. Guerra, B. Holl, E. Masana, R. Messineo, N. Mowlavi, K. Nienartowicz, P. Panuzzo, J. Portell, M. Riello, G. M. Seabroke, P. Tanga, F. Thévenin, G. Gracia-Abril, G. Comoretto, M. Garcia-Reinaldos, D. Teyssier, M. Altmann, R. Andrae, M. Audard, I. Bellas-Velidis, K. Benson, J. Berthier, R. Blomme, P. Burgess, G. Busso, B. Carry, A. Cellino, G. Clementini, M. Clotet, O. Creevey, M. Davidson, J. De Ridder, L. Delchambre, A. Dell'Oro, C. Ducourant, J. Fernández-Hernández, M. Fouesneau, Y. Frémat, L. Galluccio, M. García-Torres, J. González-Núñez, J. J. González-Vidal, E. Gosset, L. P. Guy, J. L. Halbwachs, N. C. Hambly, D. L. Harrison, J. Hernández, D. Hestroffer, S. T. Hodgkin, A. Hutton, G. Jasniewicz, A. Jean-Antoine-Piccolo, S. Jordan, A. J. Korn, A. Krone-Martins, A. C. Lanzafame, T. Lebzelter, W. Löffler, M. Manteiga, P. M. Marrese, J. M. Martín-Fleitas, A. Moitinho, A. Mora, K. Muinonen, J. Osinde, E. Pancino, T. Pauwels, J. M. Petit, A. Recio-Blanco, P. J. Richards, L. Rimoldini, A. C. Robin, L. M. Sarro, C. Siopis, M. Smith, A. Sozzetti, M. Süveges, J. Torra, W. van Reeven, U. Abbas, A. Abreu Aramburu, S. Accart, C. Aerts, G. Altavilla, M. A. Álvarez, R. Alvarez, J. Alves, R. I. Anderson, A. H. Andrei, E. Anglada Varela, E. Antiche, T. Antoja, B. Ar-

cay, T. L. Astraatmadja, N. Bach, S. G. Baker, L. Balaguer-Núñez, P. Balm, C. Barache, C. Barata, D. Barbato, F. Barblan, P. S. Barklem, D. Barrado, M. Barros, M. A. Barstow, S. Bartholomé Muñoz, J. L. Bassilana, U. Becciani, M. Bellazzini, A. Berihuete, S. Bertone, L. Bianchi, O. Bienaymé, S. Blanco-Cuaresma, T. Boch, C. Boeche, A. Bombrun, R. Borrachero, D. Bossini, S. Bouquillon, G. Bourda, A. Bragaglia, L. Bramante, M. A. Breddels, A. Bressan, N. Brouillet, T. Brüsemeister, E. Brugaletta, B. Bucciarelli, A. Burlacu, D. Busonero, A. G. Butkevich, R. Buzzi, E. Caffau, R. Cancelliere, G. Cannizzaro, T. Cantat-Gaudin, R. Carballo, T. Carlucci, J. M. Carrasco, L. Casamiquela, M. Castellani, A. Castro-Ginard, P. Charlot, L. Chemin, A. Chiavassa, G. Cocozza, G. Costigan, S. Cowell, F. Crifo, M. Crosta, C. Crowley, J. Cuypers, C. Dafonte, Y. Damerdji, A. Dapergolas, P. David, M. David, P. de Laverny, F. De Luise, R. De March, D. de Martino, R. de Souza, A. de Torres, J. Debosscher, E. del Pozo, M. Delbo, A. Delgado, H. E. Delgado, P. Di Matteo, S. Diakite, C. Diener, E. Distefano, C. Dolding, P. Drazinos, J. Durán, B. Edvardsson, H. Enke, K. Eriksson, P. Esquej, G. Eynard Bontemps, C. Fabre, M. Fabrizio, S. Faigler, A. J. Falcão, M. Farràs Casas, L. Federici, G. Fedorets, P. Fernique, F. Figueras, F. Filippi, K. Findeisen, A. Fonti, E. Fraile, M. Fraser, B. Frézouls, M. Gai, S. Galleti, D. Garabato, F. García-Sedano, A. Garofalo, N. Garralda, A. Gavel, P. Gavras, J. Gerssen, R. Geyer, P. Giacobbe, G. Gilmore, S. Girona, G. Giuffrida, F. Glass, M. Gomes, M. Granvik, A. Gueguen, A. Guerrier, J. Guiraud, R. Gutiérrez-Sánchez, R. Haigron, D. Hatzidimitriou, M. Hauser, M. Haywood, U. Heiter, A. Helmi, J. Heu, T. Hilger, D. Hobbs, W. Hofmann, G. Holland, H. E. Huckle, A. Hypki, V. Icardi, K. Janßen, G. Jevardat de Fombelle, P. G. Jonker, Á. L. Juhász, F. Julbe, A. Karampelas, A. Kewley, J. Klar, A. Kochoska, R. Kohley, K. Kolenberg, M. Kontizas, E. Kontizas, S. E. Koposov, G. Kordopatis, Z. Kostrzewa-Rutkowska, P. Koubsky, S. Lambert, A. F. Lanza, Y. Lasne, J. B. Lavigne, Y. Le Fustec, C. Le Poncin-Lafitte, Y. Lebreton, S. Leccia, N. Leclerc, I. Lecoeur-Taibi, H. Lenhardt, F. Leroux, S. Liao, E. Licata, H. E. P. Lindstrøm, T. A. Lister, E. Livanou, A. Lobel, M. López, S. Managau, R. G. Mann, G. Mantelet, O. Marchal, J. M. Marchant, M. Marconi, S. Marinoni, G. Marschalkó, D. J. Marshall, M. Martino, G. Marton, N. Mary, D. Massari, G. Matijevič, T. Mazeh, P. J. McMillan, S. Messina, D. Michalik, N. R. Millar, D. Molina, R. Molinaro, L. Molnár, P. Montegriffo, R. Mor, R. Morbidelli, T. Morel, D. Morris, A. F. Mulone, T. Muraveva, I. Musella, G. Nelemans, L. Nicastro, L. Noval, W. O'Mullane, C. Ordénovic, D. Ordóñez-Blanco, P. Osborne, C. Pagani, I. Pagano, F. Pailler, H. Palacin, L. Palaversa, A. Panahi, M. Pawlak, A. M. Piersimoni, F. X. Pineau, E. Plachy, G. Plum, E. Poggio, E. Poujoulet, A. Prša, L. Pulone, E. Racero, S. Ragaini, N. Rambaux, M. Ramos-Lerate, S. Regibo, C. Reylé, F. Riclet, V. Ripepi, A. Riva, A. Rivard, G. Rixon, T. Roegiers, M. Roelens, M. Romero-Gómez, N. Rowell, F. Royer, L. Ruiz-Dern, G. Sadowski, T. Sagristà Sellés, J. Sahlmann, J. Salgado, E. Salguero, N. Sanna, T. Santana-Ros, M. Sarasso, H. Savietto, M. Schultheis, E. Sciacca, M. Segol, J. C. Segovia, D. Ségransan, I. C. Shih, L. Siltala, A. F. Silva, R. L. Smart, K. W. Smith, E. Solano, F. Solitro, R. Sordo, S. Soria Nieto, J. Souchay, A. Spagna, F. Spoto, U. Stampa, I. A. Steele, H. Steidelmüller, C. A. Stephenson, H. Stoev, F. F. Suess, J. Surdej, L. Szabados, E. Szegedi-Elek, D. Tapiador, F. Taris, G. Tauran, M. B. Taylor, R. Teixeira, D. Terrett, P. Teyssand ier, W. Thuillot, A. Titarenko, F. Torra Clotet, C. Turon, A. Ulla, E. Utrilla, S. Uzzi, M. Vaillant, G. Valentini, V. Valette, A. van Elteren, E. Van Hemelryck, M. van Leeuwen, M. Vaschetto, A. Vecchiato, J. Veljanoski, Y. Viala, D. Vicente, S. Vogt, C. von Essen, H. Voss, V. Votruba, S. Voutsinas, G. Walmsley, M. Weiler, O. Wertz, T. Wevers, Ł. Wyrzykowski, A. Yoldas, M. Žerjal, H. Ziaeepour, J. Zorec, S. Zschocke, S. Zucker, C. Zurbach, and T. Zwitter. Gaia Data Release 2. Summary of the contents and survey properties. *A&A*, 616:A1, Aug 2018. 1.2.1, 1.6, 2.1, 2.2

[35] Jinhee Lee and Inseok Song. Bayesian assessment of moving group membership: importance of models and prior knowledge. *MNRAS*, 475(3):2955–2970, April 2018. 1.2.1

[36] Jinhee Lee and Inseok Song. Development of models for nearby young stellar moving groups: Creation, revision, and finalization of the models. *Monthly Notices of the Royal Astronomical Society*, 486(3):3434–3450, 2019. 1.2.1

[37] Jonathan P. Williams and Lucas A. Cieza. Protoplanetary Disks and Their Evolution. *ARA&A*, 49(1):67–117, September 2011. 1.3

[38] David Nesvorný. Dynamical Evolution of the Early Solar System. *ARA&A*, 56:137–174, September 2018. 1.3

[39] T. Birnstiel, M. Fang, and A. Johansen. Dust Evolution and the Formation of Planetesimals. *SSRv*, 205(1-4):41–75, December 2016. 1.3

[40] J. E. Owen, B. Ercolano, C. J. Clarke, and R. D. Alexander. Radiation-hydrodynamic models of X-ray and EUV photoevaporating protoplanetary discs. *MNRAS*, 401(3):1415–1428, January 2010. 1.3

[41] P. Pinilla, T. Birnstiel, L. Ricci, C. P. Dullemond, A. L. Uribe, L. Testi, and A. Natta. Trapping dust particles in the outer regions of protoplanetary disks. *A&A*, 538:A114, February 2012. 1.3.1

[42] P. Pinilla, M. Benisty, and T. Birnstiel. Ring shaped dust accumulation in transition disks. *A&A*, 545:A81, September 2012. 1.3.1

[43] Edwin A. Bergin and Jonathan P. Williams. The Determination of Protoplanetary Disk Masses. In Martin Pessah and Oliver Gressel, editors, *Formation, Evolution, and Dynamics of Young Solar Systems*, volume 445 of *Astrophysics and Space Science Library*, page 1, January 2017. 1.4.1

[44] A. Dutrey, S. Guilloteau, V. Piétu, E. Chapillon, V. Wakelam, E. Di Folco, T. Stoecklin, O. Denis-Alpizar, U. Gorti, R. Teague, T. Henning, D. Semenov, and N. Grosso. The Flying Saucer: Tomography of the thermal and density gas structure of an edge-on protoplanetary disk. *A&A*, 607:A130, November 2017. 1.4.1, 4.1, 4.4.1, 4.4.3

[45] Sean M. Andrews, Jane Huang, Laura M. Pérez, Andrea Isella, Cornelis P. Dullemond, Nicolás T. Kurtovic, Viviana V. Guzmán, John M. Carpenter, David J. Wilner, Shangjia Zhang, Zhaohuan Zhu, Tilman Birnstiel, Xue-Ning Bai, Myriam Benisty, A. Meredith

Hughes, Karin I. Öberg, and Luca Ricci. The Disk Substructures at High Angular Resolution Project (DSHARP). I. Motivation, Sample, Calibration, and Overview. *ApJL*, 869(2):L41, December 2018. 1.4.1, 1.5

[46] Jane Huang, Sean M. Andrews, Cornelis P. Dullemond, Andrea Isella, Laura M. Pérez, Viviana V. Guzmán, Karin I. Öberg, Zhaohuan Zhu, Shangjia Zhang, Xue-Ning Bai, Myriam Benisty, Tilman Birnstiel, John M. Carpenter, A. Meredith Hughes, Luca Ricci, Erik Weaver, and David J. Wilner. The Disk Substructures at High Angular Resolution Project (DSHARP). II. Characteristics of Annular Substructures. *ApJL*, 869(2):L42, December 2018. 1.4.1, 1.5

[47] Jeff Jennings, Richard A. Booth, Marco Tazzari, Cathie J. Clarke, and Giovanni P. Rosotti. A super-resolution analysis of the DSHARP survey: substructure is common in the inner 30 au. *MNRAS*, 509(2):2780–2799, January 2022. 1.4.1

[48] Valentin Christiaens, Faustine Cantalloube, Simon Casassus, Daniel J. Price, Olivier Absil, Christophe Pinte, Julien Girard, and Matias Montesinos. Evidence for a Circumplanetary Disk around Protoplanet PDS 70 b. *ApJL*, 877(2):L33, June 2019. 1.4.1

[49] Myriam Benisty, Jaehan Bae, Stefano Facchini, Miriam Keppler, Richard Teague, Andrea Isella, Nicolas T. Kurtovic, Laura M. Pérez, Anibal Sierra, Sean M. Andrews, John Carpenter, Ian Czekala, Carsten Dominik, Thomas Henning, Francois Menard, Paola Pinilla, and Alice Zurlo. A Circumplanetary Disk around PDS70c. *ApJL*, 916(1):L2, July 2021. 1.4.1

[50] Charles J. Law, Sage Crystian, Richard Teague, Karin I. Öberg, Evan A. Rich, Sean M. Andrews, Jaehan Bae, Kevin Flaherty, Viviana V. Guzmán, Jane Huang, John D. Ilee, Joel H. Kastner, Ryan A. Loomis, Feng Long, Laura M. Pérez, Sebastián Pérez, Chunhua Qi, Giovanni P. Rosotti, Dary Ruíz-Rodríguez, Takashi Tsukagoshi, and David J. Wilner. CO Line Emission Surfaces and Vertical Structure in Mid-Inclination Protoplanetary Disks. *arXiv e-prints*, page arXiv:2205.01776, May 2022. 1.4.1

[51] Paola Caselli and Cecilia Ceccarelli. Our astrochemical heritage. *A&ARv*, 20:56, October 2012. 1.4.2

[52] Jes K. Jørgensen, Arnaud Belloche, and Robin T. Garrod. Astrochemistry During the Formation of Stars. *ARA&A*, 58:727–778, August 2020. 1.4.2

[53] Eric Herbst and Ewine F. van Dishoeck. Complex Organic Interstellar Molecules. *ARA&A*, 47(1):427–480, September 2009. 1.4.2

[54] Henning Avenhaus, Sascha P. Quanz, Antonio Garufi, Sebastian Perez, Simon Casassus, Christophe Pinte, Gesa H. M. Bertrang, Claudio Caceres, Myriam Benisty, and Carsten Dominik. Disks around T Tauri Stars with SPHERE (DARTTS-S). I. SPHERE/IRDIS Polarimetric Imaging of Eight Prominent T Tauri Disks. *ApJ*, 863(1):44, August 2018. 1.5

[55] Karin I. Öberg, Viviana V. Guzmán, Catherine Walsh, Yuri Aikawa, Edwin A. Bergin, Charles J. Law, Ryan A. Loomis, Felipe Alarcón, Sean M. Andrews, Jaehan Bae, Jennifer B. Bergner, Yann Boehler, Alice S. Booth, Arthur D. Bosman, Jenny K. Calahan, Gianni Cataldi, L. Ilsedore Cleeves, Ian Czekala, Kenji Furuya, Jane Huang, John D. Ilee, Nicolas T. Kurtovic, Romane Le Gal, Yao Liu, Feng Long, François Ménard, Hideko Nomura, Laura M. Pérez, Chunhua Qi, Kamber R. Schwarz, Anibal Sierra, Richard Teague, Takashi Tsukagoshi, Yoshihide Yamato, Merel L. R. van't Hoff, Abygail R. Waggoner, David J. Wilner, and Ke Zhang. Molecules with ALMA at Planet-forming Scales (MAPS). I. Program Overview and Highlights. *ApJ Supplement Series*, 257(1):1, November 2021. 1.5

[56] C. R. O'dell and Zheng Wen. Postrefurbishment Mission Hubble Space Telescope Images of the Core of the Orion Nebula: Proplyds, Herbig-Haro Objects, and Measurements of a Circumstellar Disk. *ApJ*, 436:194, November 1994. 1.5

[57] Dary Ruíz-Rodríguez, Joel H. Kastner, Ruobing Dong, David A. Principe, Sean M. Andrews, and David J. Wilner. Constraints on a Putative Planet Sculpting the V4046 Sagittarii Circumbinary Disk. *AJ*, 157(6):237, June 2019. 1.5

[58] A. P. Sousa, S. H. P. Alencar, J. Bouvier, J. Stauffer, L. Venuti, L. Hillenbrand, A. M. Cody, P. S. Teixeira, M. M. Guimarães, P. T. McGinnis, L. Rebull, E. Flaccomio, G. Fürész, G. Micela, and J. F. Gameiro. CSI 2264: Accretion process in classical T Tauri stars in the young cluster NGC 2264. *A&A*, 586:A47, February 2016. 1.5

[59] Jane Huang, Karin I. Öberg, Chunhua Qi, Yuri Aikawa, Sean M. Andrews, Kenji Furuya, Viviana V. Guzmán, Ryan A. Loomis, Ewine F. van Dishoeck, and David J. Wilner. An ALMA Survey of DCN/H^{13}CN and DCO^+/$H^{13}CO^+$ in Protoplanetary Disks. *ApJ*, 835(2):231, February 2017. 1.5

[60] Feng Long, Paola Pinilla, Gregory J. Herczeg, Daniel Harsono, Giovanni Dipierro, Ilaria Pascucci, Nathan Hendler, Marco Tazzari, Enrico Ragusa, Colette Salyk, Suzan Edwards, Giuseppe Lodato, Gerrit van de Plas, Doug Johnstone, Yao Liu, Yann Boehler, Sylvie Cabrit, Carlo F. Manara, Francois Menard, Gijs D. Mulders, Brunella Nisini, William J. Fischer, Elisabetta Rigliaco, Andrea Banzatti, Henning Avenhaus, and Michael Gully-Santiago. Gaps and Rings in an ALMA Survey of Disks in the Taurus Star-forming Region. *ApJ*, 869(1):17, December 2018. 1.5

[61] C. Pinte, F. Ménard, G. Duchêne, and P. Bastien. Monte Carlo radiative transfer in protoplanetary disks. *A&A*, 459(3):797–804, December 2006. 1.5.1, 3.4.1, 4.3.2

[62] C. Pinte, T. J. Harries, M. Min, A. M. Watson, C. P. Dullemond, P. Woitke, F. Ménard, and M. C. Durán-Rojas. Benchmark problems for continuum radiative transfer. High optical depths, anisotropic scattering, and polarisation. *A&A*, 498(3):967–980, May 2009. 1.5.1, 3.4.1, 4.3.2

[63] Simon J Murphy, Warrick A Lawson, and Michael S Bessell. Re-examining the membership and origin of the E Cha association. *Monthly Notices of the Royal Astronomical Society*, 435(2):1325–1349, 2013. 1.6, 2.1, 2.2, 3.1, 3.2, 3.3.1, 3.3.2, 3.4.1, 3.4.2, 3.4.2, 5.1

[64] D. A. Dickson-Vandervelde, E. C. Wilson, and J. H. Kastner. Gaia-based Isochronal, Kinematic, and Spatial Analysis of the ϵ Cha Association. *AJ*, 161(2):87, February 2021. 1.6, 3.1, 3.4.2, 3.4.2

[65] D. Annie Dickson-Vandervelde, Emily C. Wilson, and Joel H. Kastner. Identification of the Youngest Known Substellar Object within 100 pc. *Research Notes of the American Astronomical Society*, 4(2):25, Feb 2020. 1.6, 2.4.2.2, 3.1, 3.3.1, 3.3.2, 3.4.1, 3.4.3

[66] Joel H. Kastner, Emily A. Thompson, Rodolfo Montez, Simon J. Murphy, Michael S. Bessell, and Giuseppe Germano Sacco. 2M1155-79 (= T Chamaeleontis B): A Low-mass, Wide-separation Companion to the nearby, “Old” T Tauri Star T Chamaeleontis. *ApJL*, 747(2):L23, Mar 2012. 1.6, 2.4.1.2, 2.4.2.2, 2.4.2.3, 3.1, 3.3.1, 3.3.2, 3.4.1, 3.5

[67] G. G. Sacco, J. H. Kastner, T. Forveille, D. Principe, R. Montez, B. Zuckerman, and P. Hily-Blant. Molecules in the transition disk orbiting T Chamaeleontis. *A&A*, 561:A42, January 2014. 1.6, 2.1, 2, 4.1, 4.3.1, 5.2.3

[68] Joel Kastner, Katelyn Allers, Brendan Bowler, Thayne Currie, Jeremy Drake, Trent Dupuy, Jackie Faherty, Jonathan Gagne, Michael Liu, Eric Mamajek, Dimitri Mawet, Evgenya Shkolnik, Inseok Song, Russel White, and Ben Zuckerman. The Early Evolution of Stars and Exoplanet Systems: Exploring and Exploiting Nearby, Young Stars. *BAAS*, 51(3):294, May 2019. 2.1

[69] Adam C. Schneider, Evgenya L. Shkolnik, Katelyn N. Allers, Adam L. Kraus, Michael C. Liu, Alycia J. Weinberger, and Laura Flagg. ACRONYM. III. Radial Velocities for 336 Candidate Young Low-mass Stars in the Solar Neighborhood, Including 77 Newly Confirmed Young Moving Group Members. *AJ*, 157(6):234, June 2019. 2.1

[70] Caprice L. Phillips, Brendan P. Bowler, Gregory Mace, Michael C. Liu, and Kimberly Sokal. 2MASS J04435686+3723033 B: A Young Companion at the Substellar Boundary with Potential Membership in the β Pictoris Moving Group. *ApJ*, 896(2):173, June 2020. 2.1

[71] Jonathan Gagné, Eileen C. Gonzales, and Jacqueline K. Faherty. A Gaia DR2 Confirmation that 2MASS J12074836-3900043 is a Member of the TW HYA Association. *Research Notes of the American Astronomical Society*, 2(2):17, May 2018. 2.1

[72] B. Zuckerman, Beth Klein, and Joel Kastner. The Nearby, Young, χ ^{1} Fornacis Cluster: Membership, Age, and an Extraordinary Ensemble of Dusty Debris Disks. *ApJ*, 887(1):87, December 2019. 2.1, 2.5.1, 2.5.2

[73] Nicholas J. Wright and Eric E. Mamajek. The kinematics of the Scorpius-Centaurus OB association from Gaia DR1. *MNRAS*, 476(1):381–398, May 2018. 2.1

[74] Jonathan Gagné, Jacqueline K. Faherty, and Eric E. Mamajek. Volans-Carina: A New 90 Myr Old Stellar Association at 85 pc. *ApJ*, 865(2):136, October 2018. 2.1, 2.3.1, 2.5.3

[75] Eric E. Mamajek, Warrick A. Lawson, and Eric D. Feigelson. The η Chamaeleontis Cluster: Origin in the Sco-Cen OB Association. *ApJ*, 544(1):356–374, November 2000. 2.1

[76] Eric D. Feigelson, Warrick A. Lawson, and Gordon P. Garmire. The $\in$ Chamaeleontis Young Stellar Group and the Characterization of Sparse Stellar Clusters. *ApJ*, 599(2):1207–1222, December 2003. 2.1, 2.4.2.3

[77] A. S. Hales, I. De Gregorio-Monsalvo, B. Montesinos, S. Casassus, W. F. R. Dent, C. Dougados, C. Eiroa, A. M. Hughes, G. Garay, D. Mardones, F. Ménard, Aina Palau, S. Pérez, N. Phillips, J. M. Torrelles, and D. Wilner. A CO Survey in Planet-forming Disks: Characterizing the Gas Content in the Epoch of Planet Formation. *AJ*, 148(3):47, September 2014. 2.1

[78] Paola Testa, David P. Huenemoerder, Norbert S. Schulz, and Kazunori Ishibashi. X-Ray Emission from Young Stellar Objects in the epsilon Chamaeleontis Group: The Herbig Ae Star HD 104237 and Associated Low-Mass Stars. *ApJ*, 687(1):579–597, November 2008. 2.1

[79] Joel H. Kastner, Pierry Hily-Blant, G. G. Sacco, Thierry Forveille, and B. Zuckerman. Detection of a Molecular Disk Orbiting the Nearby, “old,” Classical T Tauri Star MP Muscae. *ApJL*, 723(2):L248–L251, November 2010. 2.1

[80] S. Desidera, E. Covino, S. Messina, J. Carson, J. Hagelberg, J. E. Schlieder, K. Biazzo, J. M. Alcalá, G. Chauvin, A. Vigan, J. L. Beuzit, M. Bonavita, M. Bonnefoy, P. Delorme, V. D’Orazi, M. Esposito, M. Feldt, L. Girardi, R. Gratton, T. Henning, A. M. Lagrange, A. C. Lanzafame, R. Launhardt, M. Marmier, C. Melo, M. Meyer, D. Mouillet, C. Moutou, D. Segransan, S. Udry, and C. M. Zaidi. The VLT/NaCo large program to probe the occurrence of exoplanets and brown dwarfs in wide orbits. I. Sample definition and characterization. *A&A*, 573:A126, January 2015. 2.2

[81] G. A. Gontcharov. Pulkovo Compilation of Radial Velocities for 35 495 Hipparcos stars in a common system. *Astronomy Letters*, 32(11):759–771, November 2006. 2.2

[82] C. A. Grady, B. Woodgate, Carlos A. O. Torres, Th. Henning, D. Apai, J. Rodmann, Hongchi Wang, B. Stecklum, H. Linz, G. M. Williger, A. Brown, E. Wilkinson, G. M. Harper, G. J. Herczeg, A. Danks, G. L. Vieira, E. Malumuth, N. R. Collins, and R. S. Hill. The Environment of the Optically Brightest Herbig Ae Star, HD 104237. *ApJ*, 608(2):809–830, June 2004. 2.2, 2.4.2.3

[83] E. W. Guenther, M. Esposito, R. Mundt, E. Covino, J. M. Alcalá, F. Cusano, and B. Stecklum. Pre-main sequence spectroscopic binaries suitable for VLTI observations. *A&A*, 467(3):1147–1155, June 2007. 2.2, 2.4.1.3

[84] B. Lopez Martí, F. Jimenez Esteban, A. Bayo, D. Barrado, E. Solano, and C. Rodrigo. Proper motions of young stars in Chamaeleon. I. A Virtual Observatory study of spectroscopically confirmed members. *A&A*, 551:A46, March 2013. 2.2

[85] Lison Malo, Étienne Artigau, René Doyon, David Lafrenière, Loïc Albert, and Jonathan Gagné. BANYAN. III. Radial Velocity, Rotation, and X-Ray Emission of Low-mass Star Candidates in Nearby Young Kinematic Groups. *ApJ*, 788(1):81, June 2014. 2.2

[86] G. Kordopatis, G. Gilmore, M. Steinmetz, C. Boeche, G. M. Seabroke, A. Siebert, T. Zwitter, J. Binney, P. de Laverny, A. Recio-Blanco, M. E. K. Williams, T. Piffl, H. Enke, S. Roeser, A. Bijaoui, R. F. G. Wyse, K. Freeman, U. Munari, I. Carrillo, B. Anguiano, D. Burton, R. Campbell, C. J. P. Cass, K. Fiegert, M. Hartley, Q. A. Parker, W. Reid, A. Ritter, K. S. Russell, M. Stupar, F. G. Watson, O. Bienaymé, J. Bland -Hawthorn, O. Gerhard, B. K. Gibson, E. K. Grebel, A. Helmi, J. F. Navarro, C. Conrad, B. Famaey, C. Faure, A. Just, J. Kos, G. Matijevič, P. J. McMillan, I. Minchev, R. Scholz, S. Sharma, A. Siviero, E. Wylie de Boer, and M. Žerjal. The Radial Velocity Experiment (RAVE): Fourth Data Release. *AJ*, 146(5):134, November 2013. 2.2

[87] E. Schisano, E. Covino, J. M. Alcalá, M. Esposito, D. Gandolfi, and E. W. Guenther. Variability of the transitional T Tauri star T Chamaeleontis. *A&A*, 501(3):1013–1030, July 2009. 2.2, 2.4.1.3, 4.1, 4.3.2

[88] L. Terranegra, F. Morale, A. Spagna, G. Massone, and M. G. Lattanzi. Proper motions of faint ROSAT WTT stars in the Chamaeleon region. *A&A*, 341:L79–L83, January 1999. 2.2

[89] C. A. O. Torres, G. R. Quast, L. da Silva, R. de La Reza, C. H. F. Melo, and M. Sterzik. Search for associations containing young stars (SACY). I. Sample and searching method. *A&A*, 460(3):695–708, December 2006. 2.2, 4.1

[90] L. Lindegren, J. Hernández, A. Bombrun, S. Klioner, U. Bastian, M. Ramos-Lerate, A. de Torres, H. Steidelmüller, C. Stephenson, D. Hobbs, U. Lammers, M. Biermann,

R. Geyer, T. Hilger, D. Michalik, U. Stampa, P. J. McMillan, J. Castañeda, M. Clotet, G. Comoretto, M. Davidson, C. Fabricius, G. Gracia, N. C. Hambly, A. Hutton, A. Mora, J. Portell, F. van Leeuwen, U. Abbas, A. Abreu, M. Altmann, A. Andrei, E. Anglada, L. Balaguer-Núñez, C. Barache, U. Becciani, S. Bertone, L. Bianchi, S. Bouquillon, G. Bourda, T. Brüsemeister, B. Bucciarelli, D. Busonero, R. Buzzi, R. Cancelliere, T. Carlucci, P. Charlot, N. Cheek, M. Crosta, C. Crowley, J. de Bruijne, F. de Felice, R. Drimmel, P. Esquej, A. Fienga, E. Fraile, M. Gai, N. Garralda, J. J. González-Vidal, R. Guerra, M. Hauser, W. Hofmann, B. Holl, S. Jordan, M. G. Lattanzi, H. Lenhardt, S. Liao, E. Licata, T. Lister, W. Löffler, J. Marchant, J. M. Martin-Fleitas, R. Messineo, F. Mignard, R. Morbidelli, E. Poggio, A. Riva, N. Rowell, E. Salguero, M. Sarasso, E. Sciacca, H. Siddiqui, R. L. Smart, A. Spagna, I. Steele, F. Taris, J. Torra, A. van Elteren, W. van Reeven, and A. Vecchiato. Gaia Data Release 2. The astrometric solution. *A&A*, 616:A2, Aug 2018. 2.2, 2.4, 2.5

[91] L. Lindegren. Re-normalising the astrometric chi-square in Gaia DR2. GAIA-C3-TN-LU-LL-124, August 2018. 2.2

[92] Vasily Belokurov, Zephyr Penoyre, Semyeong Oh, Giuliano Iorio, Simon Hodgkin, N. Wyn Evans, Andrew Everall, Sergey E. Koposov, Christopher A. Tout, Robert Izzard, Cathie J. Clarke, and Anthony G. A. Brown. Unresolved stellar companions with Gaia DR2 astrometry. *arXiv e-prints*, page arXiv:2003.05467, March 2020. 2.3.1

[93] Jonathan Gagné, Eric E. Mamajek, Lison Malo, Adric Riedel, David Rodriguez, David Lafrenière, Jacqueline K. Faherty, Olivier Roy-Loubier, Laurent Pueyo, Annie C. Robin, and René Doyon. BANYAN. XI. The BANYAN Σ Multivariate Bayesian Algorithm to Identify Members of Young Associations with 150 pc. *ApJ*, 856(1):23, March 2018. 2.3.2, 2.4.1.4

[94] César Briceño and Andrei Tokovinin. New Binaries in the $\in$ Cha Association. *AJ*, 154(5):195, November 2017. 2.4, 2.5, 2.4.1.5, 2.4.2.1, 2.4.2.1, 2.5.1

[95] S. H. P. Alencar, P. S. Teixeira, M. M. Guimarães, P. T. McGinnis, J. F. Gameiro, J. Bouvier, S. Aigrain, E. Flaccomio, and F. Favata. Accretion dynamics and disk evolution in NGC 2264: a study based on CoRoT photometric observations. *A&A*, 519:A88, September 2010. 2.4.1.3, 4.1

[96] J Olofsson, M Benisty, J. B. Le Bouquin, J. P. Berger, S Lacour, F Ménard, Th Henning, A Crida, L Burtscher, G Meeus, T Ratzka, C Pinte, J. C. Augereau, F Malbet, B Lazareff, and W Traub. Sculpting the disk around T Chamaeleontis: An interferometric view. *Astronomy and Astrophysics*, 552, 2013. 2.4.1.3, 4.1, 4.3.2, 4.3.2, 4.4.1

[97] Jason A. Cardelli, Geoffrey C. Clayton, and John S. Mathis. The Relationship between Infrared, Optical, and Ultraviolet Extinction. *ApJ*, 345:245, October 1989. 2.4.1.3, 3.2

[98] K. L. Luhman. A Survey for Low-Mass Stars and Brown Dwarfs in the η Chamaeleontis and $\in$ Chamaeleontis Young Associations. *ApJ*, 616(2):1033–1041, December 2004. 2.4.1.3, 3.4.2

[99] M. Fang, R. van Boekel, J. Bouwman, Th. Henning, W. A. Lawson, and A. Sicilia-Aguilar. Young stars in $\in$ Chamaleontis and their disks: disk evolution in sparse associations. *A&A*, 549:A15, January 2013. 2.4.1.3, 3.4.2, 3.4.2

[100] Mark J Pecaut and Eric E Mamajek. Intrinsic colors, temperatures, and bolometric corrections of pre-main-sequence stars. *Astrophysical Journal, Supplement Series*, 208(1):9, 2013. 2.4.1.4, 2.4.2.2

[101] Rainer Köhler. Multiplicity of X-Ray-selected T Tauri Stars in Chamaeleon. *AJ*, 122(6):3325–3334, December 2001. 2.4.2.1

[102] Joel H. Kastner. Candidate Wide-separation Companions to Nearby, Dusty Young Stars: Gaia Weighs In. *Research Notes of the American Astronomical Society*, 2(3):137, Aug 2018. 2.4.2.1, 2.4.2.2, 2.4.2.3, 3.1, 3.4.2

[103] Maria C. Schutte, Kellen D. Lawson, John P. Wisniewski, Marc J. Kuchner, Steven M. Silverberg, Jacqueline K. Faherty, Daniella C. Bardalez Gagliuffi, Rocio Kiman,

Jonathan Gagné, Aaron Meisner, Adam C. Schneider, Alissa S. Bans, John H. Debes, Natalie Kovacevic, Milton K. D. Bosch, Hugo A. Durantini Luca, Jonathan Holden, Michiharu Hyogo, and Disk Detective Collaboration. Discovery of a Nearby Young Brown Dwarf Disk. *AJ*, 160(4):156, October 2020. 2.4.2.2, 2.5.3

[104] Gaspard Duchêne and Adam Kraus. Stellar Multiplicity. *ARA&A*, 2013. 2.5.1

[105] Ivan King. The structure of star clusters. I. an empirical density law. *AJ*, 67:471, October 1962. 2.5.2

[106] Eric E. Mamajek. A Pre-Gaia Census of Nearby Stellar Groups. In J. H. Kastner, B. Stelzer, and S. A. Metchev, editors, *Young Stars & Planets Near the Sun*, volume 314 of *IAU Symposium*, pages 21–26, January 2016. 2.5.2

[107] J. K. Donaldson, A. J. Weinberger, J. Gagné, J. K. Faherty, A. P. Boss, and S. A. Keiser. New Parallaxes and a Convergence Analysis for the TW Hya Association. *ApJ*, 833(1):95, December 2016. 2.5.3

[108] Cameron P. M. Bell, Eric E. Mamajek, and Tim Naylor. A self-consistent, absolute isochronal age scale for young moving groups in the solar neighbourhood. *MNRAS*, 454(1):593–614, November 2015. 2.5.3

[109] Aaron Dotter. MESA Isochrones and Stellar Tracks (MIST) 0: Methods for the Construction of Stellar Isochrones. *ApJs*, 222(1):8, January 2016. 3

[110] Jieun Choi, Aaron Dotter, Charlie Conroy, Matteo Cantiello, Bill Paxton, and Benjamin D. Johnson. Mesa Isochrones and Stellar Tracks (MIST). I. Solar-scaled Models. *ApJ*, 823(2):102, June 2016. 3

[111] Bill Paxton, Lars Bildsten, Aaron Dotter, Falk Herwig, Pierre Lesaffre, and Frank Timmes. Modules for Experiments in Stellar Astrophysics (MESA). *ApJs*, 192(1):3, January 2011. 3

[112] Bill Paxton, Matteo Cantiello, Phil Arras, Lars Bildsten, Edward F. Brown, Aaron Dotter, Christopher Mankovich, M. H. Montgomery, Dennis Stello, F. X. Timmes, and Richard Townsend. Modules for Experiments in Stellar Astrophysics (MESA): Planets, Oscillations, Rotation, and Massive Stars. *ApJs*, 208(1):4, September 2013. 3

[113] Bill Paxton, Pablo Marchant, Josiah Schwab, Evan B. Bauer, Lars Bildsten, Matteo Cantiello, Luc Dessart, R. Farmer, H. Hu, N. Langer, R. H. D. Townsend, Dean M. Townsley, and F. X. Timmes. Modules for Experiments in Stellar Astrophysics (MESA): Binaries, Pulsations, and Explosions. *ApJs*, 220(1):15, September 2015. 3

[114] M. Simon, S. Guilloteau, Tracy L. Beck, E. Chapillon, E. Di Folco, A. Dutrey, Gregory A. Feiden, N. Grosso, V. Piétu, L. Prato, and Gail H. Schaefer. Masses and Implications for Ages of Low-mass Pre-main-sequence Stars in Taurus and Ophiuchus. *ApJ*, 884(1):42, October 2019. 2.5.3

[115] J. H. Kastner, B. Stelzer, and S. A. Metchev, editors. *Young Stars & Planets Near the Sun,*, volume 314, January 2016. 3.1

[116] Ya-Lin Wu, Laird M. Close, Jared R. Males, Travis S. Barman, Katie M. Morzinski, Katherine B. Follette, Vanessa Bailey, Timothy J. Rodigas, Philip Hinz, Alfio Puglisi, Marco Xompero, and Runa Briguglio. New Extinction and Mass Estimates from Optical Photometry of the Very Low Mass Brown Dwarf Companion CT Chamaeleontis B with the Magellan AO System. *ApJ*, 801(1):4, Mar 2015. 3.1

[117] Ya-Lin Wu, Laird M. Close, Jared R. Males, Travis S. Barman, Katie M. Morzinski, Katherine B. Follette, Vanessa P. Bailey, Timothy J. Rodigas, Philip Hinz, Alfio Puglisi, Marco Xompero, and Runa Briguglio. New Extinction and Mass Estimates of the Low-mass Companion 1RXS 1609 B with the Magellan AO System: Evidence of an Inclined Dust Disk. *ApJL*, 807(1):L13, Jul 2015. 3.1

[118] Ya-Lin Wu, Laird M. Close, Vanessa P. Bailey, Timothy J. Rodigas, Jared R. Males, Katie M. Morzinski, Katherine B. Follette, Philip M. Hinz, Alfio Puglisi, Runa Briguglio,

and Marco Xompero. Magellan AO System z', Y $_S$, and L' Observations of the Very Wide 650 AU HD 106906 Planetary System. *ApJ*, 823(1):24, May 2016. 3.1

[119] D. Nguyen-Thanh, N. Phan-Bao, S. J. Murphy, and M. S. Bessell. Sporadic and intense accretion in a 1 Myr-old brown dwarf candidate. *A&A*, 634:A128, February 2020. 3.1, 3.4.2

[120] C. A. L. Bailer-Jones, J. Rybizki, M. Fouesneau, M. Demleitner, and R. Andrae. Estimating Distances from Parallaxes. V. Geometric and Photogeometric Distances to 1.47 Billion Stars in Gaia Early Data Release 3. *AJ*, 161(3):147, March 2021. 3.1, 4.1

[121] L. Rodet, H. Beust, M. Bonnefoy, R. J. De Rosa, P. Kalas, and A. M. Lagrange. ODEA: Orbital Dynamics in a complex Evolving Architecture. Application to the planetary system HD 106906. *A&A*, 631:A139, Nov 2019. 3.1

[122] A. M. Lagrange, M. Langlois, R. Gratton, A. L. Maire, J. Milli, J. Olofsson, A. Vigan, V. Bailey, D. Mesa, G. Chauvin, A. Boccaletti, R. Galicher, J. H. Girard, M. Bonnefoy, M. Samland, F. Menard, T. Henning, M. Kenworthy, C. Thalmann, H. Beust, J. L. Beuzit, W. Brandner, E. Buenzli, A. Cheetham, M. Janson, H. le Coroller, J. Lannier, D. Mouillet, S. Peretti, C. Perrot, G. Salter, E. Sissa, Z. Wahhaj, L. Abe, S. Desidera, M. Feldt, F. Madec, D. Perret, C. Petit, P. Rabou, C. Soenke, and L. Weber. A narrow, edge-on disk resolved around HD 106906 with SPHERE. *A&A*, 586:L8, February 2016. 3.1

[123] Núria Miret-Roig, Hervé Bouy, Sean N. Raymond, Motohide Tamura, Emmanuel Bertin, David Barrado, Javier Olivares, Phillip A. B. Galli, Jean-Charles Cuillandre, Luis Manuel Sarro, Angel Berihuete, and Nuria Huélamo. A rich population of free-floating planets in the Upper Scorpius young stellar association. *Nature Astronomy*, 6:89–97, January 2022. 3.1

[124] N. Lodieu, N. C. Hambly, and N. J. G. Cross. Exploring the planetary-mass population in the Upper Scorpius association. *MNRAS*, 503(2):2265–2279, May 2021. 3.1

[125] John J. Bochanski, Joseph F. Hennawi, Robert A. Simcoe, J. Xavier Prochaska, Andrew A. West, Adam J. Burgasser, Scott M. Burles, Rebecca A. Bernstein, Christopher L. Williams, and Michael T. Murphy. MASE: A New Data-Reduction Pipeline for the Magellan Echellette Spectrograph. *PASP*, 121(886):1409, December 2009. 3.2

[126] William D. Vacca, Michael C. Cushing, and John T. Rayner. A Method of Correcting Near-Infrared Spectra for Telluric Absorption. *PASP*, 115(805):389–409, March 2003. 3.2

[127] Michael C. Cushing, William D. Vacca, and John T. Rayner. Spextool: A Spectral Extraction Package for SpeX, a 0.8-5.5 Micron Cross-Dispersed Spectrograph. *PASP*, 116(818):362–376, April 2004. 3.2

[128] E. L. Fitzpatrick, Derck Massa, Karl D. Gordon, Ralph Bohlin, and Geoffrey C. Clayton. An Analysis of the Shapes of Interstellar Extinction Curves. VII. Milky Way Spectrophotometric Optical-through-ultraviolet Extinction and Its R-dependence. *ApJ*, 886(2):108, December 2019. 3.2

[129] K. N. Allers and Michael C. Liu. A Near-infrared Spectroscopic Study of Young Field Ultracool Dwarfs. *ApJ*, 772(2):79, August 2013. 3.3.1.2

[130] Edward F. Schlafly, Aaron M. Meisner, and Gregory M. Green. The unWISE Catalog: Two Billion Infrared Sources from Five Years of WISE Imaging. *ApJ Supplement Series*, 240(2):30, February 2019. 3.3.2

[131] R. G. McMahon, M. Banerji, E. Gonzalez, S. E. Koposov, V. J. Bejar, N. Lodieu, R. Rebolo, and VHS Collaboration. VizieR Online Data Catalog: The VISTA Hemisphere Survey (VHS) catalog DR5 (McMahon+, 2020). *VizieR Online Data Catalog*, page II/367, January 2021. 3.3.3

[132] Joel H. Kastner, Valerie Rapson, Benjamin Sargent, C. T. Smith, and John Rayner. V4046 Sgr: Touchstone to Investigate Spectral Type Discrepancies for Pre-main Sequence Stars. In *18th Cambridge Workshop on Cool Stars, Stellar Systems, and the Sun*,

volume 18 of *Cambridge Workshop on Cool Stars, Stellar Systems, and the Sun*, pages 313–320, January 2015. 3.4.1

[133] Mark J. Pecaut. Anomalous Spectral Types and Intrinsic Colors of Young Stars. In J. H. Kastner, B. Stelzer, and S. A. Metchev, editors, *Young Stars & Planets Near the Sun*, volume 314, pages 85–90, January 2016. 3.4.1

[134] Dagny L. Looper, John J. Bochanski, Adam J. Burgasser, Subhanjoy Mohanty, Eric E. Mamajek, Jacqueline K. Faherty, Andrew A. West, and Mark A. Pitts. A Widely Separated, Highly Occluded Companion to the Nearby Low-mass T Tauri Star TWA 30. *AJ*, 140(5):1486–1499, November 2010. 3.4.2, 3.4.2, 3.4.2

[135] Adam Schneider, Carl Melis, and Inseok Song. TW HYA Association Membership and New WISE-detected Circumstellar Disks. *ApJ*, 754(1):39, July 2012. 3.4.2

[136] David A. Principe, G. Sacco, J. H. Kastner, B. Stelzer, and J. M. Alcalá. Evidence for variable, correlated X-ray and optical/IR extinction towards the nearby, pre-main-sequence binary TWA 30. *MNRAS*, 459(2):2097–2105, June 2016. 3.4.2, 3.4.2

[137] K. L. Luhman and T. L. Esplin. Refining the Census of the Upper Scorpius Association with Gaia. *AJ*, 160(1):44, July 2020. 3.4.2

[138] V. Christiaens, M. G. Ubeira-Gabellini, H. Cánovas, P. Delorme, B. Pairet, O. Absil, S. Casassus, J. H. Girard, A. Zurlo, Y. Aoyama, G. D. Marleau, L. Spina, N. van der Marel, L. Cieza, G. Lodato, S. Pérez, C. Pinte, D. J. Price, and M. Reggiani. A faint companion around CrA-9: protoplanet or obscured binary? *MNRAS*, 502(4):6117–6139, April 2021. 3.4.2

[139] J. L. Monin, F. Menard, and G. Duchene. Using polarimetry to check rotation alignment in PMS binary stars. Principles of the method and first results. *A&A*, 339:113–122, November 1998. 3.4.2

[140] Karl R. Stapelfeldt, John E. Krist, François Ménard, Jérôme Bouvier, Deborah L. Padgett, and Christopher J. Burrows. An Edge-On Circumstellar Disk in the Young Binary System HK Tauri. *ApJL*, 502(1):L65–L69, July 1998. 3.4.2

[141] C. McCabe, G. Duchêne, C. Pinte, K. R. Stapelfeldt, A. M. Ghez, and F. Ménard. Spatially Resolving the HK Tau B Edge-on Disk from 1.2 to 4.7 μm: A Unique Scattered Light Disk. *ApJ*, 727(2):90, February 2011. 3.4.2

[142] Eric L. N. Jensen and Rachel Akeson. Misaligned protoplanetary disks in a young binary star system. *Nature*, 511(7511):567–569, July 2014. 3.4.2

[143] John Kwan, Suzan Edwards, and William Fischer. Modeling T Tauri Winds from He I λ10830 Profiles. *ApJ*, 657(2):897–915, March 2007. 3.4.3

[144] Suzan Edwards, William Fischer, Lynne Hillenbrand, and John Kwan. Probing T Tauri Accretion and Outflow with 1 Micron Spectroscopy. *ApJ*, 646(1):319–341, July 2006. 3.4.3

[145] John Kwan and William Fischer. Origins of the H, He I and Ca II line emission in classical T Tauri stars. *MNRAS*, 411(4):2383–2425, March 2011. 3.4.3

[146] A. P. Sousa, J. Bouvier, S. H. P. Alencar, J. F. Donati, E. Alecian, J. Roquette, K. Perraut, C. Dougados, A. Carmona, S. Covino, D. Fugazza, E. Molinari, C. Moutou, A. Santerne, K. Grankin, É. Artigau, X. Delfosse, G. Hebrard, and SPIRou Consortium. Star-disk interaction in the T Tauri star V2129 Ophiuchi: An evolving accretion-ejection structure. *A&A*, 649:A68, May 2021. 3.4.3

[147] Suzan Edwards, William Fischer, John Kwan, Lynne Hillenbrand, and A. K. Dupree. He I λ10830 as a Probe of Winds in Accreting Young Stars. *ApJL*, 599(1):L41–L44, December 2003. 3.4.3

[148] C. Flores, G. Duchêne, S. Wolff, M. Villenave, K. Stapelfeldt, J. P. Williams, C. Pinte, D. Padgett, M. S. Connelley, G. van der Plas, F. Ménard, and M. D. Perrin. The

Anatomy of an Unusual Edge-on Protoplanetary Disk. II. Gas Temperature and a Warm Outer Region. *AJ*, 161(5):239, May 2021. 4.1, 4.4.3

[149] M. Villenave, K. R. Stapelfeldt, G. Duchêne, F. Ménard, M. Lambrechts, A. Sierra, C. Flores, W. R. F. Dent, S. Wolff, Á. Ribas, M. Benisty, N. Cuello, and C. Pinte. A Highly Settled Disk around Oph163131. *ApJ*, 930(1):11, May 2022. 4.1, 4.4.3

[150] D. Ruíz-Rodríguez, J. Kastner, P. Hily-Blant, and T. Forveille. Tracing molecular stratification within an edge-on protoplanetary disk. *A&A*, 646:A59, February 2021. 4.1, 4.4.3

[151] Eoin Cahill, Emma T. Whelan, Nuria Huélamo, and Juan Alcalá. UVES spectroscopy of T Chamaeleontis: line variability, mass accretion rate, and spectro-astrometric analysis. *MNRAS*, 484(3):4315–4324, April 2019. 4.1

[152] P. Pinilla, M. Tazzari, I. Pascucci, A. N. Youdin, A. Garufi, C. F. Manara, L. Testi, G. van der Plas, S. A. Barenfeld, H. Canovas, E. G. Cox, N. P. Hendler, L. M. Pérez, and N. van der Marel. Homogeneous Analysis of the Dust Morphology of Transition Disks Observed with ALMA: Investigating Dust Trapping and the Origin of the Cavities. *ApJ*, 859(1):32, May 2018. 4.2, 4.3.1, 4.3.1

[153] Lucas A. Cieza, Johan Olofsson, Paul M. Harvey, Christophe Pinte, Bruno Merín, Jean-Charles Augereau, II Evans, Neal J., Joan Najita, Thomas Henning, and Francois Ménard. Herschel Observations of the T Cha Transition Disk: Constraining the Outer Disk Properties. *ApJL*, 741(2):L25, November 2011. 4.3.2

[154] M. Ansdell, J. P. Williams, L. Trapman, S. E. van Terwisga, S. Facchini, C. F. Manara, N. van der Marel, A. Miotello, M. Tazzari, M. Hogerheijde, G. Guidi, L. Testi, and E. F. van Dishoeck. ALMA Survey of Lupus Protoplanetary Disks. II. Gas Disk Radii. *ApJ*, 859(1):21, May 2018. 4.4.1

[155] Ryan D. Boyden and Josh A. Eisner. Protoplanetary Disks in the Orion Nebula Cluster: Gas-disk Morphologies and Kinematics as Seen with ALMA. *ApJ*, 894(1):74, May 2020. 4.4.1

[156] Nienke van der Marel, Jonathan P. Williams, M. Ansdell, Carlo F. Manara, Anna Miotello, Marco Tazzari, Leonardo Testi, Michiel Hogerheijde, Simon Bruderer, Sierk E. van Terwisga, and Ewine F. van Dishoeck. New Insights into the Nature of Transition Disks from a Complete Disk Survey of the Lupus Star-forming Region. *ApJ*, 854(2):177, February 2018. 4.4.1

[157] Laurent Loinard, Rosa M. Torres, Amy J. Mioduszewski, and Luis F. Rodríguez. A Preliminary VLBA Distance to the Core of Ophiuchus, with an Accuracy of 4%. *ApJL*, 675(1):L29, March 2008. 4.4.3

[158] Gisela N. Ortiz-León, Laurent Loinard, Marina A. Kounkel, Sergio A. Dzib, Amy J. Mioduszewski, Luis F. Rodríguez, Rosa M. Torres, Rosa A. González-Lópezlira, Gerardo Pech, Juana L. Rivera, Lee Hartmann, Andrew F. Boden, II Evans, Neal J., Cesar Briceño, John J. Tobin, Phillip A. B. Galli, and Donald Gudehus. The Gould's Belt Distances Survey (GOBELINS). I. Trigonometric Parallax Distances and Depth of the Ophiuchus Complex. *ApJ*, 834(2):141, January 2017. 4.4.3

[159] K. A. Kretke, H. F. Levison, M. W. Buie, and A. Morbidelli. A Method to Constrain the Size of the Protosolar Nebula. *AJ*, 143(4):91, April 2012. 5.2.3